The W Boson Transverse Momentum Spectrum in Proton-Antiproton Collisions at $\sqrt{s} = 1.8$ TeV

by

Brian Lee Winer

Abstract

The Collider Detector at Fermilab (CDF) was used to measure the transverse momentum distribution of W boson produced in proton-antiproton collisions at the Tevatron collider. The W bosons were identified by the decay $W \rightarrow e\nu$. The results are in good agreement with a next-to-leading order calculation. The cross section for W production with $P_T > 50$ GeV/c is 423 ± 58 (*stat.*) $\pm$ 108 (*sys.*) pb.

James Siegrist

Chair: Prof. James L. Siegrist

Acknowledgements

I would like to start by thanking the members of the CDF collaboration for the time and money which they have invested in the CDF detector. This includes the many people who put so much effort into writing computer code which turned an electronic signal at the end of a wire into a physics quantity. I also give my appreciation to the members of my local CDF group, my advisor James Siegrist, William Carithers, William Chinowsky, Robert Ely, Kevin Einsweiler, Lina Galtieri, Richard Kadel, Michael Gold, Carl Haber, Bob Drucker, and William Wester. I am especially grateful to two members of the group, Paul Tipton and Marjorie Shapiro. Paul's advise and friendship got this analysis off to a great start and Marjorie's guidance and support down the home stretch was absolutely invaluable.

I also want to thank all the friends who made me laugh and smile when I really didn't feel like laughing or smiling. First, the members of the "SSC Ground Breaking Crew", "The Mex", "The Tex", and "The Chucker", get a special thanks from me ("The Gimp"). It was a great trip, boys! Next, there is the large "Party Gang", Vic, Phil, Hovhannes, Tim ("Tiny"), Les, Karen, Leigh, Jodi, Chris, Dee, Steve, Peter, Paul D., Johnny, and the many others who helped drain all those tequila bottles. We had some very interesting nights in the prairie. Also, my thanks to Paul T. and J.J. for keeping day to day life at Fermilab from becoming boring. Then there are the graduate students in Berkeley who helped me keep my sanity (almost). Les always reminded me that sports is much more important than physics and that there was always time to play bad golf. WWIII showed me how to enjoy Cincinatti Chile but still hate their sports teams. Dan, one of my best friends, helped me keep life in perspective and laugh at the same time. He is the only guy I know who could make chocolate chip cookies while discussing the meaning of life and then yell "Babe Alert!" when a beer commercial came on television. I also want to thank two old friends, Andy and Monika. Over the past four and a half years I was rarely in the same time zone as either of them, but their friendship was still very important to me.

My final thanks goes to the members of my family. They have been a source of

strength and enjoyment throughout my life. First, my thanks to my bothers and sisters, Tom, Linda, Greg, Sue, and Laura, and all the nieces and nephews, Jon, Evan, Michael, Meghan, Dan, Eric, and Katie, who offered such a great distraction from physics. Finally, my deepest appreciation goes to mother and father for all that they have ever given me. What they have done for my life is beyond all words, expect one ...love.

The CDF Collaboration

F. Abe,[8] D. Amidei,[4] G. Apollinari,[11] M. Atac,[4] P. Auchincloss,[14] A. R. Baden,[6] A. Bamberger,[19] A. Barbaro-Galtieri,[9] V. E. Barnes,[12] F. Bedeschi,[11] S. Behrends,[2] S. Belforte,[11] G. Bellettini,[11] J. Bellinger,[18] J. Bensinger,[2] A. Beretvas,[4] J. P. Berge,[4] S. Bertolucci,[5] S. Bhadra,[7] M. Binkley,[4] R. Blair,[1] C. Blocker,[2] A. W. Booth,[4] G. Brandenburg,[6] D. Brown,[6] E. Buckley,[14] A. Byon,[12] K. L. Byrum,[18] C. Campagnari,[3] M. Campbell,[3] R. Carey,[6] W. Carithers,[9] D. Carlsmith,[18] J. T. Carroll,[4] R. Cashmore,[19] F. Cervelli,[11] K. Chadwick,[4] G. Chiarelli,[5] W. Chinowsky,[9] S. Cihangir,[4] A. G. Clark,[4] D. Connor,[10] M. Contreras,[2] J. Cooper,[4] M. Cordelli,[5] D. Crane,[4] M. Curatolo,[5] C. Day,[4] S. Dell'Agnello,[11] M. Dell'Orso,[11] L. Demortier,[2] P. F. Derwent,[3] T. Devlin,[14] D. DiBitonto,[15] R. B. Drucker,[9] J. E. Elias,[4] R. Ely,[9] S. Errede,[7] B. Esposito,[5] B. Flaugher,[14] G. W. Foster,[4] M. Franklin,[6] J. Freeman,[4] H. Frisch,[3] Y. Fukui,[8] Y. Funayama,[16] A. F. Garfinkel,[12] A. Gauthier,[7] S. Geer,[6] P. Giannetti,[11] N. Giokaris,[13] P. Giromini,[5] L. Gladney,[10] M. Gold,[9] K. Goulianos,[13] H. Grassmann,[11] C. Grosso-Pilcher,[3] C. Haber,[9] S. R. Hahn,[4] R. Handler,[18] K. Hara,[16] R. M. Harris,[9] J. Hauser,[3] T. Hessing,[15] R. Hollebeek,[10] L. Holloway,[7] P. Hu,[14] B. Hubbard,[9] B. T. Huffman,[12] R. Hughes,[10] P. Hurst,[7] J. Huth,[4] M. Incagli,[11] T. Ino,[16] H. Iso,[16] H. Jensen,[4] C. P. Jessop,[6] R. P. Johnson,[4] U. Joshi,[4] R. W. Kadel,[4] T. Kamon,[15] S. Kanda,[16] D. A. Kardelis,[7] I. Karliner,[7] E. Kearns,[6] R. Kephart,[4] P. Kesten,[2] R. M. Keup,[7] H. Keutelian,[7] S. Kim,[16] L. Kirsch,[2] K. Kondo,[16] S. E. Kuhlmann,[1] E. Kuns,[14] A. T. Laasanen,[12] J. I. Lamoureux,[18] W. Li,[1] T. M. Liss,[7] N. Lockyer,[10] C. B. Luchini,[7] P. Maas,[4] M. Mangano[11] J. P. Marriner,[4] R. Markeloff,[18] L. A. Markosky,[18] R. Mattingly,[2] P. McIntyre,[15] A. Menzione,[11] T. Meyer,[15] S. Mikamo,[8] M. Miller,[3] T. Mimashi,[16] S. Miscetti,[5] M. Mishina,[8] S. Miyashita,[16] Y. Morita,[16] S. Moulding,[2] A. Mukherjee,[4] L. F. Nakae,[2] I. Nakano,[16] C. Nelson,[4] C. Newman-Holmes,[4] J. S. T. Ng,[6] M. Ninomiya,[16] L. Nodulman,[1] S. Ogawa,[16] R. Paoletti,[11] A. Para,[4] E. Pare,[6] J. Patrick,[4] T. J. Phillips,[6] R. Plunkett,[4] L. Pondrom,[18] J. Proudfoot,[1] G. Punzi,[11] D. Quarrie,[4] K. Ragan,[10] G. Redlinger,[3] J. Rhoades,[18] M. Roach,[17] F. Rimondi,[19] L. Ristori,[11] T. Rohaly,[10] A. Roodman,[3], A. Sansoni,[5] R. D. Sard,[7] A. Savoy-Navarro,[4] V. Scarpine,[7] P. Schlabach,[7] E. E. Schmidt,[4] M. H. Schub,[12] R. Schwitters,[6] A. Scribano,[11] S. Segler,[4] Y. Seiya,[16] M. Sekiguchi,[16] P. Sestini,[11] M. Shapiro,[6] M. Sheaff,[18] M. Shochet,[3] J. Siegrist,[9] P. Sinervo,[10] J. Skarha,[18] K. Sliwa,[17] D. A. Smith,[11] F. D. Snider,[3] R. St. Denis,[6] A. Stefanini,[11] R. L. Swartz, Jr.,[7] M. Takano,[16] K. Takikawa,[16] S. Tarem,[2] D. Theriot,[4] M. Timko,[15] P. Tipton,[9] S. Tkaczyk,[4] A. Tollestrup,[4] G. Tonelli,[11] J. Tonnison,[12] W. Trischuk,[6] Y. Tsay,[3] F. Ukegawa,[16] D. Underwood,[1] R. Vidal,[4] R. G. Wagner,[1] R. L. Wagner,[4] J. Walsh,[10] T. Watts,[14] R. Webb,[15] C. Wendt,[18] W. C. Wester, III,[9] T. Westhusing,[11] S. N. White,[13] A. B. Wicklund,[1] H. H. Williams,[10] B. L. Winer,[9] A. Yagil,[4] A. Yamashita,[16] K. Yasuoka,[16] G. P. Yeh,[4] J. Yoh,[4] M. Yokoyama,[16] J. C. Yun,[4] F. Zetti[11]

(1) Argonne National Laboratory, Argonne, Illinois 60439; (2) Brandeis University, Waltham, Massachusetts 02254; (3) University of Chicago, Chicago, Illinois 60637; (4) Fermi National Accelerator Laboratory, Batavia, Illinois 60510; (5) Laboratori Nazionali di Frascati, Istituto Nazionale di Fisica Nucleare, Frascati, Italy; (6) Harvard University, Cambridge, Massachusetts 02138; (7) University of Illinois, Urbana, Illinois 61801; (8) National Laboratory for High Energy Physics (KEK), Tsukuba, Ibaraki 305, Japan; (9) Lawrence Berkeley Laboratory, Berkeley, California 94720; (10) University of Pennsylvania, Philadelphia, Pennsylvania 19104; (11) Istituto Nazionale di Fisica Nucleare, University and Scuola Normale Superiore of Pisa, I-56100 Pisa, Italy; (12) Purdue University, West Lafayette, Indiana 47907; (13) Rockefeller University, New York, New York 10021; (14) Rutgers University, Piscataway, New Jersey 08854; (15) Texas A&M University, College Station, Texas 77843; (16) University of Tsukuba, Tsukuba, Ibaraki 305, Japan; (17) Tufts University, Medford, Massachusetts 02155; (18) University of Wisconsin, Madison, Wisconsin 53706; (19) Visitor

This work was supported by the U.S. Department of Energy and Lawrence Berkeley Laboratory under Contract DE-AC03-76SF00098.

Contents

List of Figures

List of Tables

Chapter 1

Theoretical Discussion

1.1 Introduction

In this century, physicists have explored nature by studying the interactions between fundamental particles. Particles interact via the basic forces of nature. These forces consist of the strong force, the electromagnetic force, the weak force, and the gravitational force[1]. By studying the dynamics of particle interactions, we can learn about the structure of nature. This knowledge is used not only to test current theoretical models but also provide motivation for new models. The dynamics of particle physics is described by the *Standard Model* (see Section 1.2).

Physicists have studied particle interactions by colliding particles to induce an interaction. The early experiments in particle physics used radioactive sources to give energetic particles. For example, in 1911 Rutherford used a source of α particles incident on a thin metal foil to discover the nucleus [1]. The development of particle accelerators allowed higher energy interactions and therefore provided a deeper probe into nature. The accelerators include electron-positron colliding machines such as LEP and the SLC [2, 3]. In addition, there are several hadron colliders both operating and proposed. The highest energy accelerator is the Tevatron collider at Fermi National Accelerator Laboratory. The

[1] For the interaction between fundamental particles, the gravitational force is so weak compared with the other forces that it is neglected.

Tevatron provides proton-antiproton collisions at a center-of-mass energy of 1.8 TeV. The high center-of-mass energy of the Tevatron allows the creation of very massive particles.

The $W^{\pm}$ and Z bosons are one of the most recent discoveries in particle physics. These intermediate vector bosons were formally postulated with the unification of the electromagnetic and weak forces [4, 5, 6]. The particles were first observed at the CERN Sp$\bar{p}$S collider in the early 1980's [7, 8, 9, 10]. Because of its mass and its coupling, the W boson can currently only be created in proton-antiproton collisions. Studying W boson production properties provides insights into the *Standard Model.* One of the production properties is the transverse momentum (P_T) spectrum for the W boson. The W boson transverse momentum is generated by QCD processes (see Section 1.4). The focus of this thesis is the measurement of the differential cross section, $d\sigma/dP_T$, for W boson production.

1.2 The Standard Model

The *Standard Model* describes the interaction between the fundamental particles of nature. The model consists of Quantum Chromodynamics (QCD) [11, 12, 13] and the Electroweak Model which includes Quantum Electrodynamics (QED). The strong interaction is described by QCD which is based on the group SU(3). The Electroweak Model describes the electromagnetic and weak interactions and is based on the group structure of $SU(2)_L \times U(1)$. This model is the result of the unification of the electromagnetic and weak interactions by Glashow, Weinberg, and Salam in the late 1960's [4, 5, 6].

The *Standard Model* contains two types of fundamental particles, the fermions and the bosons. The fermions are quarks or leptons with spin $\frac{1}{2}$. There are 6 quarks, Up (u), Down (d), Charm (c), Strange (s), Top (t), and Bottom (b). The six quarks appear in three doublets or families (see Table 1.1). The existence of all the quarks, except the Top quark have been experimentally verified. Each quark has an additional degree of freedom called color. The color is labelled Red (R), Green (G), or Blue (B). The quarks bound in color singlet states form the hardrons. For instance, the ψ is the 1^3S_1 bound state of a $c\bar{c}$ pair. Quarks can only exist in color singlet states and therefore can not be isolated.

Fundamental Particles								
Fermions								Bosons
Quarks			Q ($\|e\|$)	Leptons			Q ($\|e\|$)	$W^{\pm}$, Z^{o},γ,
u	**c**	**t**	+2/3	ν_e	ν_μ	ν_τ	0	8 gluons (g)
d	**s**	**b**	−1/3	**e**	μ	τ	−1	Higgs (H)
• Quarks and gluons carry color (R,G,B)								
• Leptons, $W^{\pm}$,Z^{o}, γ are colorless								
• The quarks and leptons also have antiparticle counterparts								

Table 1.1: The fundamental particles are broken down into several groups. The fermions consist of the quarks and leptons. The interactions between these particles are mediated by the second group, the bosons.

The leptons are the second group of fermions. The leptons also appear in three families (see Table 1.1). The electron, muon and tau all have mass and carry a negative electric charge ($-|e|$). Three neutrinos exist and each is paired with either the electron, the muon, or the tau. The neutrinos carry no electric charge and are taken as massless[2]. Leptons carry no color and therefore experience no strong interactions. Since the neutrinos have zero charge, they experience only weak interactions. The leptons and the quarks all have antiparticle counterparts (*e.g.* the positron is the antiparticle of the electron).

The bosons which have integer spin are the final class of particles in the *Standard Model.* The gauge bosons are the photon (γ), W^+, W^-, Z^o, and 8 gluons (g). The photon, the W's, and the Z bosons mediate the electroweak force. The gluons mediate the strong force between particles carrying color. As feature of the non-abelian group nature of QCD, the gluons also carry color and therefore undergo self-interactions. The last boson is the Higgs boson. The Higgs was theoretically constructed to explain the masses of the fundamental particles. So far, no experimental evidence exists for the Higgs boson.

[2]The measurements of the electron neutrino mass give a mass less than 17 eV/c^2 and consistent with massless [14].

1.3 Proton-Antiproton Collisions

Proton-antiproton collisions are complicated by the fact that the proton and antiproton are not fundamental particles. Both the proton and the antiproton are composed of three valence quarks (proton: uud, antiproton: $\bar{u}\bar{u}\bar{d}$), gluons, and 'sea' or 'ocean' quarks which appear as virtual pairs. In most proton-antiproton collisions, the partons (quarks and gluons) are involved in low energy interactions. However, occasionally the partons interact with either a large momentum transfer or an annihilation into an energetic state (see Figure 1.1). For example, the partons could form an energetic virtual intermediate state or a real heavy particle such as the W or the Z boson. The final state consists of fermions and bosons. If quarks or gluons are in the final state, they fragment into hadrons which are presumed to be approximately collinear with the final state parton direction. The collection of particles from the fragmentation of a parton is called a jet. If a W or Z is in the final state, it can decay into leptons or into quarks which then fragment. The partons not involved in the energetic interaction are "spectators" and contribute low energy particles to the event. These low energy particles are called the "underlying event".

In order to calculate an observable cross section in proton-antiproton collisions, the parton cross section must be convoluted with the momentum distributions of the partons in the proton and antiproton.

$$\sigma_{tot}(AB \to C) = \sum_{ij} \int dx_i dx_j f(x_j) f(x_i) \hat{\sigma}(p_i p_j \to C) \tag{1.1}$$

The cross section, $\hat{\sigma}(p_i p_j \to C)$, represents the cross section for parton i with momentum p_i and parton j with momentum p_j to create C. The sum runs over all possible partons. The quantity $f(x_k)$ ($\bar{f}(x_k)$) represents the probability for having a parton k with momentum fraction $x_k = p_k/P_{proton}$ in the proton (antiproton). The $f(x_k)$ depends on the type of parton (gluon or quark flavor). Figure 1.2 shows the distribution functions, $f(x_k)$, for the partons in a proton. The distribution functions are determined from $\nu - N$ and $e - N$ scattering and evolved to higher Q^2 with the Altarelli-Parisi equations [15, 16, 17].

In proton-antiproton collisions, the momentum of the two partons involved in the

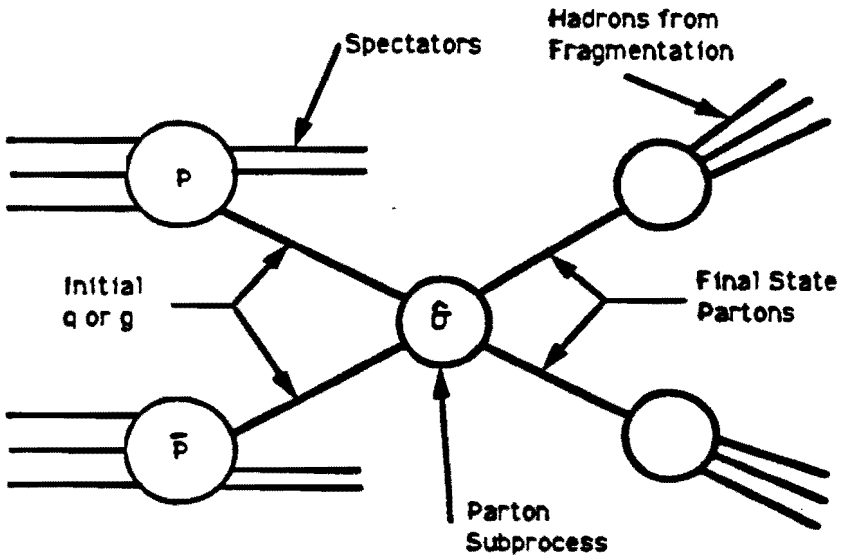

Figure 1.1: At the Tevatron the most interesting events involve an energetic interaction between two constituents of the proton and antiproton. The other partons are called spectators. The products of the interaction fragment into hadrons or in the case of the W boson decay into leptons.

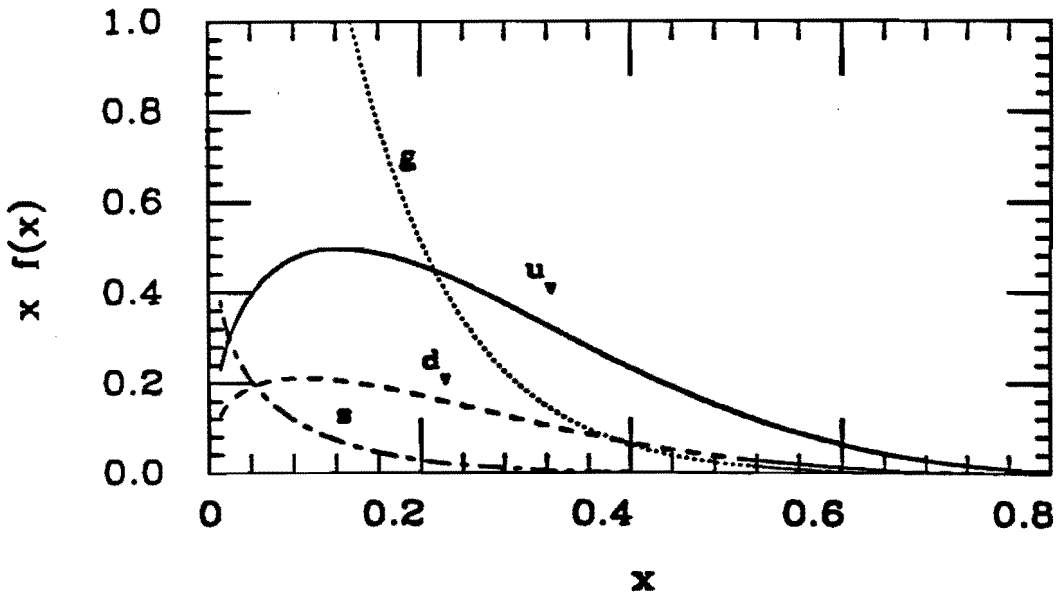

Figure 1.2: The distribution functions, f(x), represent the probability of finding a quark with momentum fraction $x = p/P_{proton}$ between x and x + dx. The distribution functions are shown for the up, down and strange quarks along with the gluon. EHLQ1 structure functions were used.

collision is not *a priori* known. In addition, small angle products of the collision can travel down the accelerator's vacuum chamber and escape detection. Therefore, the momentum parallel to the beam is not a useful quantity in $p\bar{p}$ collisions. The collisions are described using quantities which are defined transverse to the beams' direction since this component is assumed to be initially zero for every collision. Some of the useful quantities are:

1. Transverse Momentum, $P_T = P\sin\theta$, where θ is the polar angle using the z vertex and the beam axis.
2. Transverse Energy, $E_T = E\sin\theta$, is an analog of the P_T but using the energy[3].
3. Transverse Mass, M_T^{ij}, of two particles, i and j, as

$$M_T^{ij} = ((P_i^x + P_j^x)^2 + (P_i^y + P_j^y)^2)^{1/2}$$

   where x and y are orthogonal components perpendicular to the beam axis. The transverse mass is the two component analog of the four component invariant mass. The transverse mass distribution for the decay products of a massive particle will peak near the mass of the heavy particle. This quantity is invariant to boosts along the beam direction and it insensitive to boosts in the transverse direction.
4. Pseudorapidity, η, is defined as:

$$\eta = -\ln\tan(\theta/2)$$

   where θ is the polar angle.

1.4 W Production

Considering W production in lowest order, the W is created by the annihilation of a quark and an antiquark (see Figure 1.3(a)). For creating a W^+, the quark is normally a u quark

[3]Although energy is a scalar, it is often treated as a vector. The energy (E) is measured with the calorimeter. Since the particles which enter the calorimeter have a small mass, the energy (E) is approximately the same as the momentum (P).

and the antiquark is a $\bar{d}$ quark. In this case the parton cross section is written as

$$\hat{\sigma}(u\bar{d} \rightarrow W^+) = 2\pi|V_{ud}|^2 \frac{G_F}{\sqrt{2}} M_W^2 \delta(\hat{s} - M_W^2) \tag{1.2}$$

where V_{ud} is an element of the Kobayashi-Maskawa matrix, G_F is the Fermi constant, M_W is the W mass, and $\hat{s} = x_u x_{\bar{d}} s$ where s is the center of mass energy of the proton-antiproton collision. The Fermi constant, G_F, represents the magnitude of the coupling of the W bosons to quarks. To determine the observable cross section, the subprocess cross section must be convoluted with the proton and antiproton distribution functions (see Eq. 1.1). More complicated subprocess cross sections arise from higher order diagrams which must be included for an accurate prediction of the total cross section. A measurement of the W production cross section represents a test of their assumed coupling, G_F, of quarks to the W boson[4].

W's are produced with momentum transverse to the beam direction (P_T^W). Most often the W is produced with a small P_T (< 10 GeV/c). In these cases, one or both of the initial quarks undergoes initial state gluon radiation which gives the W a small P_T. However, W's can also be created with a large P_T (> 30 GeV/c). In this case, the W recoils against an energetic quark or gluon. The W can also recoil against a system of quarks and/or gluons (see Figure 1.3). In this case, the coupling of quarks to gluons enters the calculation along with coupling of W's to quarks. Measuring the cross section of W bosons produced with a large transverse momentum provides a test of the theoretical models used to predict the production of W's with associated quarks and gluons.

In the small P_T^W region, most gluons produced with the W will have a very small P_T. Gluon resummation techniques can be used to calculate the P_T^W spectrum in the small P_T^W region and avoid the divergences in the theory [18]. In the large P_T^W region, QCD calculations using perturbation theory give an accurate prediction of the P_T^W spectrum. Some of the diagrams which contribute to the large P_T^W region are shown in Figure 1.3. The first order, $\mathcal{O}(\alpha_s)$, diagrams (Figure 1.3 (b) and (c)) show the W recoiling against a

[4]Measuring the W cross section, however, is not an accurate method for determining G_F.

quark or gluon. The second order, $O(\alpha_s^2)$, diagrams either can have a second final state parton (see Figure 1.3(d)) or it can contain an internal loop (see Figure 1.3(e)). The diagrams with internal loops give rise to interference terms with lower order processes.

For the large P_T^W region, a complete $O(\alpha_s^2)$ calculation has been performed by Arnold and Reno [19]. In addition, a next-to-leading order calculation using gluon resummation has been performed for the small P_T^W region. The small P_T^W calculation is matched with the large P_T^W calculation to give a next-to-leading order prediction for all P_T^W [20]. Figure 1.4 shows the prediction for the differential cross section, $d\sigma/dP_T$, for W boson production at the Tevatron. The prediction used HMRS(B) structure functions [21] and $\Lambda_{QCD} = 190$ MeV (a parameter of the theory).

Previous measurements of the W transverse momentum spectrum at the CERN Sp$\bar{p}$S collider showed excellent agreement with the predicted spectrum [22, 23]. However, at the higher center-of-mass energy, the Tevatron gives a larger production cross section than at the CERN collider. Although the total cross section for W production differs only by a factor of three, the cross section at large P_T^W differs dramatically. For example, the cross section at $P_T^W = 50$ GeV/c is more than an order of magnitude larger at the Tevatron and at $P_T^W = 100$ GeV/c the Tevatron cross section is approximately 60 times larger than at the Sp$\bar{p}$S. The recent measurement by UA2 has reached to P_T^W's on the order of 100 GeV/c [22]. The measurement at the Tevatron can reach to 180 GeV/c, even with less integrated luminosity.

1.5 W Boson Decay

The lifetime of the W boson is very short and it decays into quarks or leptons. The W's largest branching fraction ($\sim$ 70%) is into a quark and antiquark. Although this channel has the largest branch fraction, it is impossible to select a clean sample of W events using this mode since the background from other QCD processes overwhelms the signal. The W also decays into a charged lepton and its corresponding neutrino (*e.g.* W$\rightarrow$ e ν_e). The branching fraction into each lepton channel is approximately 10%. The lepton channels can

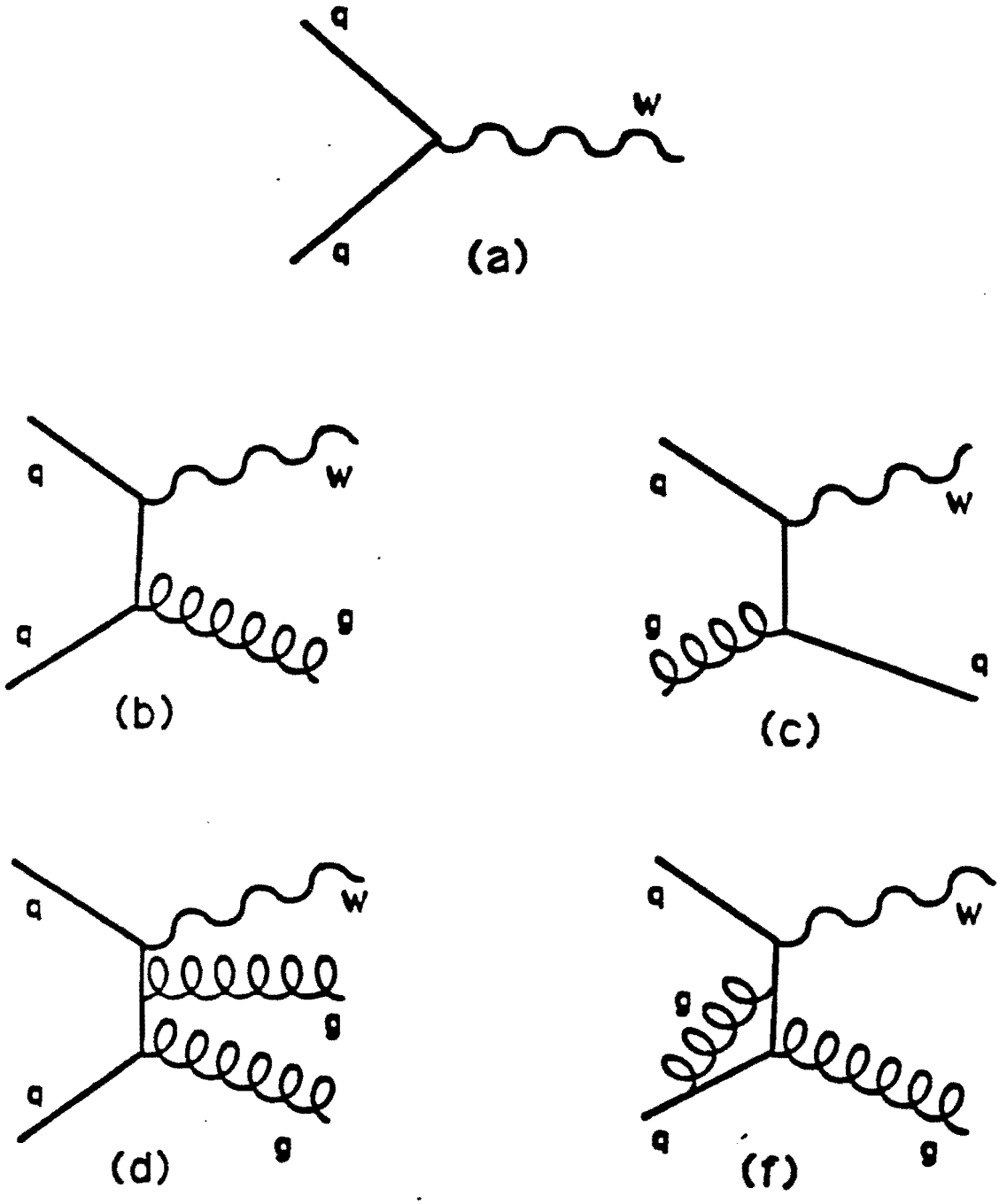

Figure 1.3: The Feynman diagrams for W boson production are shown. The lowest order process is shown in (a). Examples of the higher order diagrams are shown in (b-c), $\mathcal{O}(\alpha_s)$, and (d-e), $\mathcal{O}(\alpha_s^2)$.

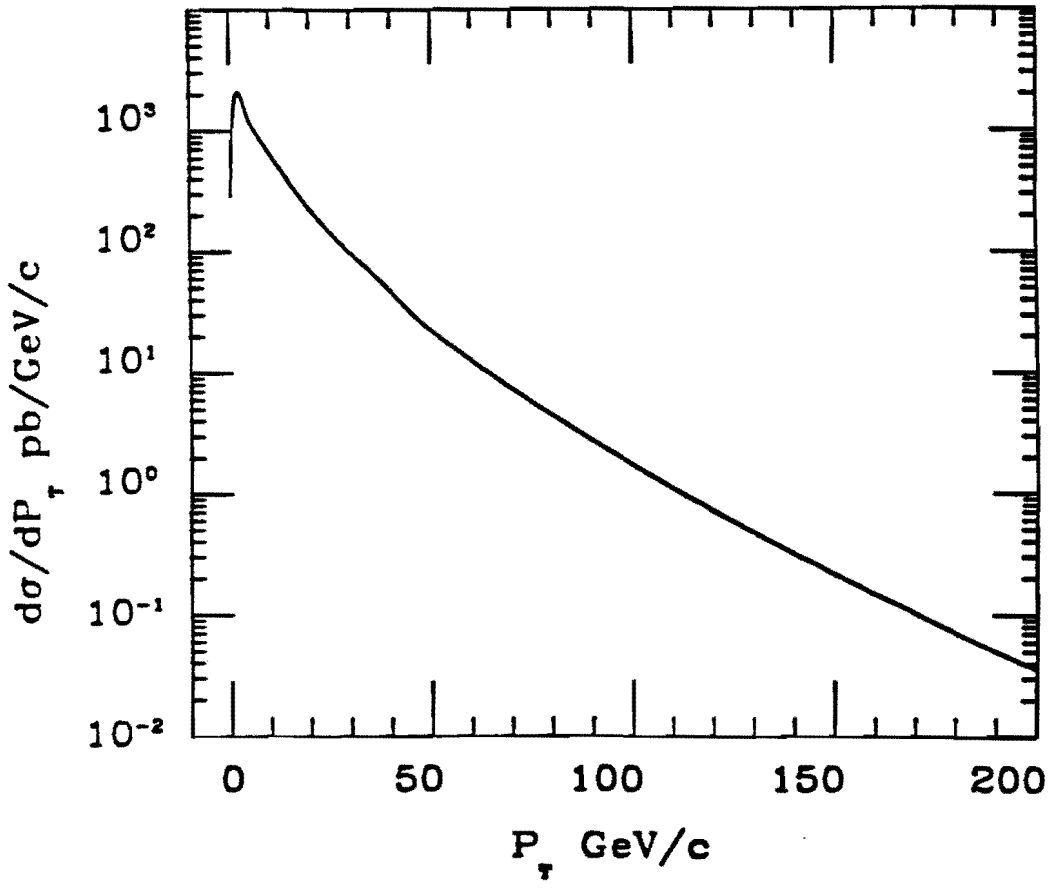

Figure 1.4: The next-to-leading order prediction for W production at Tevatron energies with HMRS(B) structure functions and $\Lambda_{QCD} = 190$ MeV. The roll over at low P_T is caused by phase space.

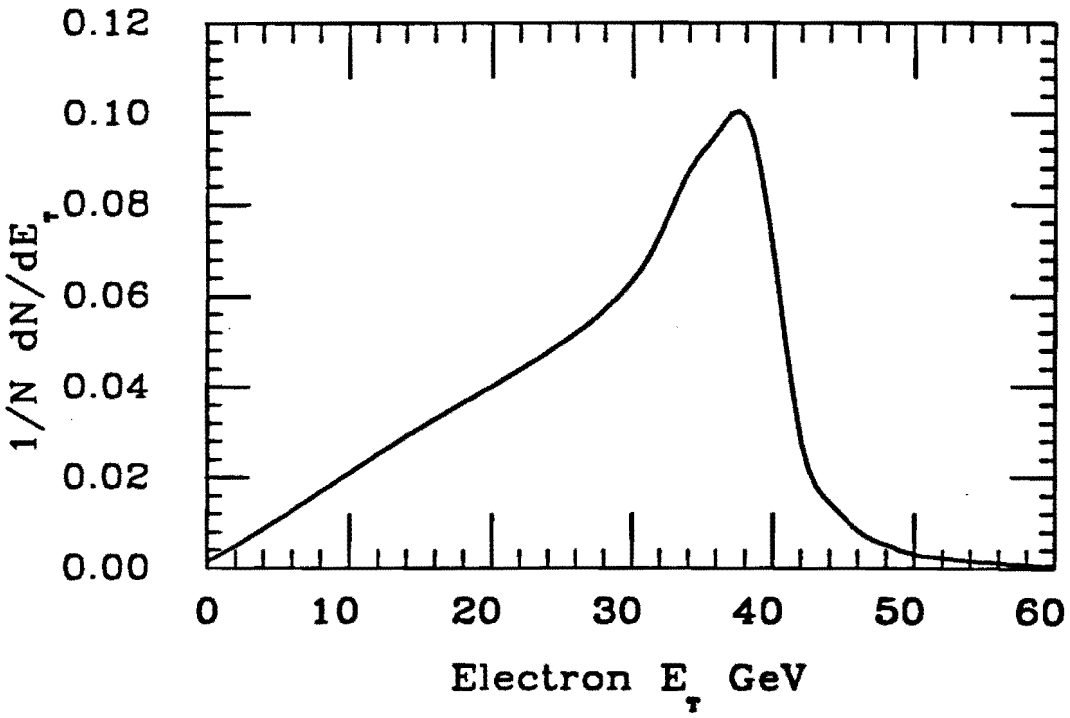

Figure 1.5: The transverse energy spectrum for an electron from the decay of a W. The Jacobian peak occurs near $M_W/2$.

be used to select a clean sample of W events. For the analysis presented in this thesis, the electron-neutrino channel was used[5].

The electron and neutrino from a W decay are very energetic because of the large mass of the W boson (80 GeV/c^2). Since the W decay is a two body decay, a peak exists in the transverse energy spectrum of the decay products. The peak is caused by a Jacobian factor which enters $d\sigma/dE_T$ when changing from an angular variable to E_T. The Jacobian factor introduces a singularity which becomes finite when the width of the W mass is included. The peak is located near half the W mass. Figure 1.5 show the Jacobian peak for the electron transverse energy (E_T) spectrum from a W Monte Carlo program. The E_T spectrum for the neutrino is similar.

[5]From now on "electron" will be used to describe both the electron and the positron.

1.6 Summary of the Analysis

Measuring the differential cross section, $d\sigma/dP_T$, for W boson production involved many steps. First, a sample of events containing a W boson was selected from the large number of recorded events. Since the W boson's lifetime is very short, it was identified by its decay products. The decay of the W into an electron and a neutrino provides a very distinct signal. The electron has a large E_T (see Figure 1.5). The neutrino is also energetic, however, it does not interact in the detector so it must be indirectly detected by an imbalance in the transverse energy deposits (see Section 2.2.3). The event selection discussed in Chapter 3 was based on identifying events with both a high E_T electron and missing transverse energy ($\not\!\!E_T$).

Once the sample of W events was selected, the sample characteristics were studied. This included determining if any background events remained in the sample. Potential sources of background events included quarks or gluons which fragmented in a manner which mimicked an electron signal and events with real electrons from sources other than W decay. Besides determining the number of background events, the shape of the P_T^W spectrum for each background was also determined so that the background could be subtracted from the observed spectrum. The method for finding the background and its shape is discussed in Chapter 3. Finally, Chapter 3 concludes with a discussion of event selection efficiencies and acceptances. These quantities are important for the normalization of $d\sigma/dP_T$.

After the event sample was selected, the P_T of the W boson was determined for each event. Since only the decay products were observed, the P_T was reconstructed from the electron and neutrino momentum[6].

$$\vec{P}_T^W = \vec{P}_T^{ele} + \vec{P}_T^{\nu}. \tag{1.3}$$

However, the procedure is complicated by the fact the neutrino is not directly observed. Instead, the neutrino E_T was measured indirectly from all the energy deposited in the

[6]When measuring the P_T of the electron and the neutrino, the calorimeter is used so the P_T is given as E_T. Because the mass of the two leptons is so small on the scale of their P_T, the E_T and P_T are equivalent.

calorimeter. This included the energy of the electron and the energy of the particles recoiling against the W. Since the electron E_T enters the neutrino E_T with a negative sign (see Section 2.2.3), the electron energy cancels out of the P_T^W calculation (see Section 4.1.2). Therefore, the P_T of the W boson was effectively measured from the recoil energy. Properly measuring the recoil energy represented the most difficult portion of this analysis. Cracks between calorimeter towers and nonlinear response of the calorimeter to low energy particles caused the observed recoil energy, and therefore the P_T^W, to be biased low. Chapter 4 discusses how the energy was corrected on an event-by-event basis to determine the best value of P_T^W.

After correcting the recoil energy, the spectrum dN/dP_T was determined. The spectrum is a sharply falling distribution (see Figure 1.4). When a falling distribution is convoluted with the detector's resolution, the spectrum becomes distorted or smeared towards larger values. In order to determine the proper dN/dP_T, a correction for these resolution smearing effects was determined (Chapter 4). Combining all the corrections, efficiencies, acceptance, and backgrounds lead to the determination of the differential cross section,

$$(\frac{d\sigma}{dP_T})_i = S * \frac{R_i}{W_i A_i}(N_i - B_i) \tag{1.4}$$

where,

- S is a normalization factor dependent on the event selection efficiency, integrated luminosity, etc.
- R_i is the resolution smearing correction factor of the i^{th} bin.
- W_i is the bin width of the i^{th} bin.
- A_i is the acceptance value of the i^{th} bin.
- N_i is the number of events in the i^{th} bin after energy corrections.
- B_i is the number of background events in the i^{th} bin.

Chapter 5 discusses these factors in more detail. Chapter 5 also presents the method used to propagate the systematic uncertainties into the cross section measurement. Finally, the results of the measurement are summarized in Chapter 6.

Chapter 2

Experimental Description

The Collider Detector at Fermilab (CDF) is located at one of the high luminosity interaction regions of the Tevatron $p\bar{p}$ collider (see Figure 2.1). The collider begins with ionized hydrogen atoms accelerated with a Cockcroft-Walton accelerator. Next, the protons are accelerated to 200 MeV in a linear accelerator. A booster ring (R = 75.45 m) boosts the proton energy to 8 GeV before the protons are injected into the main ring at Fermilab. The main ring (R = 1 km) accelerates the protons to 150 GeV. The protons are either injected into the Tevatron ring located just below the main ring or collided with a tungsten target to create antiprotons. The antiprotons are stored and stochastically cooled in an accumulator ring and later injected into the Tevatron ring [24].

In the Tevatron ring, bunches of protons and antiprotons are accelerated to 900 GeV. For the 1988-89 collider run, six bunches of protons and six bunches of antiprotons were used in the Tevatron. Quadrupole magnets on either side of the CDF interaction point focused the beams to provide the highest luminosity. The peak luminosity during the 1988-89 collider run was $2 \times 10^{30}\ cm^{-2}\ sec^{-1}$; the accelerator delivered an integrated luminosity of 8.5 pb^{-1} to the CDF interaction region.

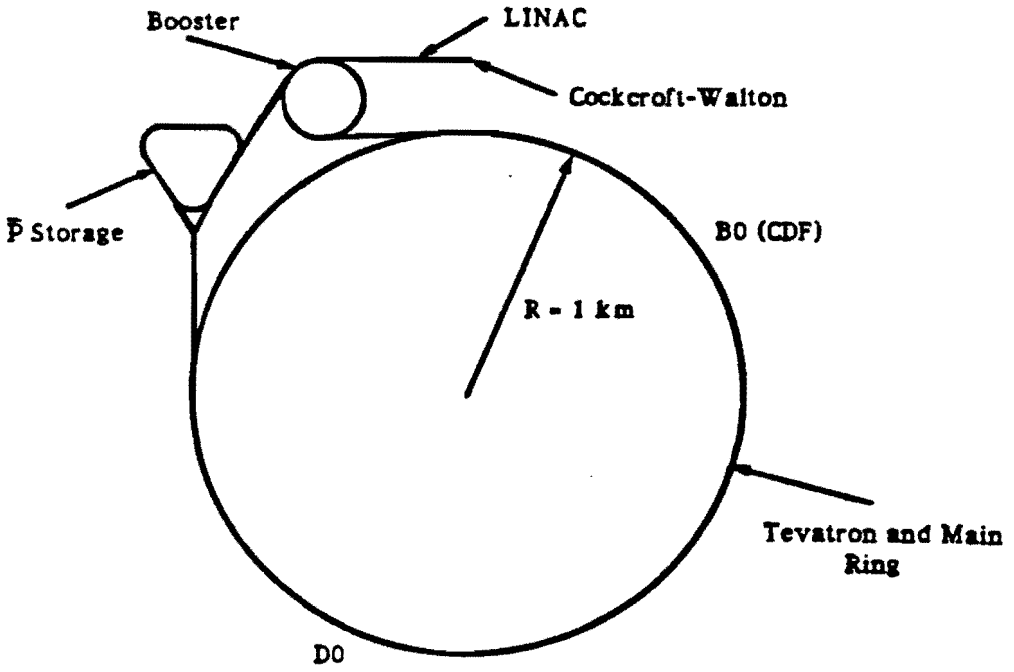

Figure 2.1: Schematic diagram of the Tevatron collider at Fermi National Accelerator Laboratory. The CDF is located at the B0 interaction region in the Tevatron Ring.

2.1 Detector

CDF is a large multi-purpose detector. It is designed for good lepton identification while also measuring jet energies. A cross section of CDF is shown in Figure 2.2. Tracking chambers make up the inner most region of the detector. CDF has a superconducting solenoid which generates an axial magnetic field in the tracking chambers. Calorimeters that surround the tracking chambers cover a range in pseudorapidity ($\eta = -\ln \tan \theta/2$)[1] from -4.2 to 4.2 and the entire azimuthal (ϕ) range. Below is a discussion of the components which are relevant to this analysis. A more complete description of CDF can be found elsewhere [25].

[1]The CDF coordinate system defines the z along the direction of the proton beam direction, θ as the polar angle, and ϕ as the azimuthal angle.

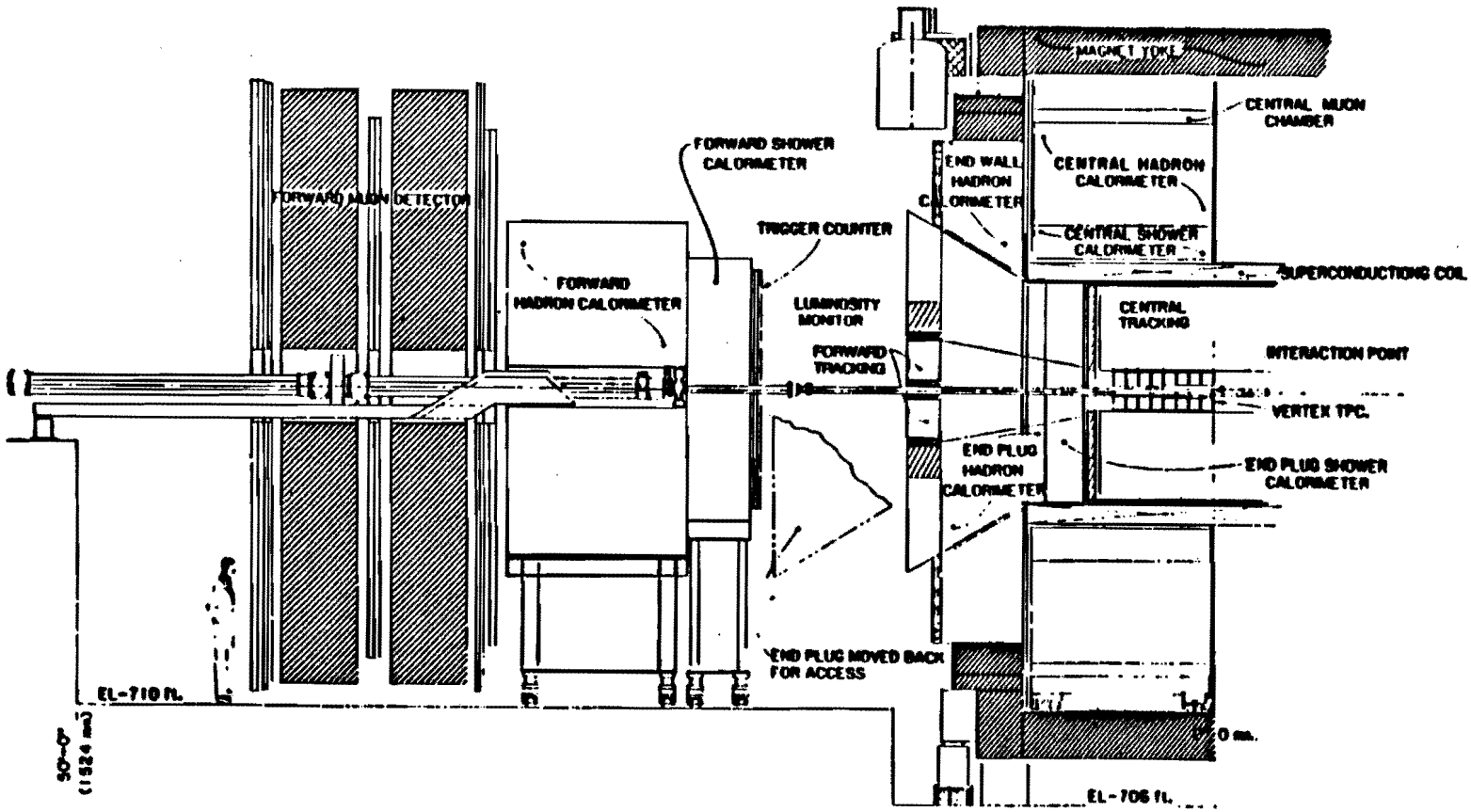

Figure 2.2: The cross section of the CDF detector. Only half of the detector is shown. A mirror image exists opposite of the nominal interaction point.

Coverage:	
Inner	$3.5° < \theta < 176.5°$
	$-3.5 < \eta < 3.5$
Outer	$8.7° < \theta < 171.3°$
	$-2.6 < \eta < 2.6$
Mechanical:	
Modules	8
Octants/Mod.	16
Wires/Oct.	24
Pads/Oct.	24
Module Inner Radius	7 cm
Module Outer Radius	21 cm
Module Length	35.3 cm
Drift Length	15.25 cm
E Drift Field	256 V/cm
Gas	50-50 Ar-Ethane
Resolution:	
Spatial	$200 - 500$ μm
2-track	6 mm (Z), 6 mm (r)
	3 cm (ϕ)

Table 2.1: The physical properties for the Vertex Time Projection Chamber (VTPC).

2.1.1 Tracking

The tracking in CDF begins with a vertex time projection chamber (VTPC) surrounding the Tevatron's vacuum chamber. The VTPC consists of eight modules of time projection chambers which provide r-z information for charged particles exiting the event vertex with a polar angle between 3.5° and 178.5°. The physical parameters of the VTPC are given in Table 2.1. The VTPC is primarily used to determine the z vertex position of each event. It is also used to identify photons which converted to electron-positron pairs after exiting the VTPC.

The central tracking chamber (CTC) is a large drift chamber surrounding the VTPC and inside the superconducting coil which produced an 1.4 Tesla axial magnetic field. The CTC provides spatial (r-ϕ-z) information for charged particles. A measurement of the particle's P_T was derived by determining the track's curvature in the magnetic field. The physical characteristics of the CTC are given in Table 2.2.

Coverage:	
Inner	$15° < \theta < 165°$
	$-2.0 < \eta < 2.0$
Outer	$40° < \theta < 140°$
	$-1.0 < \eta < 1.0$
Mechanical:	
Superlayers	9
Axial Layers	5
Wires/Axial Layer.	12
Stereo Layers	4
Wires/Axial Layer.	6
Inner Radius (Active)	30.9 cm
Outter Radius (Active)	132.0 cm
Wire Length	321.4 cm
Total Wires	36,504
Drift Length	15.25 cm
E Drift Field	1350 V/cm
Gas	Ar (49.6%)
	Ethane (49.6%)
	Alcohol (0.8%)
Resolution:	
Spatial	200 μm (r-ϕ)
	6 mm (Z)
2-track	3.5 mm
Momentum	$\delta P_T/P_T = 0.0020 \times P_T$
Momentum (Beam Constrained)	$\delta P_T/P_T = 0.0011 \times P_T$

Table 2.2: The physical properties for the Central Tracking Chamber (CTC).

The CTC has 84 layers of sense wires grouped into superlayers. There are five superlayers with 12 sense wires. These layers have axial sense wires. Between each of the axial superlayers is a superlayer with 6 sense wires at a $\pm 3°$ angle relative to the beam to determine the z position. There are 4 such "stereo" layers total. Each superlayer is divided into drift cells with planes of field shaping wires. The cells are tilted at an angle of 45 degrees to compensate for the Lorentz angle drift of charge particles in an electric and magnetic field. The spatial resolution, two track resolution, and momentum resolution are given in Table 2.2.

2.1.2 Calorimetry

The CDF calorimeters are arranged in towers which project back to the geometric center. The central calorimeter covers the region $|\eta| < 1.1$. The segmentation is $\Delta\phi = 15°$ and $\Delta\eta = 0.1$ (see Figure 2.3). The region $1.0 < |\eta| < 2.2$ is covered by the plug calorimeter. The segmentation in this region is $\Delta\phi = 5°$ and $\Delta\eta = 0.09$. The low angle region, $2.0 < |\eta| < 4.2$, is covered by the forward calorimeter where the segmentation is $\Delta\phi = 5°$ and $\Delta\eta = 0.1$ There is only partial coverage at very low angles due to space taken by the low-β quadrupoles of the Tevatron. Some overlap exists between the various calorimeters.

Central and EndWall Calorimeters

The central calorimeter has an electromagnetic section and a hadronic section. The physical characteristic of the calorimeters are summarized in Table 2.3. In the region $0.7 < |\eta| < 1.3$, the endwall calorimeter provides coverage for the hadronic calorimeter. The electromagnetic section was constructed of alternating layers of lead and scintillator. The hadronic section was constructed of alternating layers of iron and scintillator. The central calorimeter is segmented into 15° wedges (see Figure 2.4). Wave shifting material attached to the scintillator redirects light to acrylic lightguides which carry the light to photomultipliers found at the back of the calorimeter. The photomultiplier signals feed into the amplifiers in the front end electronics (see Section 2.1.3). The resolution of the calorimeters are given

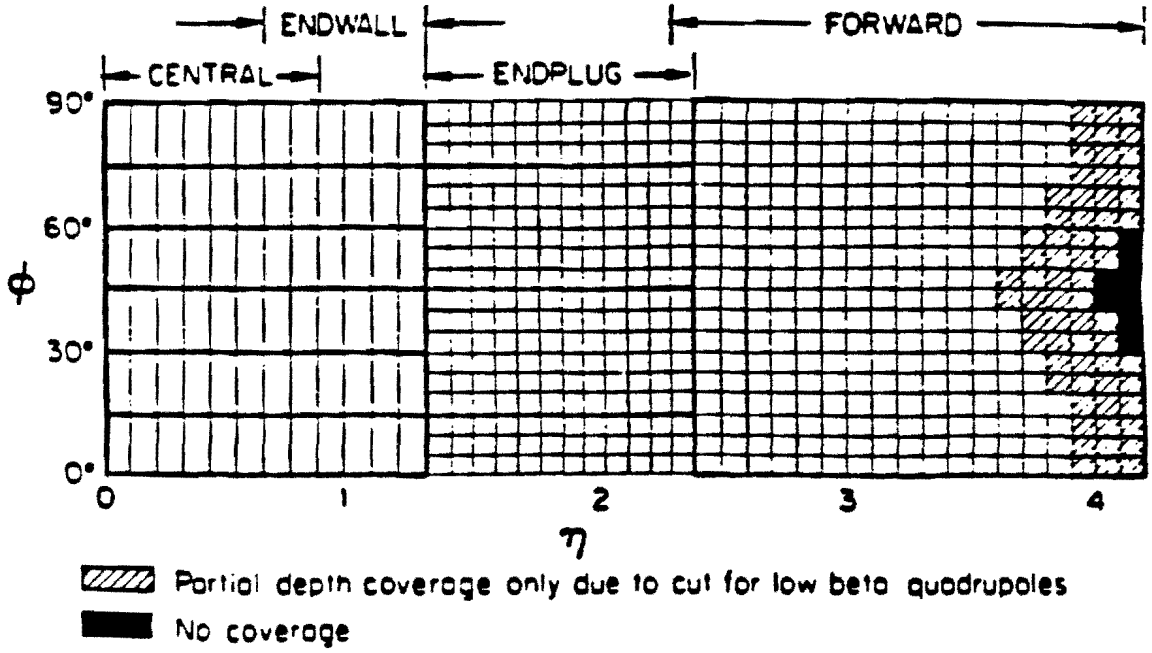

Figure 2.3: The tower segmentation of the calorimeters is shown for 1/8 of the detector. The finer segmentation occurs in the gas calorimeters.

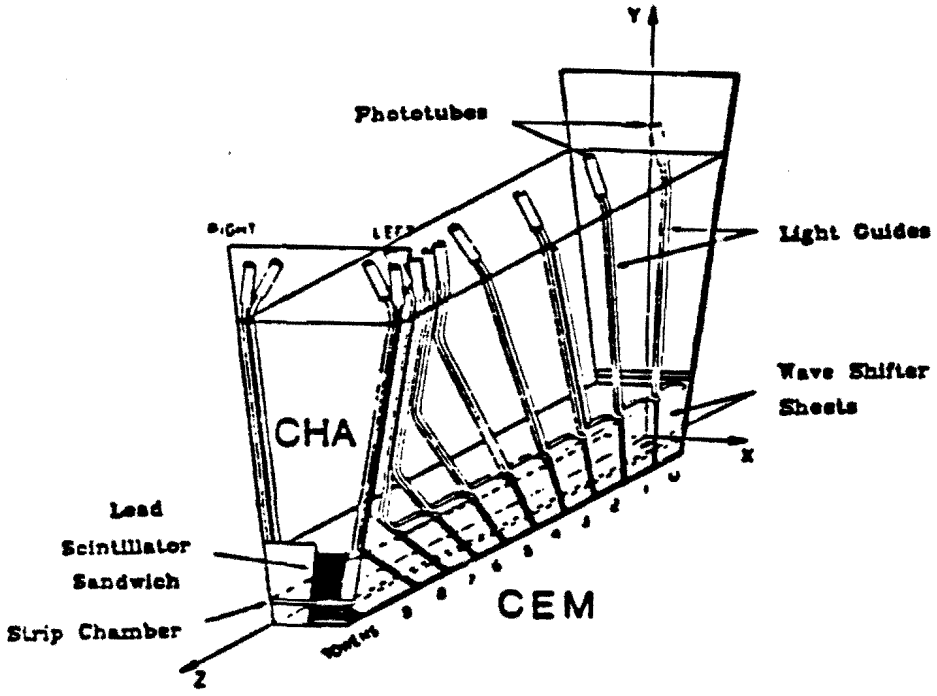

Figure 2.4: A central calorimeter wedge. Twelve wedges make up one arch of the central calorimeter. There are four aches total.

	Central (EM)	Central (Had)	Endwall (Had)
Coverage ($\|\eta\|$)	$0-1.1$	$0-0.9$	$0.7-1.3$
Tower Size ($\Delta\eta \times \Delta\phi$)	$0.1 \times 15°$	$0.1 \times 15°$	$0.1 \times 15°$
Module Length	250 cm	250 cm	100 cm
Module Width	15°	15°	80 cm
Number of Modules	48	48	48
Active Medium	SCSN-38 polytyrene Scintillator	PMMA doped scintillator	PMMA doped Scintillator
Thickness	5 mm	1.0 cm	1.0 cm
# Layers	21-31	32	15
Absorber	Pb	Fe	Fe
Thickness	1/8 in	2.5 cm	5 cm
# Layers	20-30	32	15
Energy Resolution (σ/E(GeV))	$13.5\%/\sqrt{E}$	11% (50 GeV π)	14% (50 GeV π)

Table 2.3: The physical properties for the central and endwall calorimeters.

in Table 2.3.

The central electromagnetic calorimeter has proportional wire chambers (CES) at 6 radiation lengths, approximately the position of maximum shower development for an electron shower. The anode wires provide R*ϕ position information for electromagnetic showers. The chambers also have cathode strips which provide z position information for the shower.

The calibration of the central calorimeter was first determined using a beam of pions and electrons with known variable energy. The calibration was monitored using cesium sources which can be positioned in front of each tower in a wedge. In addition, a Xenon flash system which injects light into the wave shifting material and a green LED which injects light into the photomultiplier were used to check the calibration of each piece of the system. The calibration was maintained to $\sim 0.5\%$.

The response of the electromagnetic calorimeter over the face of each tower was mapped using electrons from a test beam. The electromagnetic tower response as a function of tower position is shown in Figure 2.5. The higher response occurs near the edge of the scintillator where the light is collected. This response map was used to correct the energy

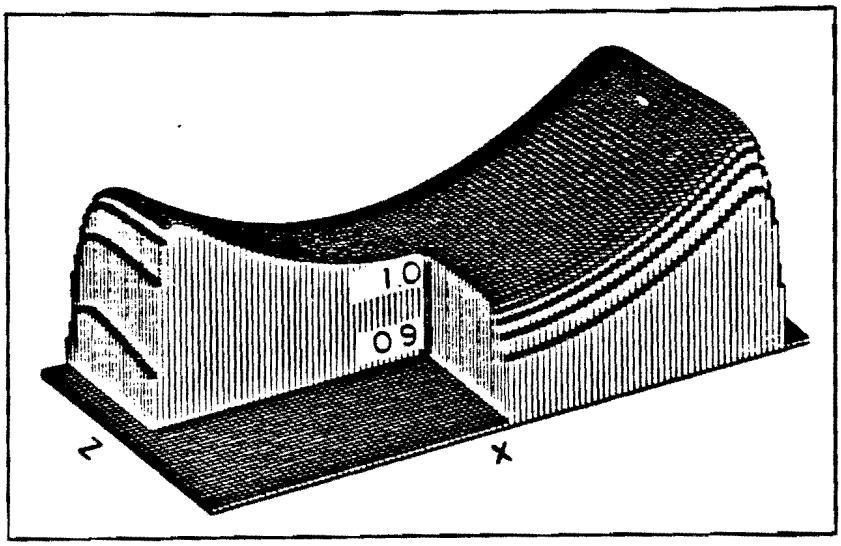

Figure 2.5: The central electromagnetic calorimeter tower response map shows the dependence of response on the electron position in a typical tower. Z is along the beam direction and X is the azimuthal direction Each tower has a slightly different response. This is used to correct measured electron energies (see Chapter 4).

of the electron (see Section 4.1.2).

Plug and Forward Calorimeters

The plug region, $1.1 < |\eta| < 2.2$, and the forward region, $2.0 < |\eta| < 4.2$, are covered by gas calorimeters. The calorimeters contain tubular proportional wire chambers with a 50% argon and 50% ethane gas mixture as the active medium. The physical properties of the gas calorimeters are summarized in Table 2.4. The chambers contain a wire at high voltage inside a resistive plastic (plug) or aluminum (forward) tube. The cathode of the detectors are copper pads plated on G-10 board. The copper pads are constructed to form towers for the calorimeter segmentation. Figure 2.6 and Figure 2.7 show the construction of the plug calorimeter. The forward calorimeter has a similar geometry. The resolution of the gas EM calorimeters is approximately 4% to 50 GeV electrons. The gas hadronic calorimeters have a resolution of approximately 20% for 50 GeV pions.

The gas calorimeters were calibrated in a test beam of pions and electrons with known

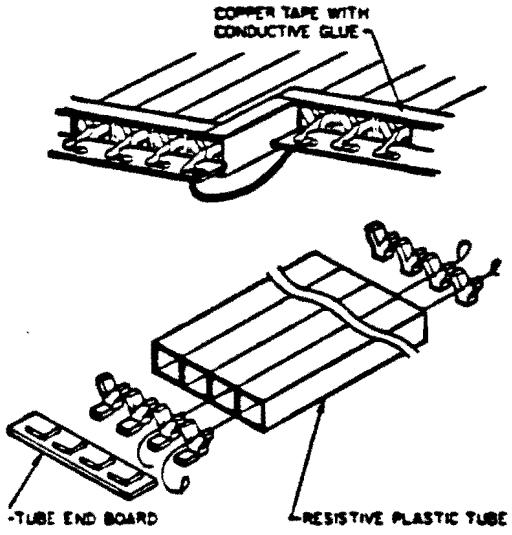

Figure 2.6: A schematic diagram showing the construction of the plug proportional chamber.

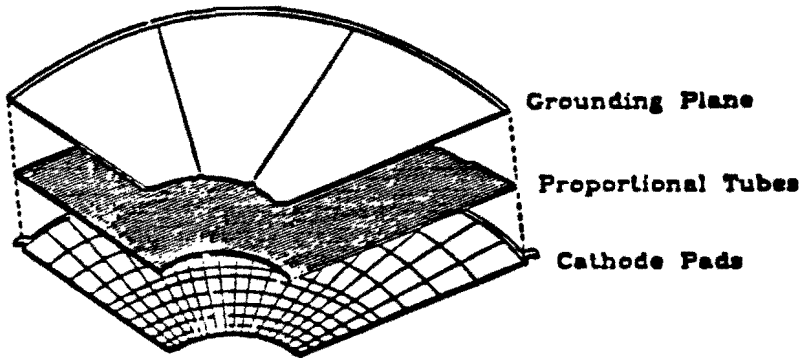

Figure 2.7: The construction of the proportional tubes, cathode pads, and grounding plane for the plug calorimeter.

	Plug (EM)	Plug (Had)	Forward (EM)	Forward (Had)
Coverage ($\|\eta\|$)	1.1 – 2.4	1.3 – 2.4	2.2 – 4.2	2.3 – 4.2
Tower Size ($\Delta\eta \times \Delta\phi$)	0.1 × 5°	0.1 × 5°	0.1 × 5°	0.1 × 5°
Active Medium	Proportional Chambers with cathode pads			
Tube Size (cm^2)	0.7 × 0.7	1.4 × 0.8	1.0 × 0.7	1.5 × 1.0
Absorber	Pb	Fe	96%Pb, 6%Sb	Fe
Thickness	0.27 cm	5.1 cm	0.48 cm	5.1 cm
Energy Resolution (σ/E at 50 GeV)	4%	20%	4%	20%

Table 2.4: A summary of the physical properties for the gas calorimeters.

energy. The response of the gas calorimeters depends on the gas density. The temperature of the gas is maintained at the temperature of the collision hall. The pressure of the gas is maintained at slightly greater than atmospheric pressure which changes with the weather conditions. To maintain a calibrated detector, the response was monitored using small proportional chamber tubes mounted on the detector. The tubes have an Fe-55 source to calibrate the gain. Adjustments were made to the detector energy scale when conditions changed.

2.1.3 Data Acquisition

Trigger

The trigger system for CDF is a multi-level system with increasing complexity at the higher levels. The lowest level trigger, Level 0, is made by a coincidence in scintillator counters positioned near the beam pipe at very low angles. The coincidence of these "beam-beam" counters was required to be within 100 ns of a beam bunch crossing at the interaction point. The decision at Level 0 was made within the 3.5 μsec between bunch crossings; therefore no deadtime was incurred.

Analog trigger signals from the detector components were brought to the trigger electronics. The calorimeter towers were summed into trigger towers of $\Delta\eta = 0.2 \times \Delta\phi = 15°$ for both the electromagnetic and hadronic calorimeters. The calorimeter E_T, and information from a hardware track processor [26] were used to make the Level 1 trigger

decision. For electrons, the Level 1 requirement was the existence of 6 GeV of E_T in an electromagnetic trigger tower. If the Level 1 trigger was not satisfied, the front end electronic circuitry was reset for the next beam crossing. On average, one beam crossing is missed during the Level 1 analysis. The average total rate out Level 1 during the 1988-89 run was a few kHz.

The Level 2 trigger used the trigger tower information with greater sophistication. The trigger towers were formed into clusters. For each cluster, the E_T, average ϕ, average η, and the ϕ and η widths were determined. This information along with tracking information was examined by a programmable Level 2 processor [27]. The processor was programed to select the interesting events containing electrons, muons, jets, and missing transverse energy (see Section 2.2.3). The requirements for the inclusive electron trigger were: (i) a cluster with $E_T > 12$ GeV in the central calorimeter, (ii) a track with $P_T > 6$ GeV/c pointing towards the cluster in ϕ, and (iii) a ratio of hadronic to electromagnetic energy deposits of less than 0.125. The Level 2 trigger decision was made in approximately 20 μsec. When the Level 3 trigger was used the event rate out of Level 2 was approximately 3-4 Hz.

The Level 3 trigger is the final level of the trigger[2]. This trigger consists of 60 Motorola 68020 processors which run the full CDF event reconstruction software including cleanup of electronic noise [28, 29]. Unlike the lower trigger levels, Level 3 had all raw data available for processing. The maximum rejection rate was approximately 60% during the 1988 - 1989 run. The electron trigger at Level 3 had the same requirements as Level 2. The transfer of data to tape limits the rate out of the highest trigger level to $1 - 2$ Hz.

Front End Electronics and Detector Readout

The front end electronics for CDF read out approximately 100,000 channels. The calorimeter readout used a "before-and-after" sampling which measured the voltage on a channel just before the beam crossing and just after the beam crossing. The difference between these voltages is proportional to the integrated charge on the channel. If the event passes

[2]The Level 3 trigger was not used at the beginning of the 1988-89 run

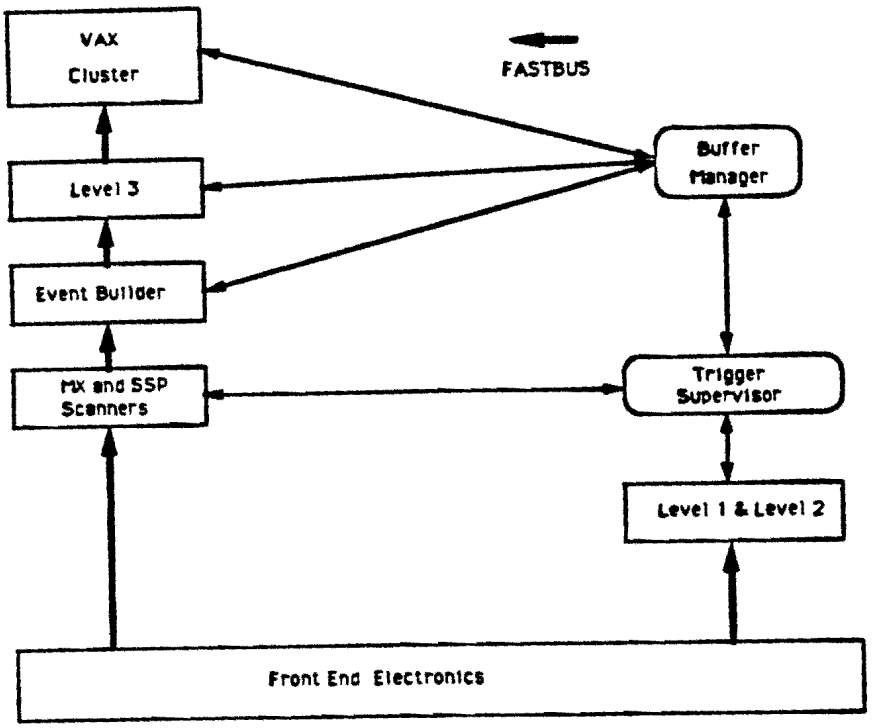

Figure 2.8: A schematic diagram of the data acquisition system. The system is based primarily on a FASTBUS network.

the Level 2 trigger, the signals were digitized in the front end electronics before being read out. The signals from the tracking systems were shaped at the detector and sent to TDC's in the counting room.

The data acquisition system is shown schematically in Figure 2.8. The system is based on FASTBUS. After the signals were digitized in the front end electronics, the data was read out and buffered by the MX and SSP scanners. The buffer manager coordinates the movement of data through the data acquisition system. The event builder collected event information from different scanners and formated the data for use by the Level 3 trigger. A host VAX accepted events from Level 3.

Separate from the data aquisition system were consumer processes which ran on the host VAX cluster and monitored the detector's performance and the quality of the data collected. Such processes included "Alarms and Limits" which monitored the component

high voltages and a separate process, "GASDAQ", which monitored the response of the gas calorimeters.

2.2 Offline Reconstruction

During the 1988 - 1989 run approximately 4.5 pb^{-1} of data were written to tape, approximately 4×10^6 events. Offline reconstruction consisted of full three dimensional tracking, cleanup of electronic noise [28, 29], calorimeter clustering, and the reduction of the raw data into useful physics quantities such as electron and jet four vectors. Selecting $W \rightarrow e\nu$ events from those written to tape is the subject of the next chapter.

2.2.1 Electron Clustering

To identify an electron and determine its energy, the offline reconstruction routines clustered energy in the electromagnetic portion of the calorimeters. The clustering algorithm began by identifying calorimeter towers as "seeds" for the cluster. A "seed" tower was identified as any tower with $E_T > 0.3$ GeV in the electromagnetic section of the calorimeter. Clusters were formed by adding adjacent towers to the cluster if the tower had $E_T > 0.1$ GeV and less energy than the seed tower E_T. If the tower had more energy than the seed tower, that tower was considered a seed tower and the process began with it. For clusters in the central calorimeter, only the towers adjacent in pseudorapidity were allowed to be added to the cluster (see Figure 2.9). Electrons deposit very little energy in adjacent ϕ towers because of the amount of material between the central wedges. Finally, the cluster was kept only if the $E_T > 5$ GeV[3] and the ratio of the energy in the hadronic calorimeter to the energy in the electromagnetic calorimeter (HAD/EM) was less than 12.5%.

2.2.2 Jet Clustering

The fragmentation of a parton forms a group of particles roughly collinear with the original parton direction. However, the transverse spread of the particles causes the energy to be

[3]The 5 GeV requirement makes the effective seed tower threshold in the central $E_T > 5/3$ GeV.

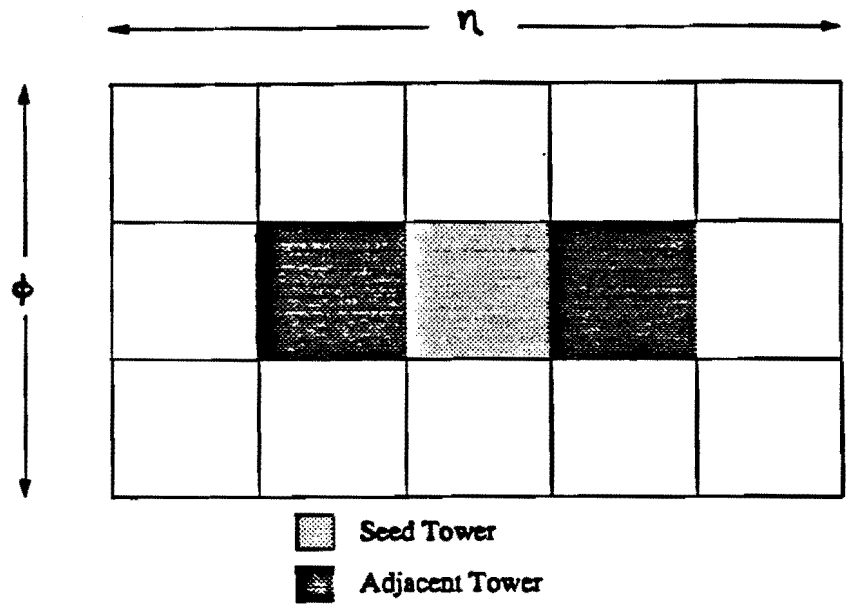

Figure 2.9: The towers used for electron clustering in the central electromagnetic calorimeter. Typically the electron showers are contained within one or two towers.

distributed over many calorimeter towers. The calorimeter towers were clustered together to find the energy from the fragmented parton [30, 31]. The clustering algorithm used a seed tower with $E_T > 200$ MeV. A cone in $\eta - \phi$ space with radius $R = \sqrt{\Delta\eta^2 + \Delta\phi^2} = 0.7$ was centered on the seed tower and all towers inside the cone with $E_T > 100$ MeV were added to the cluster. Using each tower in the cluster, the E_T weighted centroid was calculated and a new cone was formed around the centroid. The process was iterated until the list of towers in the cluster remained stable.

2.2.3 $\not\!\!E_T$ Calculation

Since a neutrino does not interact in the detector, the presence of a neutrino was inferred from an imbalance in the transverse energy deposits in the calorimeter. The imbalance is called the missing transverse energy ($\not\!\!E_T$). Offline the $\not\!\!E_T$ was calculated as,

$$\vec{\not\!\!E}_T = -\sum_i E_T^i \hat{\mathbf{n}}_i, \qquad \text{i = Calorimeter Tower with } |\eta| < 3.6 \tag{2.1}$$

where the $\hat{\mathbf{n}}_i$ is a unit vector at the tower face pointing transverse to the beam direction. The tower must have had $E_T > 100$ MeV to be included in the sum. This is identical to the threshold used for jet clustering.

Chapter 3

Event Sample

In order to measure the P_T spectrum for W's, a sample of events relatively free from background must be selected. The decay of the W into an energetic electron and neutrino provides an excellent tag which can be used to separate W's from other events. Sections 3.1 and 3.2 describe how the electron and neutrino ($\not\!\!E_T$) are selected. After identifying the electron and $\not\!\!E_T$, some background events remained in the sample. The backgrounds include jets that mimic electron signals, photon conversions ($\gamma \rightarrow e + e-$), Z's, and semileptonic decay of b and c quarks. How these backgrounds are measured and subtracted is discussed in Section 3.4. The chapter concludes with the determination of the selection efficiency and acceptance which are both important for determining the normalization for $d\sigma/dP_T$.

3.1 Electron Identification

The signal of an electron in the CDF detector is very distinct. First, the energy is deposited mostly in the electromagnetic calorimeter (Figure 3.1(a)) and the shower is usually contained within a small cluster of towers, normally 1 or 2 towers in the CEM. A track in the CTC points toward the cluster. The measured track momentum is approximately the same as the measured calorimeter energy. Finally, the track direction matches the cluster position measured by the proportional chambers in the CEM.

Jets detected by CDF normally have a signature very different from electrons (Figure

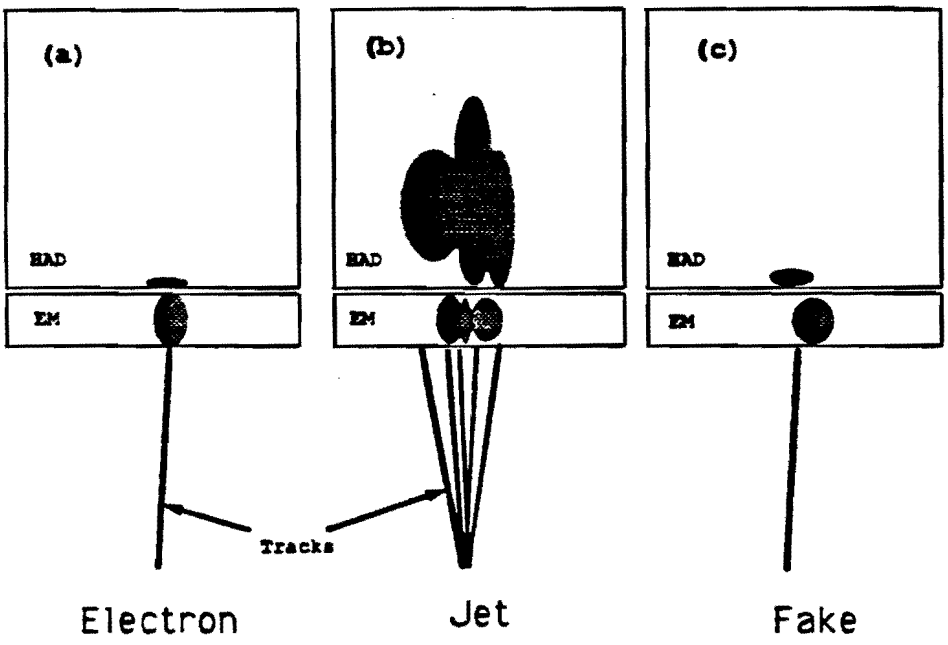

Figure 3.1: Topology of typical electron (a) and typical jet in CDF (b). Unusual jets can mimic an electron topology (c). The shaded areas represent energy deposition in the calorimeters.

3.1(b)). The energy is deposited both in the electromagnetic and hadronic calorimeters. The jet is normally distributed over a large area in $\eta - \phi$ space and many CTC tracks point toward the cluster. However, it is possible for some partons to fragment in a way which mimics an electron signal (Figure 1.1(c)). For example, if the jet energy is mostly contained in light neutral particles (e.g. π^0's), most of the energy will be deposited in the electromagnetic calorimeter. A charged particle (e.g. $\pi^{\pm}$) could provide a track which points towards the electromagnetic cluster. In order to eliminate fake electrons and eliminate real electrons from sources other than W decay, electron identification criteria must be imposed on the sample.

For this analysis, the electron was required to be in the central electromagnetic calorimeter (CEM). In this region, both tracking information and calorimeter information provided quantities for electron identification. The event selection began with events

satisfying the Level 2 electron trigger (Section 2.1.3) [1]. Approximately 10^6 electron triggers were written to magnetic tape. The following additional requirements were made on the electron:

1. Electron $E_T > 20.0$ GeV. (The electron energy was corrected for detector effects before cutting. The corrections are discussed in Section 4.1.2).

2. Within the electron cluster, the ratio of energy deposited in the hadron calorimeter (Had) to the energy deposited in the electromagnetic calorimeter (EM) was required to satisfy the following:

$$\frac{\text{Had}}{\text{EM}} < 0.055 + 0.045 * \frac{E}{100}, \tag{3.1}$$

where E is the energy of the electron cluster in GeV. The functional form was determined by studying energy deposition of electrons from a test beam. The linear term maintains the efficiency for high energy electrons which tend to have more energy in the hadronic calorimeter.

3. The ratio of the energy (E) measured by the calorimeter to the momentum (P) measured by the CTC was required to satisfy

$$\frac{\text{E}}{\text{P}} < 1.5. \tag{3.2}$$

The cut allows for some photon radiation off the electron.

4. The electron must have been well isolated. Isolation is defined as

$$I = \frac{E_T^C - E_T}{E_T} \tag{3.3}$$

where E_T^C is the amount of transverse energy inside a cone of radius $R = \sqrt{\Delta\eta^2 + \Delta\phi^2} = 0.4$ centered on the electron cluster. E_T is the electron's transverse energy. The isolation was required to be less than 0.1. This cut tends to eliminate events with electrons from sources (*e.g.* b,c quark decay) other than W decay.

[1] Since the Level 3 trigger was not present in the early part of the run and the electron requirements are the same in Level 2 and 3, the trigger requirement is placed on Level 2.

5. The electron position measured by the proportional chambers and the extrapolated CTC track position matched within the following tolerances,

$$R * \Delta\phi < 1.5\ cm, \tag{3.4}$$

$$\Delta Z < 3.0\ cm. \tag{3.5}$$

6. The lateral profile of the shower in the proportional chambers was measured by the cathode strips. The shower shape was required to be consistent with the shower shape measured for electrons from a test beam. This is quantified by performing a chi-squared comparison [32] between the two distributions and requiring

$$\chi^2_s < 15. \tag{3.6}$$

7. The lateral energy sharing (LSHR) of the calorimeter towers containing the electron shower must be consistent with the sharing measured in test beam electrons. The quality is quantified by the following relation,

$$\text{LSHR} = C \sum_i \frac{\text{E}_\text{i} - \text{T}_\text{i}}{\sigma_i} \tag{3.7}$$

   - E_i = (Energy in Adjacent Tower i)/(Energy in Seed Tower).
   - T_i = Ratio measured from electrons in a test beam.
   - σ_i = Standard deviation of the the test beam measurement.
   - $C = 0.14$, Normalization factor.

   Fake electrons tend to have clusters wider than real electron and therefore larger LSHR values. For the electron selection, LSHR was required to be less than 0.2.

8. The electron was required to be in the central fiducial volume. This volume was defined as $-0.9 < \eta < 0.9$. This does not include the outer η CEM towers. Furthermore, the extrapolated track position was required to be within 21 cm of the wedge's center. This eliminates the possibility of the electron falling in a ϕ crack between the wedges. The electron was also required to be more than 9

cm from the 90 degree crack between the central arches. The upper east CEM wedge is pierced by the cryostat for the solenoid. In this wedge, only towers with $\eta < 0.7$ were included in the fiducial volume.

9. The electron was required to emerge from a vertex with a z position less than 60 cm (2σ) of the nominal interaction point.

Each of the electron quantities is shown in Figures 3.2 & 3.3. The quantity is shown after only the trigger and E_T requirements and after all *other* electron cuts were applied. After these electron cuts,the event sample contains 4442 events. This represents an inclusive high E_T electron sample. The efficiency for the electron identification cuts and the acceptance are discusses in Sections 3.5.1 and 3.5.2 respectively.

3.2 Missing Transverse Energy Requirement

A large $\not\!\!E_T$ indicates the presence of an energetic neutrino. For W events, the $\not\!\!E_T$ spectrum is similar to the electron spectrum. To select W's from the inclusive electron sample, the $\not\!\!E_T$ was required be greater than 20 GeV. Figure 3.4 shows the $\not\!\!E_T$ distribution for the sample of high E_T electrons. The peak at small $\not\!\!E_T$ contains mostly background events including Z's. The peak near $\not\!\!E_T = 40$ GeV is consistent with the neutrino from W decay. Figure 3.5 shows the electron E_T distribution before and after the $\not\!\!E_T$ cut. Many of the events at low E_T are background which are eliminated by the $\not\!\!E_T$ cut. After the $\not\!\!E_T$ cut is applied, 2664 events remain in the sample. A typical event is shown in Figure 3.6.

3.3 Specific Background Vetos

Two types of background were identified and eliminated on an event-by-event basis. First, background events from $Z^\circ \rightarrow ee$ decay were eliminated by searching for a second electron in the event with the following qualities:

1. Had/EM < 0.1

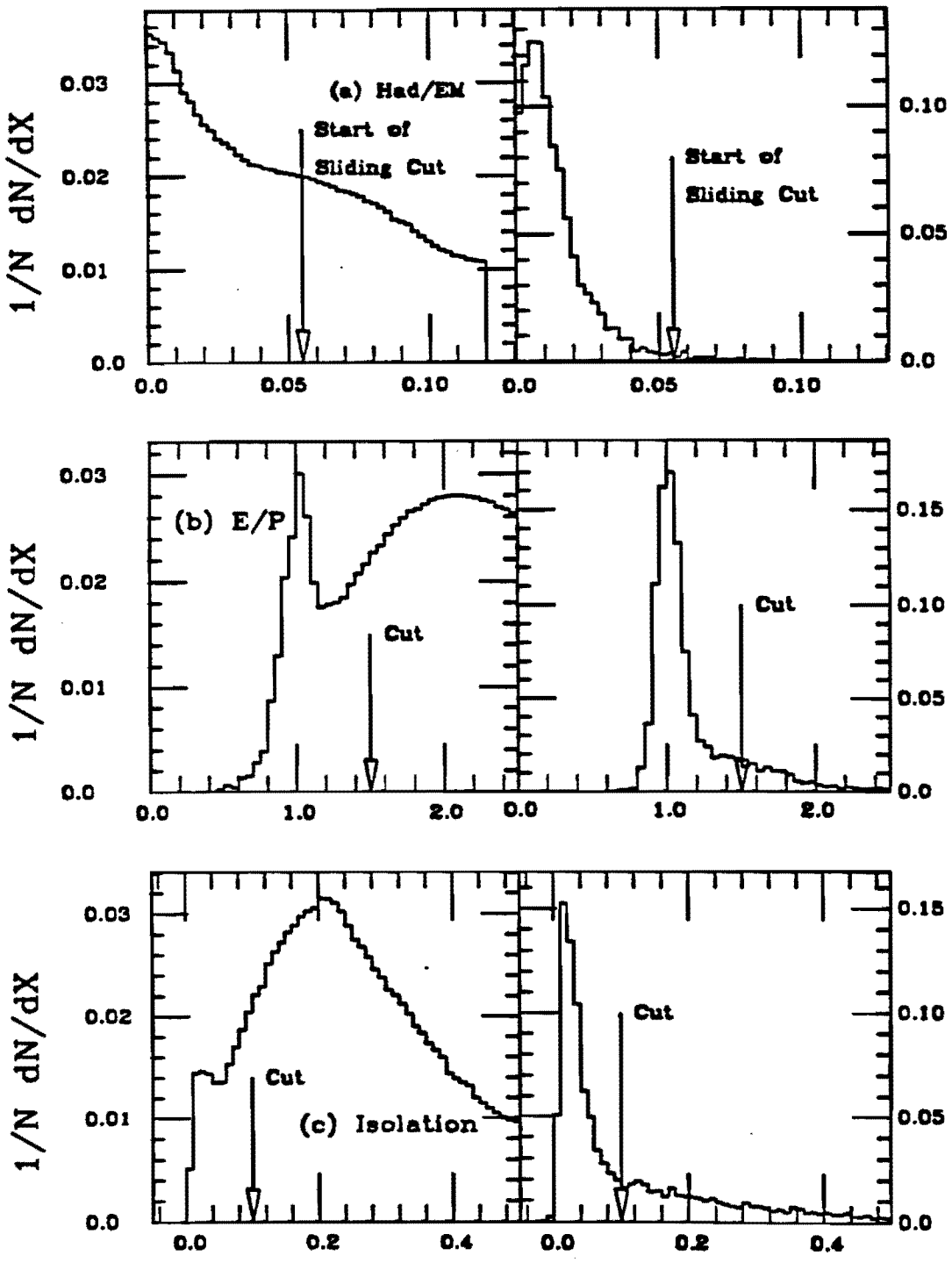

Figure 3.2: Electron Identification Quantities: Each is shown after the Electron trigger requirement and Electron E_T cut and also shown after all identification cuts *except* the cut specified. The quantities are (a) Had/EM, (b) E/P, (c) Isolation.

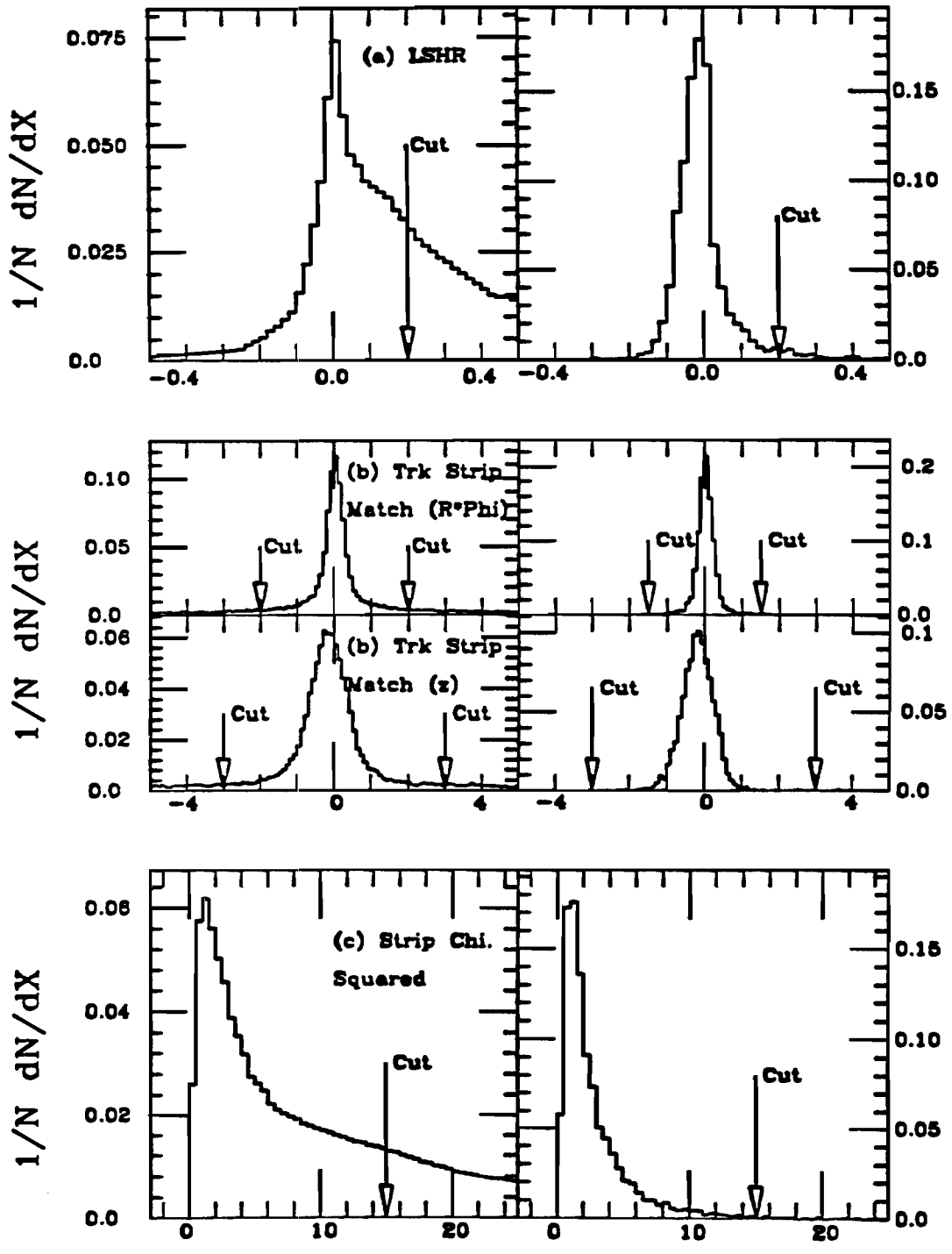

Figure 3.3: Same as Figure 3.2. The quantities are (a) Track-Strip Matching, (b) Strip Profile (χ^2_s), (c) LSHR.

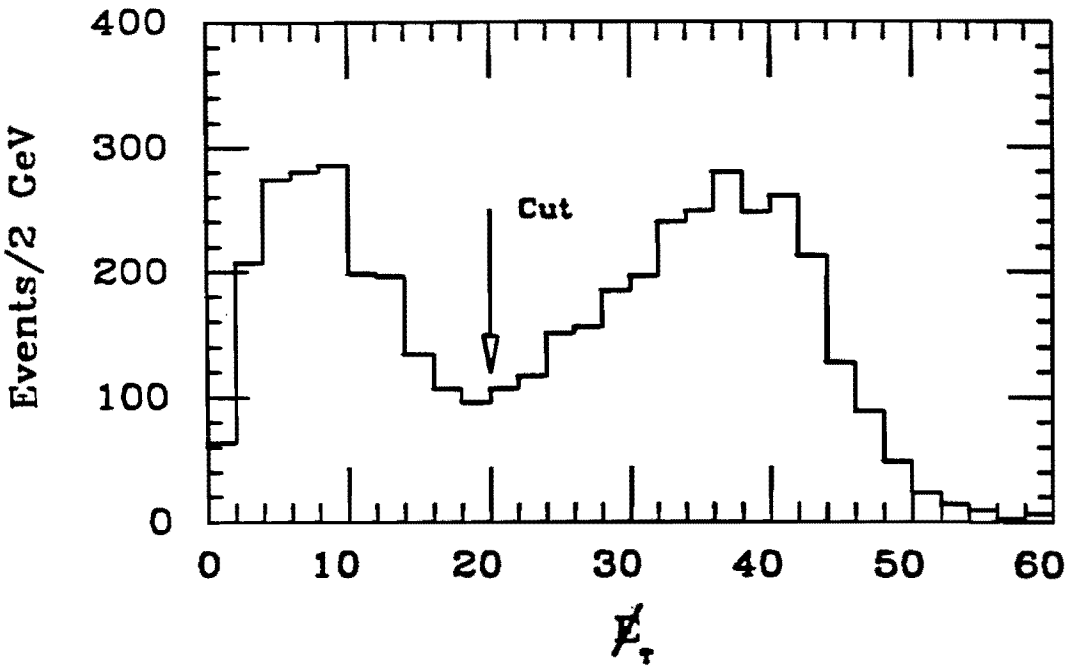

Figure 3.4: The $\not\!\!E_T$ distribution for the high E_T electron sample. The low $\not\!\!E_T$ peak contains Z events and background. The peak near 40 GeV is consistent with what would be expected from W events.

2. E/P < 2.0, if the electron is in the cental region; otherwise no cut is made.

3. If charge is known, it must be the opposite of the primary electron charge.

4. The primary and secondary electron must form an invariant mass between 70. GeV and 115 GeV. (M_Z = 91.1 GeV and Γ_Z = 2.5 GeV [33, 34, 35, 36]).

With these cuts applied, 16 events were vetoed as Z production and decay.

Next, events with a photon conversion ($\gamma \rightarrow e^+e^-$) were identified. Two methods were used to find conversions [37]. First, if the photon converted in the material between the VTPC and the CTC, no hits would be made in the VTPC. Therefore, events with less than 20% of the possible VTPC hits along the direction of the electron track were flagged as conversions. The second method required finding both the electron and positron tracks in the CTC. If two oppositely charged tracks at the same θ were approximately tangential at a common ϕ, the tracks were identified as originating from a photon conversion. In the W sample, 152 events were identified as having the primary electron coming from a photon

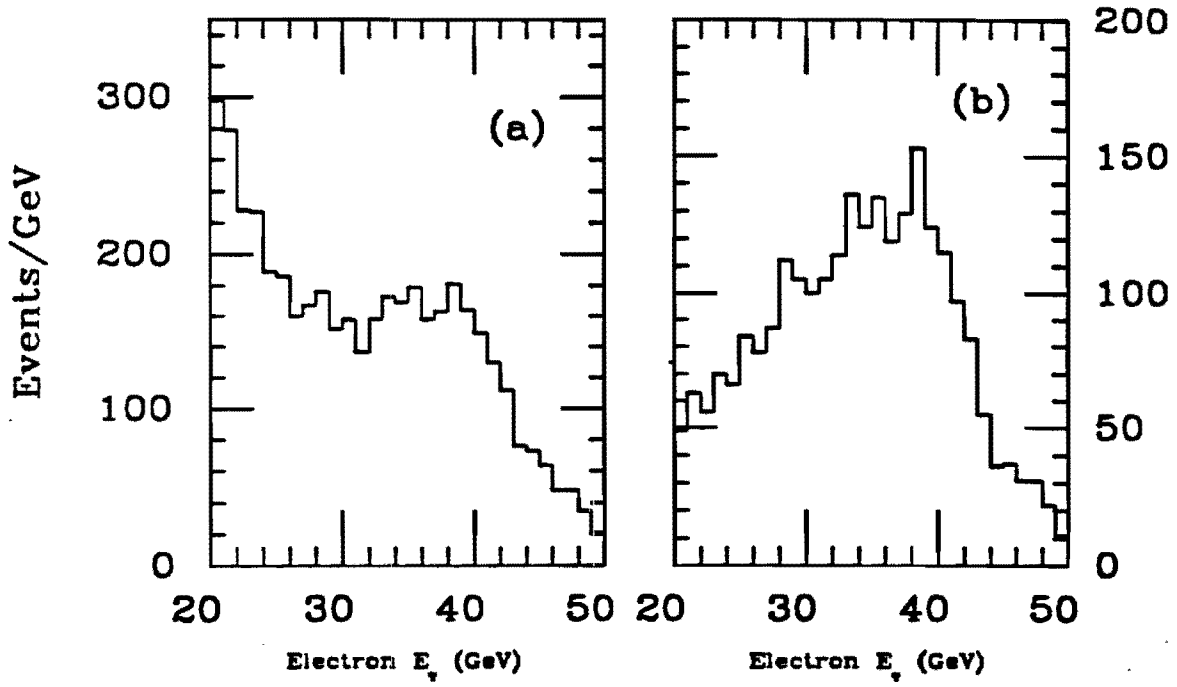

Figure 3.5: The electron E_T spectrum before and after the $\not\!\!E_T$ cut. Plot (a) shows the spectrum before the $\not\!\!E_T$ cut. The peak near 40 GeV contains both W and Z events. Plot (b) shows the spectrum after the $\not\!\!E_T > 20$ GeV requirement.

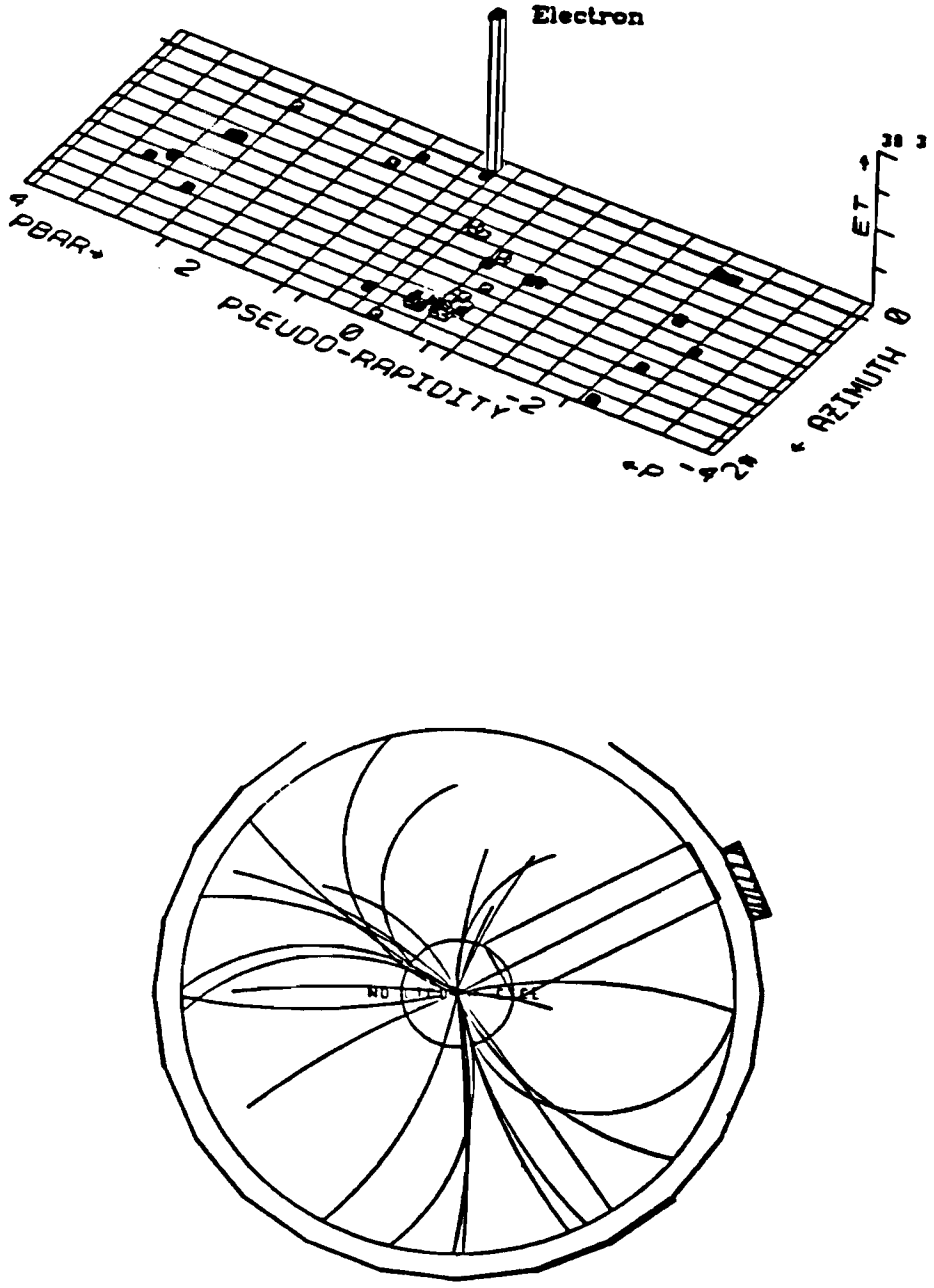

Figure 3.6: A typical W event. The upper figure shows the energy deposits in the calorimeter towers. The detector has been "unrolled" in the view. The single high E_T tower is from the electron. The lower figure shows the tracks found in the central tracking chamber. A high P_T track is pointing toward the electron cluster.

	Number of Events
Total Sample	2496
Background:	
QCD	45 ± 25
$Z \rightarrow e^+e^-$	34 ± 15
$Z \rightarrow \tau\tau(\tau \rightarrow e)$	8 ± 4
$W \rightarrow \tau\nu(\tau \rightarrow e)$	85 ± 10
Heavy Top	$0\pm^{31}_{0}$

Table 3.1: Summary of the Backgrounds Events in the final W sample.

conversion. Some of these events are real W events with the electron misidentified as a conversion electron. Section 3.5.3 discusses this over-efficiency.

3.4 Backgrounds

After all the electron identification cuts, the $\not\!\!E_T$ cut, and the background vetos, 2496 events remain in the sample. Residual background events still exist. Some of the background events could have been removed by tightening the electron identification cuts but a loss of efficiency for identifying real electrons would have resulted. Certain types of background, such as $W \rightarrow \tau\nu$ ($\tau \rightarrow e\nu\nu$)), can not be eliminated with any additional cuts. These backgrounds must be measured and subtracted from the sample on a statistical basis.

The background is divided into four sources, QCD processes including the semileptonic decay of b and c quarks, Z's, taus, and a heavy top quark. For each type, the total amount of background in the sample was measured and the background shape ($1/N\ dN/dP_T$) was determined. The shape was scaled by the total background and subtracted from the observed spectrum on a bin for bin basis. Each background type is discussed below and the total amount of background from each source is summarized in Table 3.1. The total background is less than 7% of the events in the sample.

3.4.1 QCD Background

QCD background exists from quarks or gluons which fake an electron signature (*e.g.* $\pi^{\pm}\pi^{o}$ overlap). Although the probability of such a fragmentation is small, the cross section for jet production is much larger than W boson production[2]. Also, the semileptonic decay of b quarks can contribute a *real* electron which is misidentified as coming from a W decay. Finally, conversions not found by the conversion identification procedure also contribute to this background. The background from these processes were studied by examining the electron's isolation. The electrons from W decay are more isolated than the electrons from the background since the background (*e.g.* b, c quark decay) will tend to have other particles near the electron. In order to estimate the background, a background sample was made with the following requirements:

1. "Electron" $E_T > 20$ GeV.
2. $\not\!\!E_T < 10$ GeV.
3. All standard electron cuts except the Isolation cut. (Standard Cuts: Section 3.1).
4. One or more jets with $E_T > 10$ GeV.
5. Identified conversion and Z events were eliminated.

This sample contains almost exclusively background events. The electron isolation for this sample is shown in Figure 3.7(a). The following ratio is determined for background scaling:

$$F = \frac{\text{(Number of Events with Isolation} < 0.1)}{\text{(Number of Events with Isolation} > I_c)} \tag{3.8}$$

Next, a new "signal" sample was created *without* the isolation requirement. The electron isolation for this sample is shown in Figure 3.7(b). The number of events with isolation greater than I_c was scaled by the factor F to give the number of background

[2]The probability of producing a quark or gluon with $20 < E_T < 60$ GeV is 4 or 5 orders of magnitude larger than producing an electron from a W decay.

Isolation Cut I_c	Num. $> I_c$	Scale Factor F	Num. Back. in Sample
0.20	469	0.71	45
0.25	343	0.97	49
0.30	265	1.26	44
0.35	217	1.53	49
0.40	152	2.19	48

Table 3.2: QCD Background: Scale Factors and Background Estimates

events with isolation below 0.1.

$$QCD\ Bg = F * (\text{Number of events with Isolation} > \mathrm{I_c} \text{ in the signal sample}) \qquad (3.9)$$

The value of I_c was varied between 0.2 and 0.4. The values for F and the predicted background in the final W sample are shown in Table 3.2 for the different values of I_c. The predicted background number is not sensitive to the choice of I_c.

The sensitivity to the jet requirement for the background sample was also tested. Making no jet requirement gave a prediction ($\sim$ 50 events) consistent with the 10 GeV jet requirement. However, requiring a jet with $E_T > 20$ GeV changed the prediction to 32 events. The final background from QCD processes was taken as 45 events with a systematic uncertainty of $\pm$ 25 (Table 3.1).

Finally, as a consistency check, the procedure was repeated *without* vetoing conversions[3]. The method predicts 115 background events. The seventy (70) additional events are consistent with the number of conversions eliminated by the conversion veto when the over-efficiency of the conversion identification is included (Section 3.5.3).

QCD Background P_T^W Spectrum Shape

The P_T^W spectrum shape of the QCD background was predicted from the data. A sample containing both background and signal events was created with the following cuts,

1. "Electron" $E_T > 20$ GeV.

[3]A jet with $E_T > 10$ GeV was required.

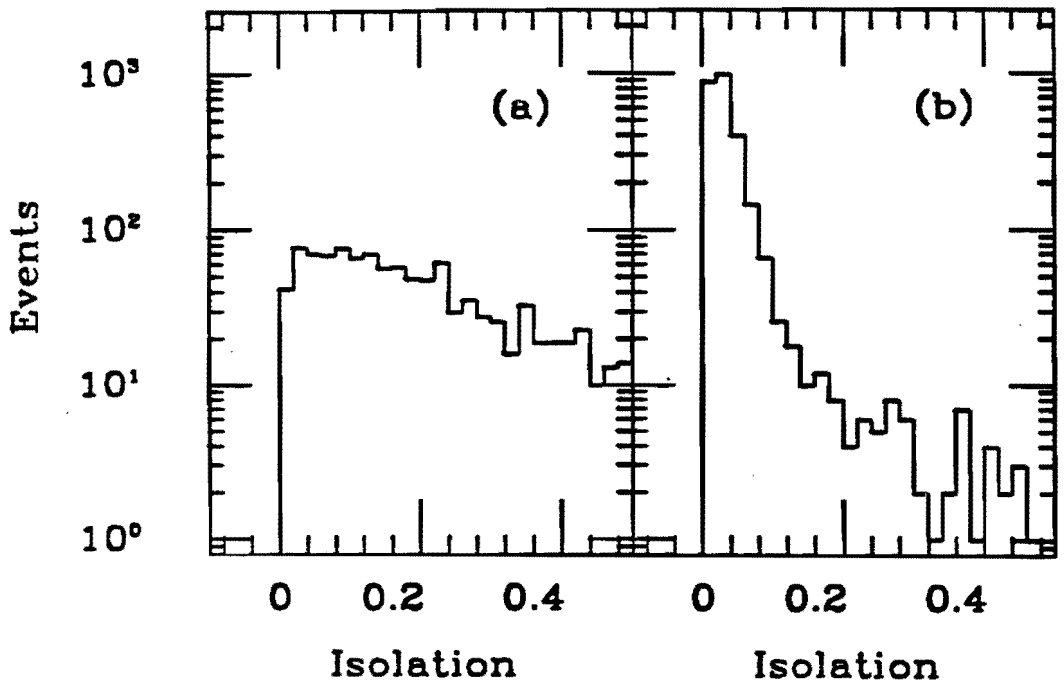

Figure 3.7: Electron Isolation for the (a) Background sample and (b) Signal sample without an isolation cut.

2. $\not\!\!E_T > 20$ GeV.

3. Isolation < 0.25.

4. Identified Conversions and Z's were eliminated.

5. Electron Fiducial Cuts.

The sample contains approximately 10^4 events. Besides the background, it also contains the 2496 events in the final sample plus the W events which are lost due to the inefficiency of the electron identification cuts. The P_T^W spectrum for this sample was created with all the electron and $\not\!\!E_T$ corrections (Section 4.1). To remove the W's from this sample, the final signal sample was scaled for the electron identification efficiency and subtracted.

$$\frac{dN_b}{dP_T} \propto \frac{dN_{b+s}}{dP_T} - \frac{1}{\epsilon} * \frac{dN_{obs}}{dP_T} \tag{3.10}$$

- $\frac{dN_b}{dP_T}$ is the P_T^W spectrum of the background.
- $\frac{dN_{b+s}}{dP_T}$ is the P_T^W spectrum of the sample containing both signal and background events.

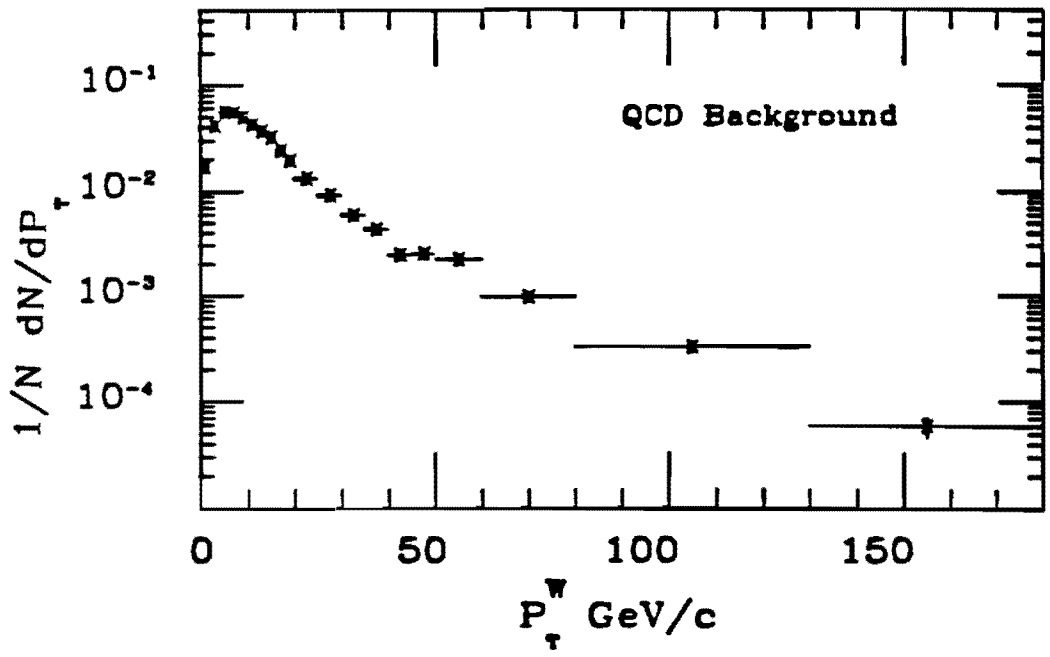

Figure 3.8: The P_T^W spectrum of the QCD background shape assumes a W topology. The distribution is determined from the data.

- $\frac{dN_{obs}}{dP_T}$ is the P_T^W spectrum of the final W sample.

The electron ID efficiency (ϵ) is 85%[4]. After the signal subtraction, the remaining P_T^W spectrum represents the background shape. The spectrum, normalized to unit area, is shown in Figure 3.8. The spectrum was scaled by the total QCD background number (45) before subtracting it from the observed P_T^W spectrum. This method depends on the electron identification efficiency being constant as a function of P_T^W. The efficiency for real electrons is constant over the observed P_T^W range (Appendix A). A small amount of background (45 events) exists in dN_{obs}/dP_T but this is a small fraction.

3.4.2 Z Background

Most Z $\rightarrow$ *ee* events were eliminated with the Z veto (Section 3.3). However, if one electron was very poorly measured or completely lost, the event was not identified as a Z event. The

[4]The efficiency is slightly larger than the efficiency found in Section 3.5.1 since the sample has an isolation cut of 0.25.

contribution of this residual Z background was estimated using the ISAJET Monte Carlo program [38]. The ISAJET program reproduces the P_T^Z spectrum observed in the data. Twenty thousand $Z \rightarrow ee$ events were generated and run through a detector simulation (QFL) [39]. The background estimate for the W sample was taken as

$$N_b^W = \frac{N_d^Z}{N_{MC}^Z} * N_{MC}^W \tag{3.11}$$

where

- N_b^W: Number of Z background events in W data sample.
- N_d^Z: Number of Z's found in the data with the Z selection (Section 3.3).
- N_{MC}^Z: Number of Monte Carlo Z's found as Z's with the Z selection.
- N_{MC}^W: Number of Monte Carlo Z's found *as W's with the W selection.*

Using the Monte Carlo events, the N_{MC}'s were determined as $N_{MC}^Z = 8202$ and $N_{MC}^W = 803$. The inclusive electron sample gives $N_d^Z = 368$. Combining the results gives a prediction of 34 $Z \rightarrow ee$ events in the W sample. This method depends on the detector simulation of the cracks in the calorimeter. Therefore, the systematic uncertainty is taken conservatively as ± 15 events to allow for uncertainty in the detector modeling. Finally, the process $Z \rightarrow \tau\tau$ also contributed to the background in the W sample. The background from this process is estimated from a Monte Carlo program as 8 ± 4 events [40].

The background shape for Z's was taken from the Monte Carlo program. Since these are Z events which are treated as W's, the P_T^W spectrum is distorted. The background P_T^W spectrum for the Monte Carlo events is shown in Figure 3.9. This spectrum was used for both the $Z \rightarrow ee$ and the $Z \rightarrow \tau\tau$ background.

3.4.3 $W \rightarrow \tau\nu$ $(\tau \rightarrow e\nu\nu)$

A W decaying to a tau and its neutrino with the subsequent decay of the tau to an electron and two neutrinos gives the topology of a $W \rightarrow e\nu$ decay. The background from this

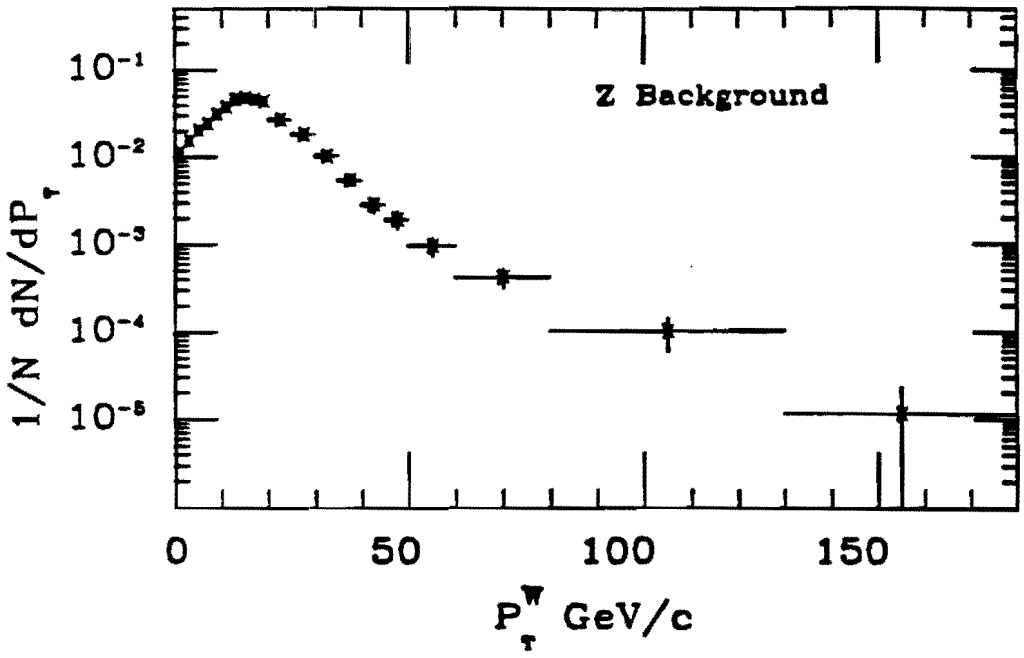

Figure 3.9: The P_T^W spectrum for Z background. The P_T^W is found with the highest E_T electron and the $\not{E}_T$. The spectrum is different from the P_T^Z of standard Z events. The distribution was determined from a Monte Carlo program with detector simulation.

source was estimated with sixty thousand (60K) $W \rightarrow \tau\nu$ events generated by the ISAJET program with detector simulation[5]. Using an integrated luminosity of 4.05 pb^{-1} for the normalization, the Monte Carlo program predicts 85 events in the W sample. The systematic uncertainty is taken as ± 10 events. The uncertainty comes from the uncertainty on the luminosity normalization and from the Monte Carlo production cross section. The shape of this background should have the same shape as the signal since the P_T^W is effectively measured from the recoil energy. However, the kinematic cuts might alter the shape of the spectrum from $W \rightarrow \tau\nu$. To check for a bias, the P_T^W spectrum from $W \rightarrow e\nu$ Monte Carlo events was compared with the P_T^W spectrum from the background $W \rightarrow \tau\nu$ events. The shapes were consistent with being identical. Therefore, the tau background was removed by a scale factor for the $d\sigma/dP_T$ normalization. The 85 events represents 3.4% of the W sample and gives a normalization scale factor of 0.966 ± 0.004.

[5]The method assumes lepton universality.

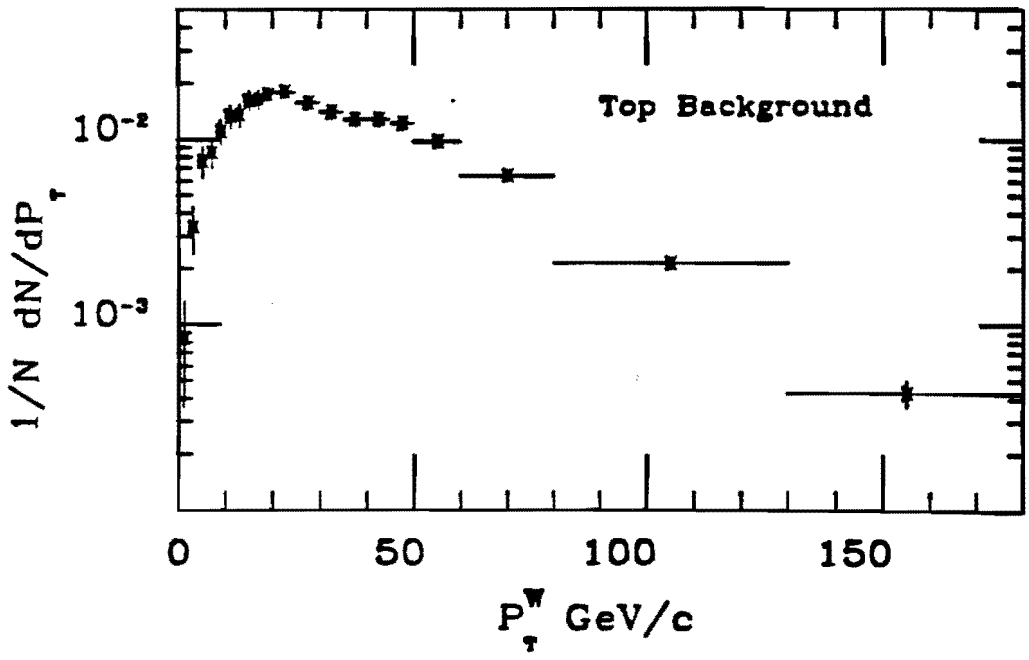

Figure 3.10: The background shape from a heavy top quark decay. The W is real; however, the P_T^W is not created by a process described by QCD. The shape was determined from a Monte Carlo program with detector simulation.

3.4.4 $t \rightarrow Wb \rightarrow e\nu b$

The decay of a heavy top quark into a real W will contribute to the inclusive differential cross section, $d\sigma/dP_T$. However, if the spectrum is compared to a theoretical QCD prediction, the contribution from the top quark decay must be included as a background. Since the top quark has not been observed, the background was taken as zero events but with a positive systematic uncertainty of 31 events. The upper systematic limit was derived by generating 30K $t\bar{t}$ events (m_{top} = 90 GeV/c^2)[6] with a Monte Carlo program (ISAJET). After all the sample selection requirements, the Monte Carlo program predicts thirty-one events would exist in our W sample. The background shape was determined from the same Monte Carlo sample. Figure 3.10 shows the background spectrum from the decay $t \rightarrow Wb \rightarrow e\nu b$.

[6]The current mass limit on the top quark is 89 GeV/c^2 [41].

3.5 Efficiencies and Acceptance

In order to properly normalize the measured differential cross section, the efficiency of the event selection cuts must be measured. In addition, the acceptance of the kinematic and fiducial cuts must also be measured. The acceptance can affect more than the normalization since it varies as a function of P_T^W. The methods used to determine the efficiencies and acceptances are discussed below along with the values determined.

3.5.1 Electron Identification Cuts

The electron identification efficiency was studied using a sample of $W \rightarrow e\nu$ events selected with strict cuts on the $\not\!\!E_T$ and the non-electron energy. The sample was selected with the following criteria:

1. Electron $E_T > 20$ GeV.
2. E/P < 10.
3. $\not\!\!E_T > 30$ GeV.
4. $50 <$ Transverse Mass < 100 GeV/c^2. (Section 1.3)
5. No Cluster with $E_T > 5.0$ GeV other than the electron.
6. Conversions Eliminated.
7. Electron Fiducial Cuts.

These cuts leave 1064 events. The transverse mass and electron E_T for this sample are shown in Figure 3.11. The nonelectron background in the sample was estimated to be less than one percent. By examining the electron quantities, the efficiencies of the electron identification cuts were measured. The results are summarized in Table 3.3. Except for the electron trigger efficiency, each efficiency given in Table 3.3 is the independent efficiency for that cut. The trigger efficiency was measured assuming the electron identification cuts had been made [42]. The overall efficiency incorporates the correlations between the different cuts. Although the electron sample was made of W's with small P_T^W, the electron efficiency was

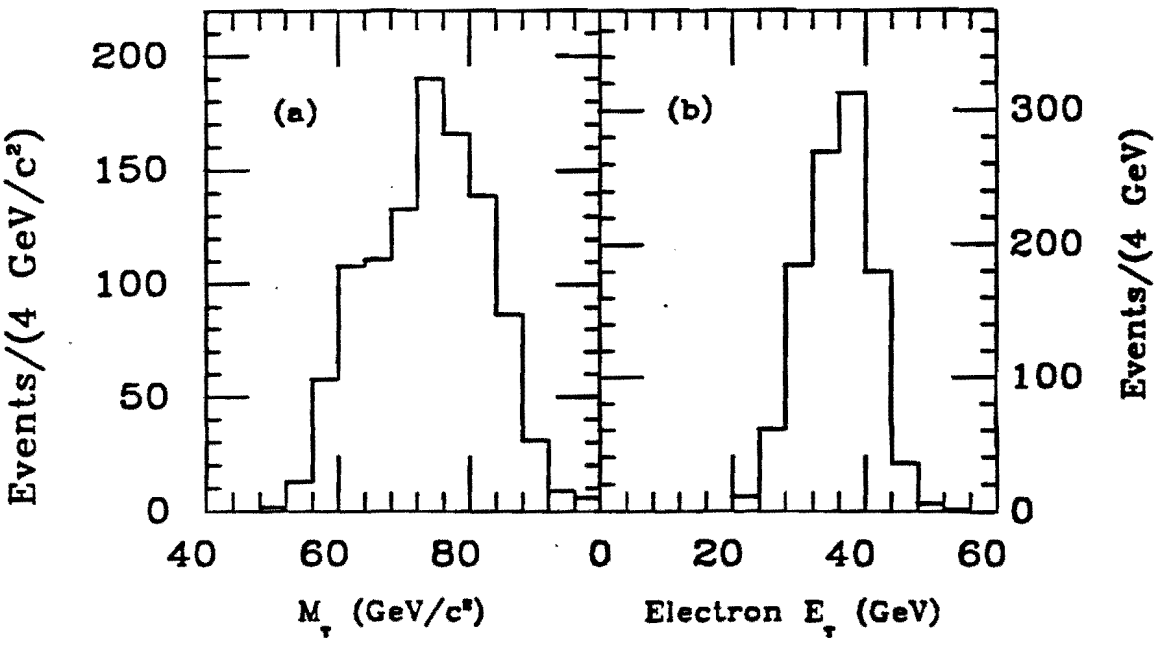

Figure 3.11: Transverse Mass and Electron E_T for sample used to measure electron identification efficiencies. The sample contains less than 1% fake electrons.

Identification Cut	Efficiency
Hadronic/EM Energy $< 0.055 + 0.045 * E/100$	99 ± 1
E/P < 1.5	93 ± 1
Track to Strip Match, $R * \Delta\phi < 1.5$ *cm*	97 ± 1
Track to Strip Match, $\Delta Z < 3.0$ *cm*	98 ± 1
Lateral Energy Sharing, LSHR < 0.2	97 ± 1
Isolation < 0.1	96 ± 1
CES $\chi^2_s < 15.$	97 ± 1
Electron Trigger	97.3 ± 0.5
Overall	84 ± 3

Table 3.3: The measured electron identification efficiencies. Each efficiency is the independent efficiency for that cut. The electron trigger efficiency is the efficiency after the other cuts are made. The overall efficiency contains the correlations among the cuts.

taken as a constant over the full range of P_T^W. This assumption is examined in Appendix A.

3.5.2 Acceptance

The kinematic and fiducial acceptances were determined using the PAPAGENO Monte Carlo program [43] which produced a W recoiling against a single quark or gluon. The final state partons were fragmented using a Feynman-Field fragmentation model [44, 45]. The detector simulation (QFL) with the offline reconstruction code gave the observed $\not\!\!E_T$ and electron E_T. The kinematic cuts were applied to the observed $\not\!\!E_T$ and the corrected electron E_T as in the event selection. The fiducial cuts were also applied to examine the geometric acceptance. Although the cuts were made on the simulated values, the generated value of P_T^W was used to determine the acceptance as a function of P_T^W. To maintain a consistent approach, the acceptance correction was applied after all $\not\!\!E_T$ and resolution corrections (see Chapter 4).

In Figure 3.12, the separate acceptances for the fiducial and kinematic cuts (E_T & $\not\!\!E_T$) are shown along with the combined acceptance. The combined acceptance shows a slow rise above the W mass due to the boosting of the electron and neutrino. Since the Monte Carlo events were generated with a jet E_T cut at 4 GeV, the very low P_T^W acceptance was checked with the ISAJET program which has a W + 0 jet contribution and therefore no threshold. The lowest value of the combined acceptance is from the ISAJET calculation. The other low P_T^W values from the ISAJET program are consistent with the points determined from PAPAGENO. The limited statistics of the ISAJET sample does not allow a comparison of the high P_T^W region. The distribution was fit to a cubic polynomial and the fit parameters are given in Table 3.4. The χ^2 per degree of freedom is 1.3. The acceptance in each bin was determined from the fit.

The systematic uncertainty was estimated by varying the structure functions and varying the energy response in the detector simulation. Different structure functions give different predictions for the number of events with the electron in the central calorimeter.

Fit: $A_c = a + b * P_T + c * P_T^2 + d * P_T^3$	Value
a	0.33
b	-0.15×10^{-2}
c	0.31×10^{-4}
d	-0.10×10^{-6}

Table 3.4: The acceptance fit parameters.

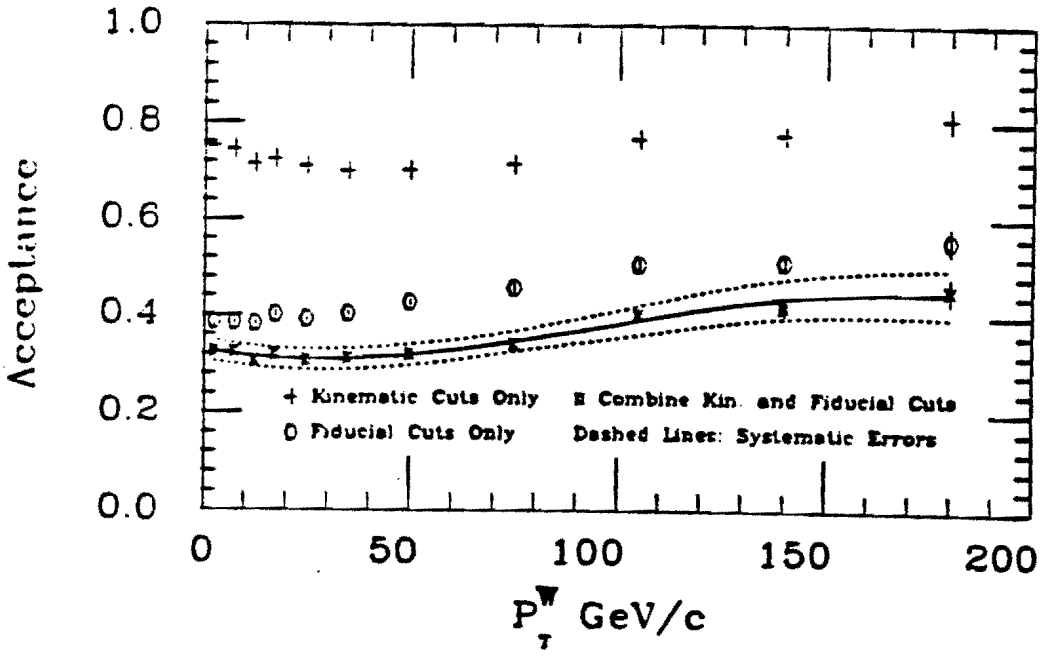

Figure 3.12: Kinematic and fiducial acceptance versus P_T^W. The kinematic acceptance and fiducial acceptance is shown separately and combined. The rise in kinematic acceptance is caused by the boosting of the electron and neutrino. The systematic uncertainty from choice of structure functions and detector simulation is shown as dotted lines.

Factor	Efficiency
Electron Identification Efficiency	84 ± 3 %
Over efficiency of Conversion Identification	3.5 ± 1.5 %
Over efficiency of Z Veto	$0.1 \pm {}^{1.0}_{0.1}$ %
Vertex Cut at 2σ	95.4 ± 0.5 %

Table 3.5: Summary of the efficiencies.

The nominal acceptance value used MRS2 structure functions [46]. The acceptance was also derived with EHLQ1, EHLQ2, and Martinelli 2 structure functions [47, 48]. For the detector simulation, the simulated $\not\!\!E_T$ resolution was worsened by a factor of 1.4, corresponding to smearing the $\not\!\!E_T$ twice. The dotted lines in Figure 3.12 enclose the variation from the structure functions and $\not\!\!E_T$ modeling. The acceptance was also measured with a Monte Carlo program (PAPAGENO) which produced a W and two jets. Within uncertainties, the results were consistent with the acceptance found with the Monte Carlo program which produces a W and one jet.

3.5.3 Miscellaneous Efficiencies

Besides the electron identification efficiency, several other efficiencies must be measured (see Table 3.5). The distribution of the z vertex position is Gaussian and the vertex cut was performed at two standard deviations, so the efficiency comes from a normal distribution. It is possible for the conversion and Z vetos to misidentify real W events as background (over-efficiency). The over-efficiency of the Z veto was estimated by performing the veto on W Monte Carlo events. The over-efficiency was measured to be $0.1 \pm {}^{1.0}_{0.1}$ %.

The over-efficiency of the conversion veto was estimated by requiring the two tracks used for the electron and positron to have the *same* charge instead of opposite charge. The method misidentified 81 events (3.1%) in the W sample as conversions. In addition, the events identified as real conversions were scanned by eye. The scanning gives an estimate between $3 - 4\%$. The over-efficiency is taken as $3.5 \pm 1.5\%$. Therefore, of the 152 events

identified as conversions, the over-efficiency predicts between 75 and 100 are real W events and between 50 and 75 are conversions. Although the conversion veto removed more signal events than background events, the *percentage* of real W's removed was constant with the P_T^W. The conversions removed, however, are *not* a constant *percentage* versus P_T^W. Therefore, the over-efficiency is easily corrected while gaining the ability to eliminate identifiable background events in the large P_T^W region.

Chapter 4

Corrections

Besides correcting for efficiencies, acceptance, and backgrounds, the observed P_T^W must be corrected for detector effects. Detector effects cause two major biases of the observed P_T^W spectrum. First, the $\not\!\!E_T$ measurement depends on properly measuring all the energy in the detector. This includes the electron energy, which is typically well measured, and the energy of the particles recoiling against the W. Although, the $\not\!\!E_T$ depends on the measuring the electron E_T, the P_T^W measurement depends only on measuring the recoil energy (see Section 4.1.2). The cracks between calorimeter towers and the nonlinear calorimeter response to low energy particles [49, 50] can cause the recoil energy to be improperly measured. This gives a contribution to the $\not\!\!E_T$ which is not from the neutrino and makes the observed $\not\!\!E_T$ an inaccurate measurement of the neutrino E_T. Second, detector resolution on the $\not\!\!E_T$ causes a bias in the P_T^W spectrum. When the resolution is convoluted with the falling P_T^W spectrum, the spectrum distorts or smears towards larger P_T^W. It is possible to correct for both these detector effects. The $\not\!\!E_T$ correction is an event-by-event correction while the resolution smearing correction is performed on the spectrum as a whole.

4.1 $\not\!\!E_T$ Corrections

4.1.1 Method

The correction is divided into three parts, each corresponding to a different energy deposition in the detector. The three parts are the electron cluster, other clustered energy (jets), and non-clustered energy (Eq. 4.1). Each part is corrected separately and the corrected $\not\!\!E_T$ is reconstructed from the three corrected pieces.

The division of energy between the different pieces must be exact to avoid either double counting or not counting energy. The electron energy is the energy deposited in the calorimeter towers containing the electron cluster. The clustered energy is the energy contained in all clusters with E_T above a threshold. Clusters falling below the E_T threshold and energy from the spectators partons compose the non-clustered energy. The raw non-clustered energy vector is defined:

$$\vec{E}_T^{nc} = -(\vec{E}_T^{ele} + \sum_{Clus}^{E_T\ Cut} \vec{E}_T^{Clus} + \vec{\not\!\!E}_T) \tag{4.1}$$

- $\vec{E}_T^{ele}$ is the contribution to the $\vec{\not\!\!E}_T$ from the towers in the electron cluster.
- $\sum_{Clus}^{Cuts} \vec{E}_T^{Clus}$ is the sum over each cluster above the E_T cut. The E_T for each jet is calculated from the energy in each cluster tower weighted by the $\sin\theta$ for each tower, where θ is determined with the z vertex position of the event.
- $\vec{\not\!\!E}_T$ is the observed missing transverse energy for the event (Section 2.2.3). The single tower threshold for the $\not\!\!E_T$ calculation is identical to the single tower threshold for the clustering of E_T^{Clus}.

Equation 4.1 assures all energy (above threshold) is counted and counted only once. Once the three pieces are corrected, the corrected $\not\!\!E_T$ is reconstructed by inverting Equation 4.1.

$$\vec{\not\!\!E}_T^{cor} = -(\vec{E}_T^{ele,cor} + \sum_{Clus} \vec{E}_T^{Clus,cor} + \vec{E}_T^{nc,cor}) \tag{4.2}$$

In this relation, the electron $\vec{E}_T$, each cluster $\vec{E}_T$, and the $\vec{E}_T^{nc}$ are corrected values. The method used to correct each piece is described in the following sections.

4.1.2 Electron Energy Corrections

The electron corrections are important for the sample selection since the electron is corrected for detector effects *before* the $E_T > 20$ GeV requirement is imposed. Also, determining the neutrino E_T requires measuring the electron properly. However, when measuring the W boson's P_T, any measurement error on the electron energy (δE_T) is fortuitously canceled by an equal and opposite measurement error of the neutrino E_T ($\not\!\!E_T$).

$$\delta \vec{P}_T = (\delta \vec{E}_T + \delta \not\!\vec{E}_T) = (\delta \vec{E}_T - \delta \vec{E}_T) = 0. \tag{4.3}$$

Nonetheless, the electron corrections are well understood and used to determine a corrected measurement of the neutrino E_T.

Several corrections were applied to the electron E_T. First, the calorimeter response is dependent on where the electron enters the tower. The response was studied using test beam electrons. A response map (Figure 2.5) was used to correct for this effect. Second, each tower in the CEM has a slightly different response. A large sample of inclusive electrons was used to determine a tower-to-tower calibration. The E/P ratio was examined for the electrons entering each tower. A tower correction factor was determined by requiring the E/P have the expected distribution [51]. This effectively calibrated the CEM to the tracking chamber. The tracking chamber was calibrated using muon tracks from ψ and Υ decays [51]. The difference between corrected E_T and measured E_T for the electron is usually less than 4%. After all corrections are made to the electron energy, the uncertainty on the energy scale is 0.4% [52].

4.1.3 Clustered Energy Corrections

The correction to the clustered energy is perhaps the most important correction to the $\not\!\!E_T$ and P_T^W. It is the dominate source of measurement error. The method involves determining an energy correction for a cluster in the central calorimeter. In the central, the calorimeter response can be determined by using the tracking information to study the E/P for low energy particles. The correction then must be extended to the remaining parts of the

detector. A response map which is a function of detector η was determined by balancing the E_T in events with two jets [53]. One of the jets, the reference jet, was contained in the central calorimeter. A second jet, the probe jet, was allowed to fall anywhere in the detector. By requiring the E_T of the two jets to balance, the calorimeter response of the probe jet allows the determination of a relative correction from any part of the detector to an equivalent central detector response. This response map corrects for the low cluster response in the cracks between the major detector components, such as the two central arches (90° crack) and the endwall and plug calorimeters (30° crack).

In order to determine the response of the central calorimeter to particles from the fragmentation of a parton, both the parton fragmentation characteristics and the calorimeter response for low energy particles must be known. The parameters of a fragmentation model were adjusted so a Monte Carlo program reproduced the jet fragmentation observed in the W sample (see Appendix B) [54, 55]. In addition, the energy flow from the underlying event was adjusted to reproduce the observed data values. The low energy calorimeter response was determined from test beam data and by studying the E/P for low energy particles in minimum bias events [49, 50]. A Monte Carlo with detector simulation convoluted the fragmented parton with the measured calorimeter response to produce an observed clustered energy.

To determine the correction factor for the energy of a cluster in the central calorimeter, partons incident on the central calorimeter were generated with flat E_T spectrum ranging from 1 to 200 GeV. The partons were fragmented and the detector simulation provided an observed cluster E_T. Clusters passing the following cuts were used to determine the clustered energy correction:

1. $0.15 < |\eta_{detector}| < 0.9$. This restricted the cluster to the central calorimeter.
2. The generated parton direction and the cluster axis had $\Delta R \leq 0.5$.
3. No other cluster within $\Delta R \leq 1.5 * 0.7$. This eliminates partons which have a strange fragmentation such that two clusters were formed. Less than 6% of the events failed this requirement. Most often the event failed because the underlying

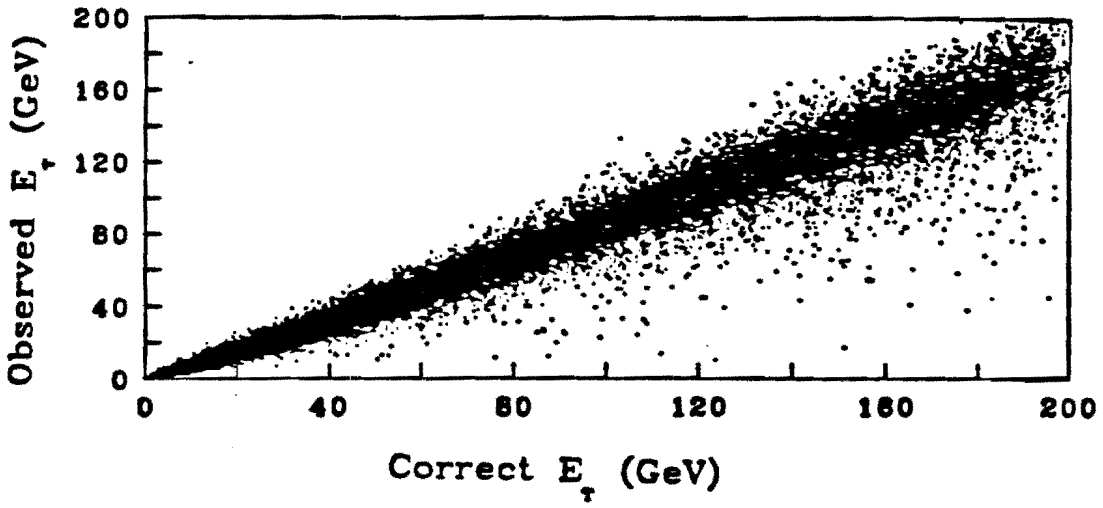

Figure 4.1: A scatter plot of the observed Cluster E_T versus energy generated inside the clustering cone.

event energy had fluctuated up to form a nearby cluster.

The observed clustered energy was corrected to the energy incident on the calorimeter within the clustering cone (see Section 2.2.2). The energy inside the clustering cone originated from either the parton or the low E_T particles from the spectator partons (underlying event). To determine the amount of energy entering the calorimeter, each final state particle was projected through the magnetic field using its initial momentum. The *initial* momentum of all particles hitting the calorimeter inside the clustering cone were summed vectorially. The vector sum represents the correct cluster E_T.

A scatter plot of correct cluster E_T versus the observed cluster E_T is shown in Figure 4.1. This plot was used to derive the correction for the clustered energy. Slices were taken in correct E_T and the projection of each slice was fit to a Gaussian distribution. The projection was refit using only those bins within 1.5σ of the mean. This was iterated until the mean and sigma stabilize to 1% and 5% respectively. This procedure eliminated effects from non-Gaussian tails. Once the mean for each slice was determined, the means were fit to a quadratic polynomial to give the following relation between observed and correct E_T.

Variable	Fit (Low)	Fit (High)
Quadratic Term (A)	1.39×10^{-3}	1.71×10^{-4}
Linear Term (B)	0.724	0.859
Constant Term (C)	−0.500	−4.18

Table 4.1: The best fit parameters for the cluster correction. Two ranges of the spectrum are fit separately. The low range is from 7 to 75 GeV and the high range is from 65 to 185 GeV.

$$E_T^{obs} = A * (E_T^{cor})^2 + B * E_T^{cor} + C \tag{4.4}$$

This expression was inverted to give a correction from observed E_T to corrected E_T.

In order to get a good fit, it was necessary to fit two regions of the jet spectrum separately. The region from 7 GeV to 75 GeV and the region from 65 GeV to 185 GeV were fit. Table 4.1 gives the fit parameters for both regions and Figure 4.2 shows the fits. A 10 GeV overlap between the two fit regions provided a nearly continuous transition from the low E_T correction to the high E_T correction. The cross point was taken in the middle of the overlap region at 70 GeV of generated energy[1]. The difference between the two parameterizations at 70 GeV is approximately 200 MeV. The residuals of the fits on either side of 70 GeV are approximately 800 MeV. The correction is a 25% correction at $E_T^{obs} = 50$ GeV and a 16% correction at an $E_T^{obs} = 150$ GeV.

The E_T threshold for correcting clusters is set at 10 GeV observed energy. Clusters with $E_T < 10$ GeV were included in the non-clustered energy. The 10 GeV cut was a compromise between setting the cut as low as possible and staying in a region where the correction is reliable and fluctuations from the underlying event are kept small. The systematic uncertainty for the clustered energy correction is discussed in Section 4.3.1.

4.1.4 Non-clustered Energy Corrections

The non-clustered energy represents the energy from low energy particles which fall outside the clustering cones. These particle can be recoiling against the W just as the particles in the

[1]This corresponds to an observed $E_T = 57$ GeV.

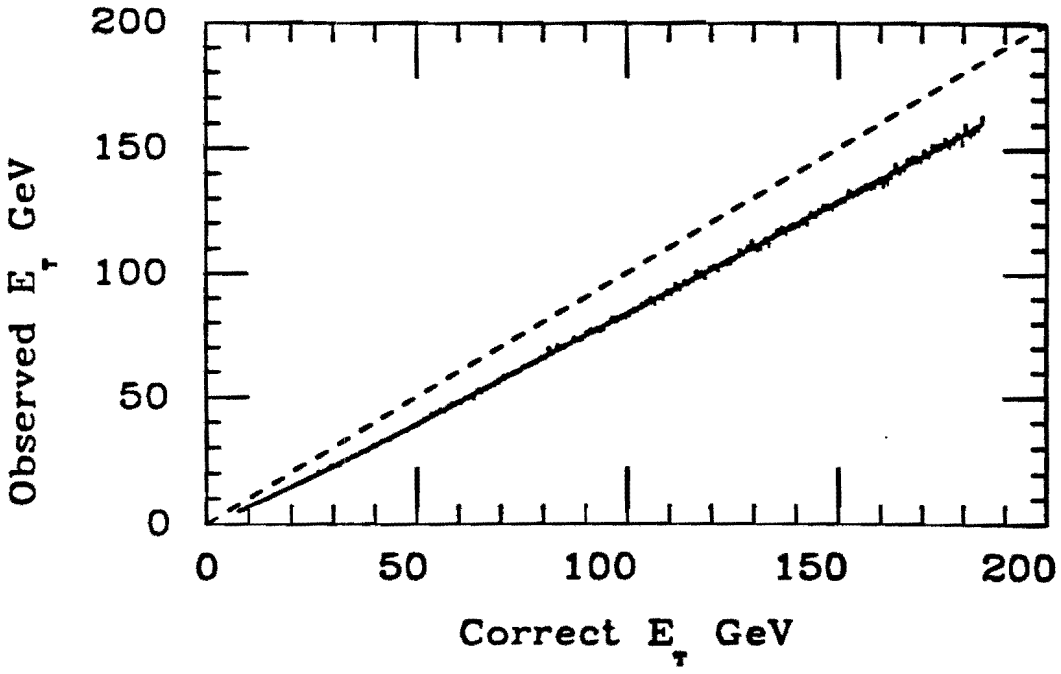

Figure 4.2: Observed clustered energy versus correct energy. The value at each E_T is the mean of a Gaussian distribution fit to a 1 GeV slice in E_T^{Cor} of Figure 4.1. The means are fit to a quadratic polynomial. A separate fit is performed for the large E_T range. The dashed line is a 1:1 line and the solid line is the fit. The fit parameters are given in Table 4.1

clusters. Although the non-clustered energy is small compared to the energy in the clusters, it is important to determine this energy as precisely as possible. This is especially true for events with a small P_T^W and no high E_T clusters. The non-clustered energy experiences the same measurement problems as the clustered energy.

The technique for determining the non-clustered energy correction is similar to the method for finding the cluster correction. First, a Monte Carlo program which was adjusted to reproduce the observed jet fragmentation and the observed energy flow from the underlying event[2] was used to determine a generated (correct) value of $\vec{E}_T^{nc}$. Second, a detector simulation (QFL) convoluted the generated particle momentums with the measured detector response to produce an observed value for $\vec{E}_T^{nc}$. The observed and generated values of $\vec{E}_T^{nc}$ were compared to find a correction factor.

A Monte Carlo program (PAPAGENO) with Feynman-Field fragmentation of the partons was used to generate events with a W along with one or two jets. The events were created with the following requirements:

1. P_T of the quark or gluon > 4.0 GeV/c.
2. $|\eta_{detector}| < 3.5$
3. The minimum separation between different quark and/or gluons: $\Delta R > 0.6$.

Only events with 1 (2) cluster(s) above 10 GeV for W + 1 (W + 2) jet events were examined. The observed non-clustered energy vector was calculated using Equation 4.1. For the generated non-clustered energy vector, all final state particles with $|\eta_{detector}| < 3.5$ and falling outside all clustering cones were used. As in the cluster correction, the particles were projected through the magnetic field. Particles which do not enter the calorimeter because they curl up in the magnetic field were included in the generated non-clustered energy. The *intial* momentum of each particle was used to calculate the generated $\vec{E}_T^{nc}$.

The non-clustered energy vector was broken into components parallel and perpendicular to the observed W direction. The observed and generated values were scatter plotted.

[2]See Appendix B

Cor = S_{nc} * Observed	
Component	S_{nc}
W + 1 Jet Par. Comp	2.01
W + 1 Jet Perp. Comp	1.85
W + 2 Jet Par. Comp	1.90
W + 2 Jet Perp. Comp	2.07

Table 4.2: The best fit parameters for the non-clustered energy correction. A correction factor, S_{nc}, equal to 2.0 is used for all components.

Slices made in the *generated* E_T^{nc} were fit to Gaussian distributions. Like the clustered energy correction, an iterative procedure was performed to find a stable mean and sigma and eliminate non-Gaussian tails. The means were fit to a line passing through the origin. The slope gives the inverse of the correction factor (S_{nc}) for observed to generated. The results are summarized in Table 4.2. A correction factor, $S_{nc} = 2.0$, is used for *all* components of the non-clustered energy ($\vec{E}_T^{nc}$) [56]. The uncertainty of the scale factor is determined from the data (see Section 4.3.2).

4.2 Verifying the $\not\!\!E_T$ Correction

The next step is to verify that the $\not\!\!E_T$ correction performs properly. The correction was tested using several control samples from the data. A sample of $Z \rightarrow ee$ events was the most direct test of the correction. However, the low statistics of high P_T Z's reduced the quality of the test. A sample of events with a photon conversion provided a high statistics check of the cluster correction. Finally, the application of the correction to a sample of inclusive electrons gave some qualitative tests.

4.2.1 Checks with Conversion Electron Events

Events identified as containing a photon conversion should have $\not\!\!E_T \simeq 0$ since any neutrinos from the fragmentation products will have a very low energy. The $\not\!\!E_T$ can be examined before and after the energy corrections are applied. Most conversions are photons from π^o decays and have a jet(s) recoiling against them (see Figure 4.3). The jet(s) forms a

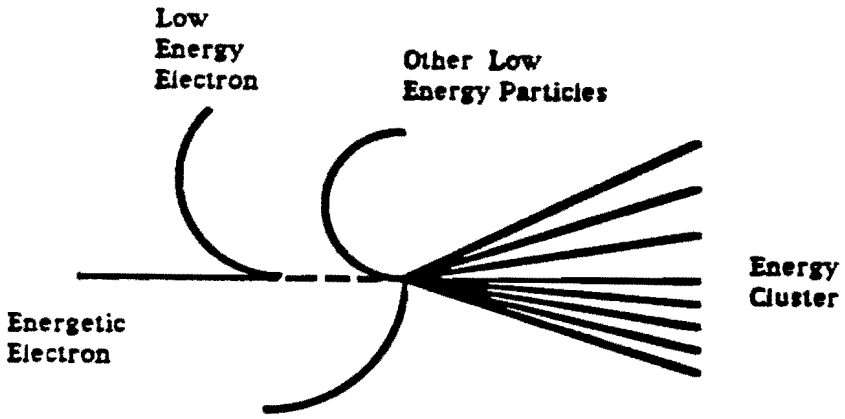

Figure 4.3: Schematic drawing of a typical conversion event. The energy cluster opposite the conversion will tend to be mismeasured low and cause a false $\not\!\!E_T$ in that direction.

cluster(s) of energy which tends to be mismeasured low because of cracks between the detectors and the nonlinear calorimeter response. This mismeasurement introduces a false $\not\!\!E_T$ in the cluster direction. To examine this mismeasurement, a sample of conversion events was selected with the following requirements:

- Primary Electron identified as originating from a photon conversion.
- Primary Electron $E_T > 20$ GeV (Corrected).
- Primary electron E/P < 2.0.
- Had/EM < 0.055 + 0.045*E/100.
- Isolation < 0.1.
- $|Z_{Vert}| < 60$ *cm*.
- Electron Fiducial Cuts.

Figure 4.4 shows the $\not\!\!E_T$ parallel to the conversion electron as a function of the primary electron E_T and therefore a weak function of the cluster E_T. The observed value shows

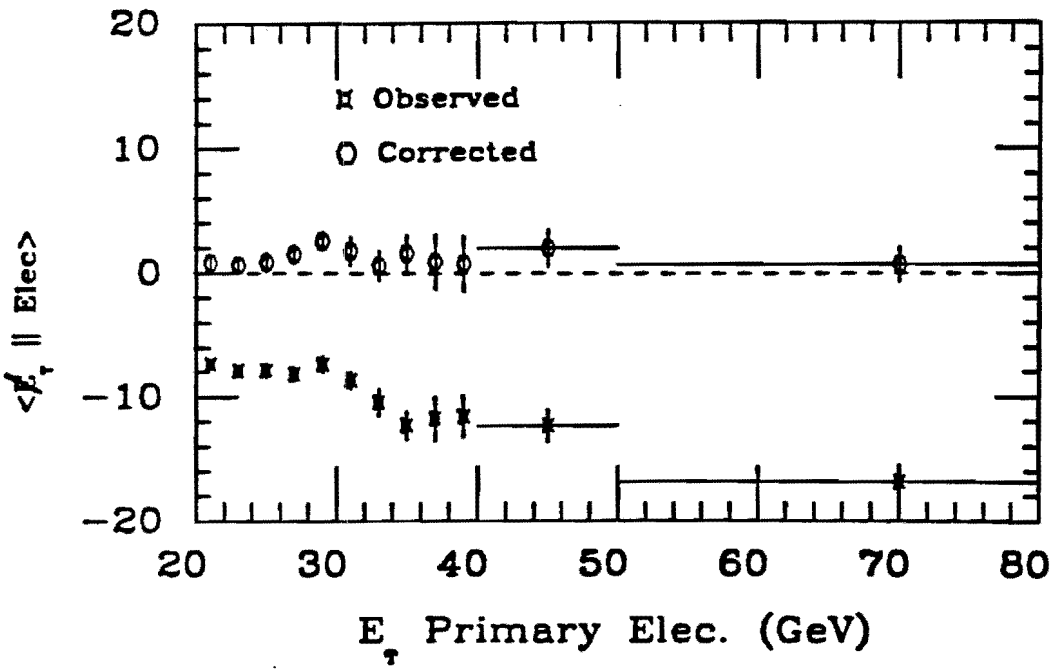

Figure 4.4: The average $\not\!\!E_T$ in the electron direction for different values of the primary electron E_T. The values are shown before and after the $\not\!\!E_T$ corrections were applied.

a large $\not\!\!E_T$ opposite the conversion electron indicating the low calorimeter response of the cluster. After correction, the distribution is flat and centered slightly above 0 GeV. Figure 4.5 shows the projection with a fit to a Gaussian distribution whose mean = 1.1 ± 0.18 GeV and σ = 7.9 GeV. The excess of events on the low side are real W events misidentified as conversions whose contribution the fit tends to ignore. The fact the conversions are centered above 0.0 GeV can be attributed to several possibilities. First, the second electron from the conversion can be trapped in the magnetic field and cause up to 0.5 GeV of $\not\!\!E_T$ in the direction of the primary electron. Second, the conversion events are typically two jet events which contain a more active underlying event than do W events. Since the cluster correction was determined assuming a W underlying event, the correction is somewhat biased for conversion events. The $\not\!\!E_T$ perpendicular to the conversion electron direction is shown in Figure 4.6. This quantity is centered at zero and remains centered after the correction. However, after correction the distribution is wider because of the energy scaling.

Primarily, the conversions provide a test of the clustered energy correction. The $\not\!\!E_T$ parallel to the conversion electron direction is not sensitive to the choice of S_{nc} because the

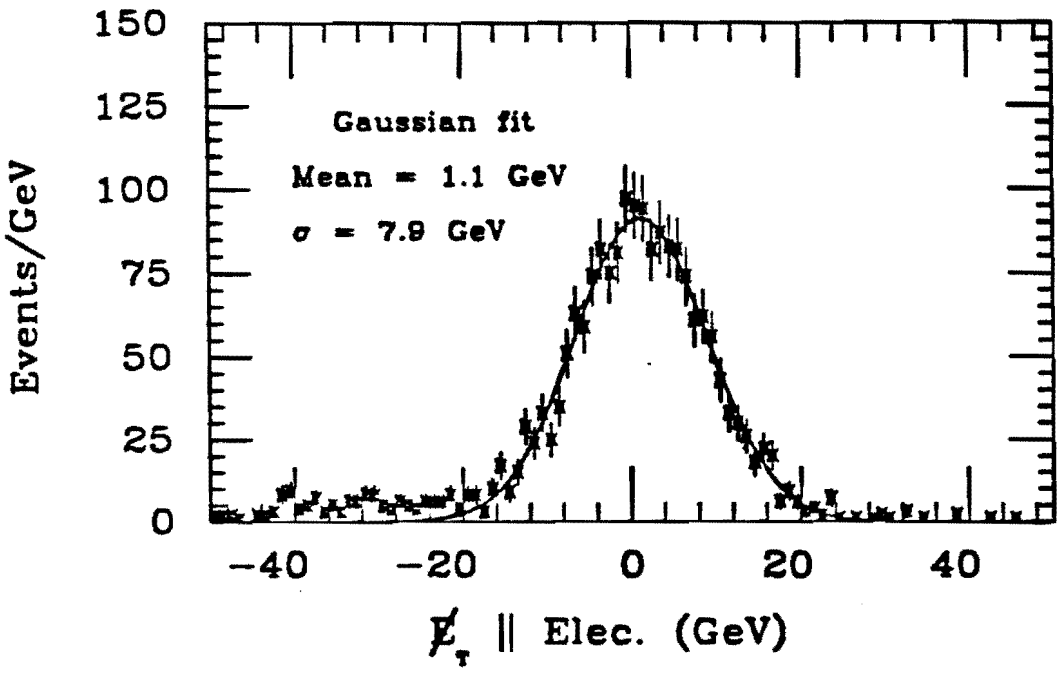

Figure 4.5: The $\not\!\!E_T$ parallel (||) to the primary electron direction in the conversion sample. The tail at large negative $\not\!\!E_{T,||}$ is caused by W events with the electron misidentified as a conversion. A fit to a Gaussian distribution tends to ignore the contribution from these events.

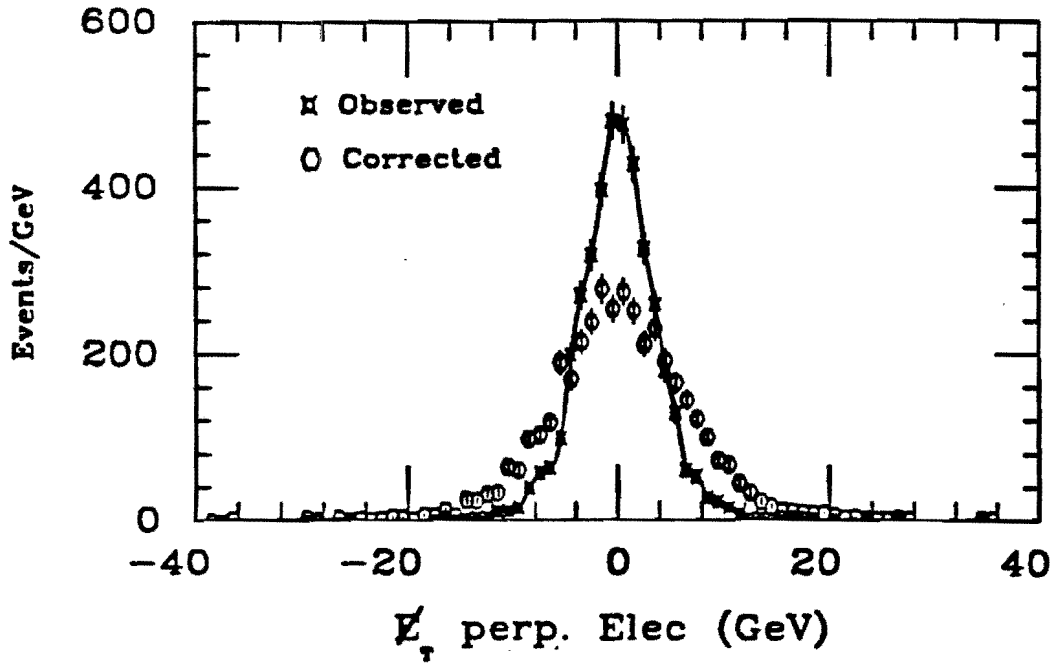

Figure 4.6: The $\not\!\!E_T$ perpendicular to the primary electron direction. This quantity is centered on 0.0 GeV before and after the $\not\!\!E_T$ corrections.

clustered energy deposits are much larger than $\vec{E}_T^{nc}$. Figure 4.7 shows the $\not\!\!E_T$ when the standard correction is applied, ($S_{nc} = 2.0$), and when the non-clustered correction is not performed ($S_{nc} = 1.0$). Very little difference exists. The flat distribution of the $\not\!\!E_T$ (Figure 4.4) is regarded as an indication the cluster correction is performing properly.

4.2.2 Checks with the Z → *ee* Events

The $\vec{E}_T$ of the electrons from a Z → *ee* decay provide an accurate measurement of the Z boson's P_T. The P_T^Z can also be measured by the calorimeter energy other than the electrons (recoil energy).

$$\vec{P}_T^{rec} = \vec{\not\!\!E}_T + \sum \vec{E}_T^{ele} \tag{4.5}$$

The P_T^{rec} is susceptible to the same measurement error as the P_T^W in W events. To determine the corrected P_T^{rec} for the Z, the calorimeter cluster energy was corrected using the correction described in Section 4.1.3. The observed non-clustered energy ($\vec{E}_T^{nc}$) was calculated with the definition given in Equation 4.1 except a sum of the $\vec{E}_T^{ele}$'s from the two Z electrons

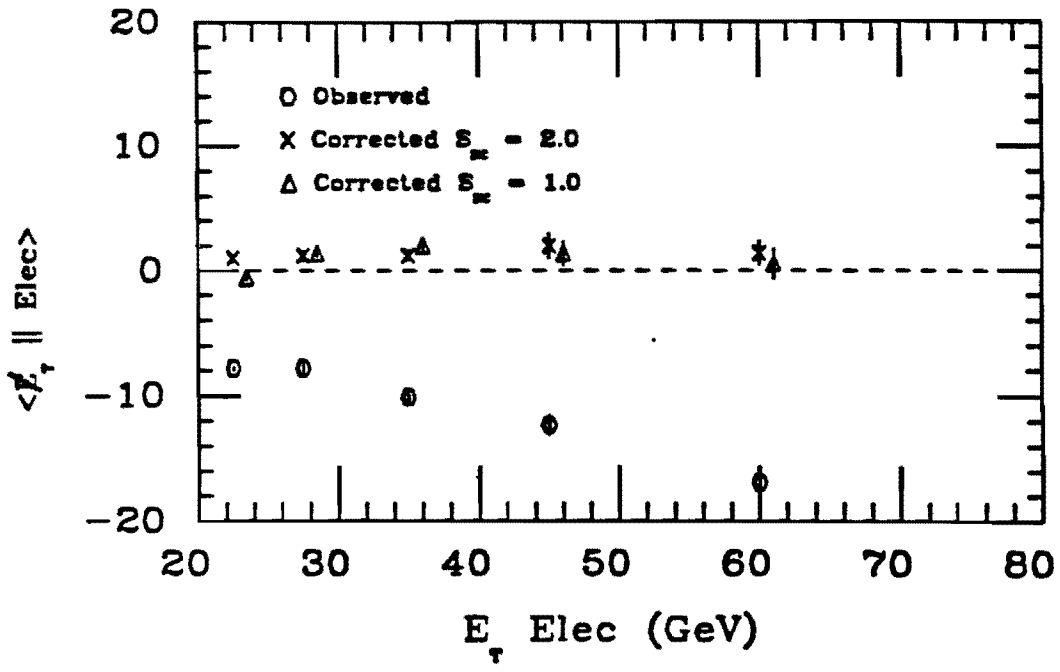

Figure 4.7: The $\not\!\!E_T$ balancing with different assumptions for the $\vec{E}_T^{nc}$ correction. The plot shows the results' insensitivity to the choice of non-clustered energy scale factor, S_{nc}, because the $\vec{E}_T^{nc}$ is small compared with the cluster E_T.

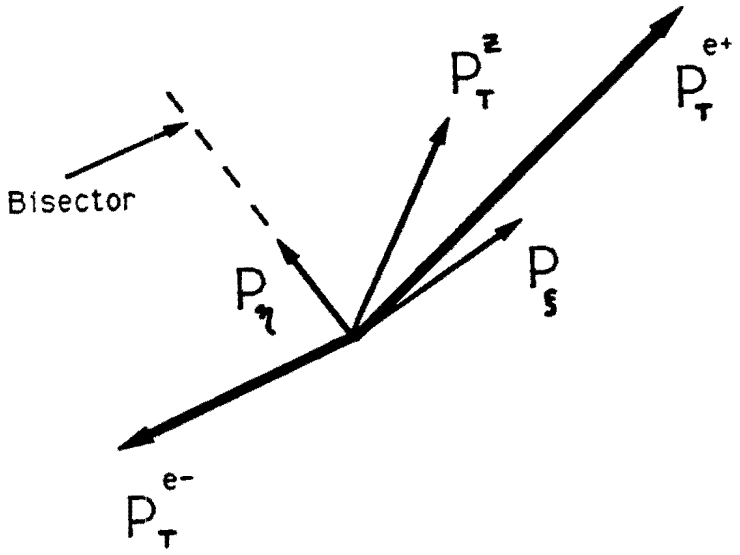

Figure 4.8: Definition of components for the Z analysis. The component P_η is less sensitive to mismeasurement of the electrons' E_T than the component P_ξ.

was used in place of the single $\vec{E}_T^{ele}$ from the W electron. The non-clustered energy was corrected with $S_{nc} = 2.0$. Combining the corrected clustered energy and the corrected non-clustered energy gives the corrected P_T^{rec} for the Z. For the Z's, it is useful to examine the components perpendicular (P_ξ) and parallel (P_η) to the bisector of the electrons (Figure 4.8). The component P_η is less sensitive to mismeasurements of the energy of the electrons than P_ξ.

To test the calorimeter corrections, the difference between the P_η measured by the electrons (P_η^{ee}) and the P_η measured by the recoil energy (P_η^{rec}) was examined. Figure 4.9 shows the average $P_\eta^{ee} - P_\eta^{rec}$ vs P_η^{ee}. The final bin in Figure 4.9 which extends from 20 to 50 GeV/c is plotted at the mean P_η^{ee} (28 GeV/c) for the events in that bin. The observed values lying above 0.0 GeV/c indicate the calorimeter measurement of the P_η is systematically low. Figure 4.10 shows the projection of $P_\eta^{ee} - P_\eta^{rec}$. A fit to a Gaussian distribution gives a mean of 0.09 ± 0.32 GeV/c and $\sigma = 4.8$ GeV/c. The same quantity for Z events with jets was examined. Figure 4.11 shows $P_\eta^{ee} - P_\eta^{rec}$ for events containing a cluster(s) with $E_T > 10$ GeV. Before the correction, the fit gives a mean of 3.5 ± 0.9 GeV/c.

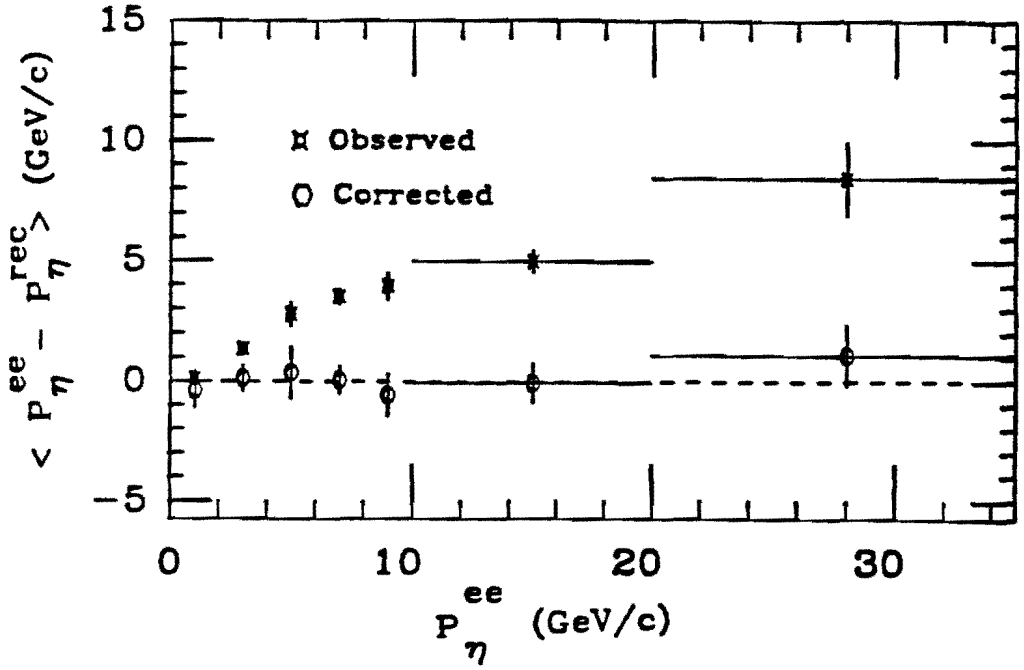

Figure 4.9: The average difference, $P_\eta^{ee} - P_\eta^{rec}$, for different ranges of P_η^{ee}. The quantity is shown before and after the energy corrections were applied.

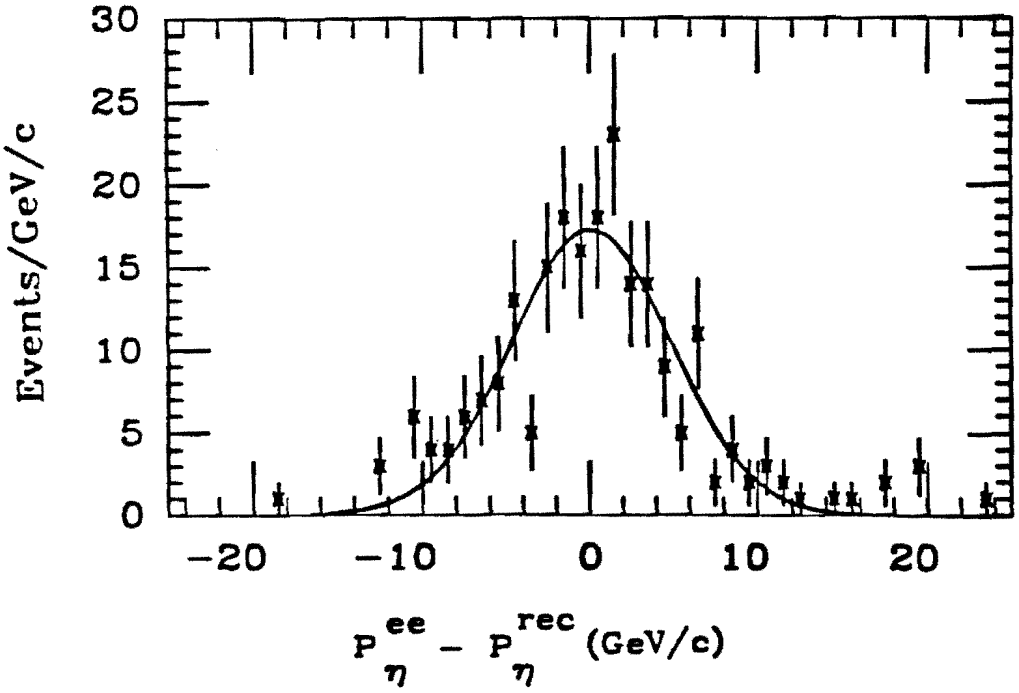

Figure 4.10: The difference, $P_\eta^{ee} - P_\eta^{rec}$, fit to a Gaussian distribution after calorimeter energy corrections is shown. The mean is 0.09 ± 0.32 GeV/c and $\sigma = 4.8$ GeV/c. The width of the distribution is a measure of the resolution for the P_T measurement (see Section 4.4.3).

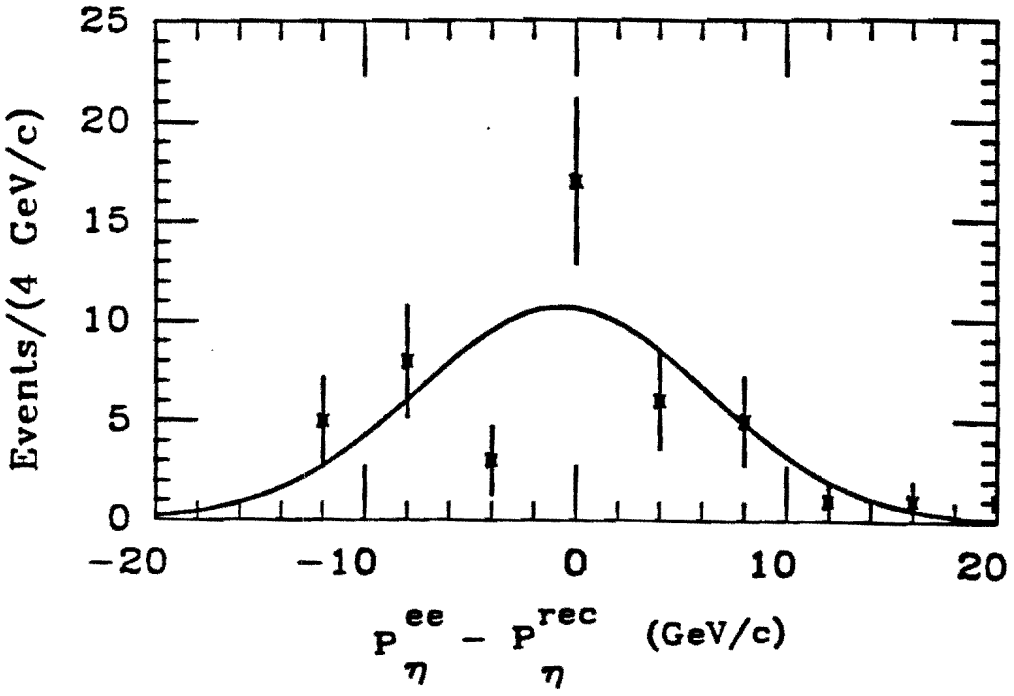

Figure 4.11: Same as Figure 4.10 except the sample contains only Z events with a cluster with $E_T > 10$ GeV. The mean of the fit is -0.45 ± 0.97 GeV/c and $\sigma = 6.6$ GeV/c.

After correction the mean is -0.45 ± 0.97 GeV/c with $\sigma = 6.6$ GeV/c. This number shifted by less than 0.25 GeV when the non-clustered correction factor was set to 1. Therefore, as in the case of the conversions, the correction to the clustered energy dominates the total energy corrections when a cluster(s) is present.

Since most Z events do not contain any jets with $E_T > 10$ GeV, the Z events mostly test the non-clustered energy correction factor, S_{nc}. The balancing of the electron-recoil measured values after the energy corrections have been applied indicates the S_{nc} factor is properly correcting the low energy deposits in the calorimeter. Although the statistics are limited, selecting Z events containing jets does provide another check of the cluster correction.

4.2.3 Checks with Inclusive Electrons

A sample of inclusive electrons events provide some qualitative tests of the energy corrections. The sample was selected using electron identification cuts similar to those made for

the W sample selection (see Section 3.1). The $\not\!\!E_T$ values parallel and perpendicular to the electron direction are shown in Figure 4.12. In both cases the observed and corrected values are shown. The peak at low $\not\!\!E_T$ is shifted from negative values to just above 0.0 GeV. Events with the electron from a b quark decay might cause the peak to be slightly positive since a neutrino is present. However, given the slight offset in the conversions, no conclusion can be made. The observed W transverse mass for the sample is shown in Figure 4.13. The peak from non-W events near 20 GeV is due to a calorimeter energy mismeasurement giving rise to a false $\not\!\!E_T$. Figure 4.13 shows that after corrections, the false peak was pushed back against 0.0 GeV which is the expected value for a transverse mass calculated with $\not\!\!E_T = 0$. Although these results are only qualitative, they do support the validity of the $\not\!\!E_T$ correction.

4.3 $\not\!\!E_T$ Correction Systematic Uncertainty

The systematic uncertainty on the $\not\!\!E_T$ correction comes from the uncertainty on the clustered energy correction and the uncertainty on the non-clustered energy correction factor, S_{nc}. For the P_T^W measurement no systematic uncertainty is introduced by the electron E_T corrections (see Section 4.1.2) since the electron E_T cancels out of the calculation. The systematic uncertainties for the clustered energy correction and S_{nc} are treated separately below.

4.3.1 Clustered Energy Correction

The systematic uncertainty on the clustered energy correction is divided into two parts. The first uncertainty is a function of the cluster E_T. This uncertainty is due to the low energy calorimeter response and the modeling of the calorimeter cracks. This represents an uncertainty in the coefficients of the E_T dependent terms of the quadratic correction (Eq. 4.4). The second part is an absolute systematic uncertainty in the clustered energy scale, a simple offset.

The conversions were used to investigate the uncertainty which scales with the E_T.

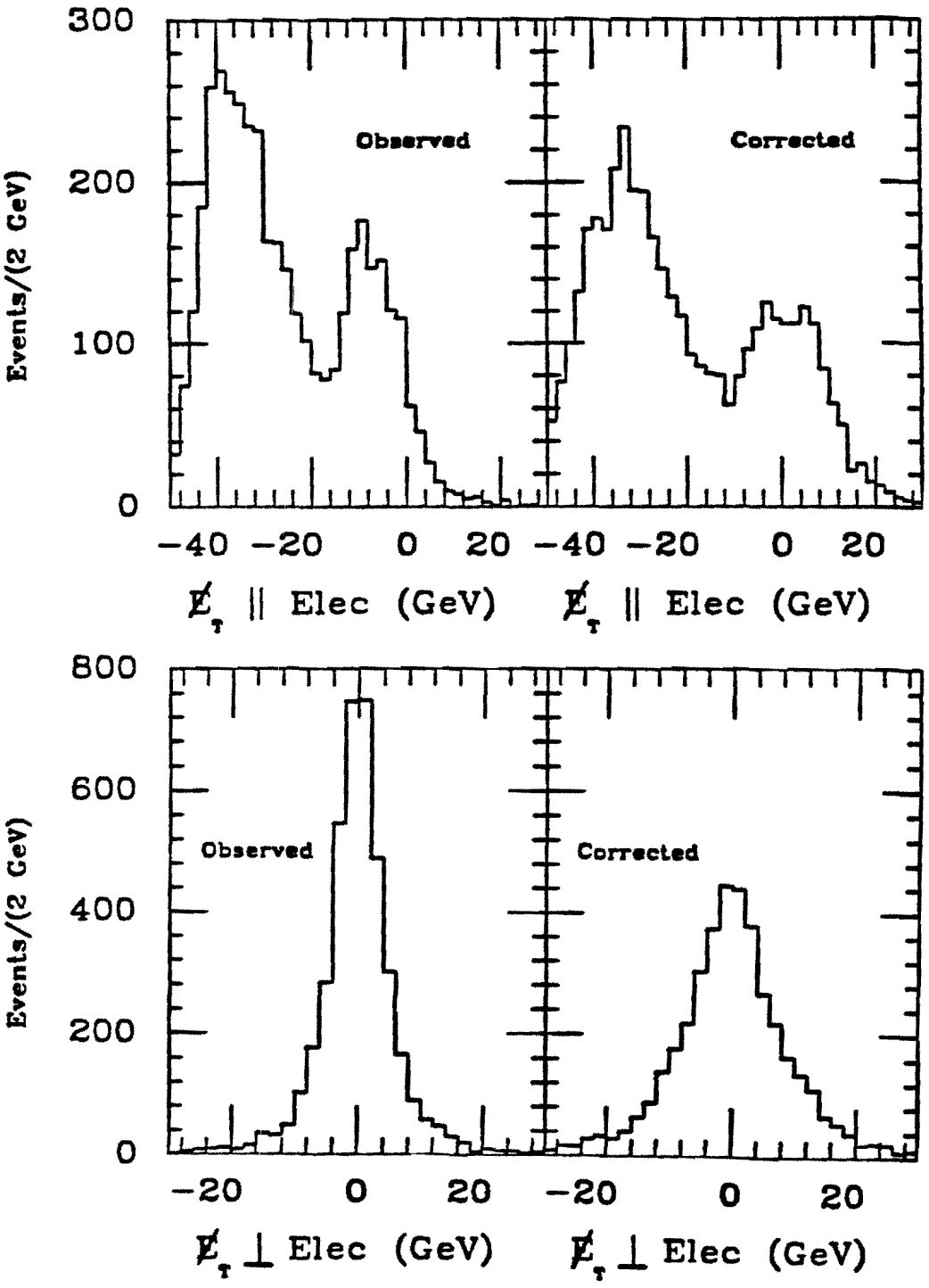

Figure 4.12: The distribution of the $\not\!\!E_T$ perpendicular ($\perp$) and parallel ($\|$) to the electron direction for the inclusive electron sample.

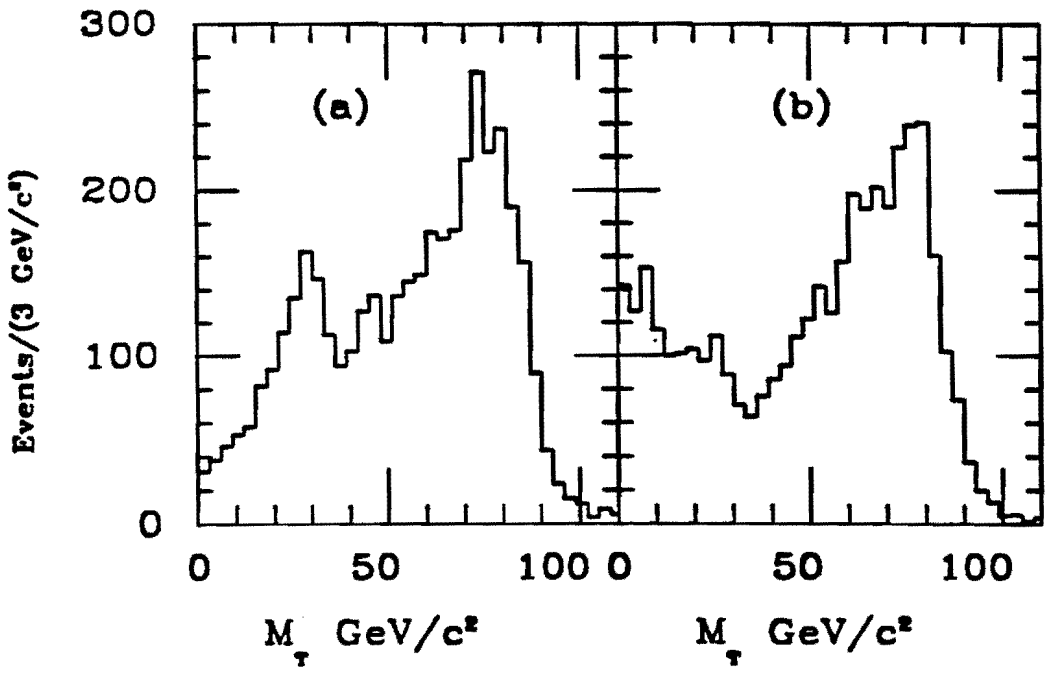

Figure 4.13: The transverse mass spectrum for the inclusive electron sample, (a) before any corrections. A false $\not\!\!E_T$ induced by the mismeasurement of clusters causes the low end to peak away from zero. Plot (b) shows the transverse mass after corrections are applied. The spectrum now is pushed back against zero.

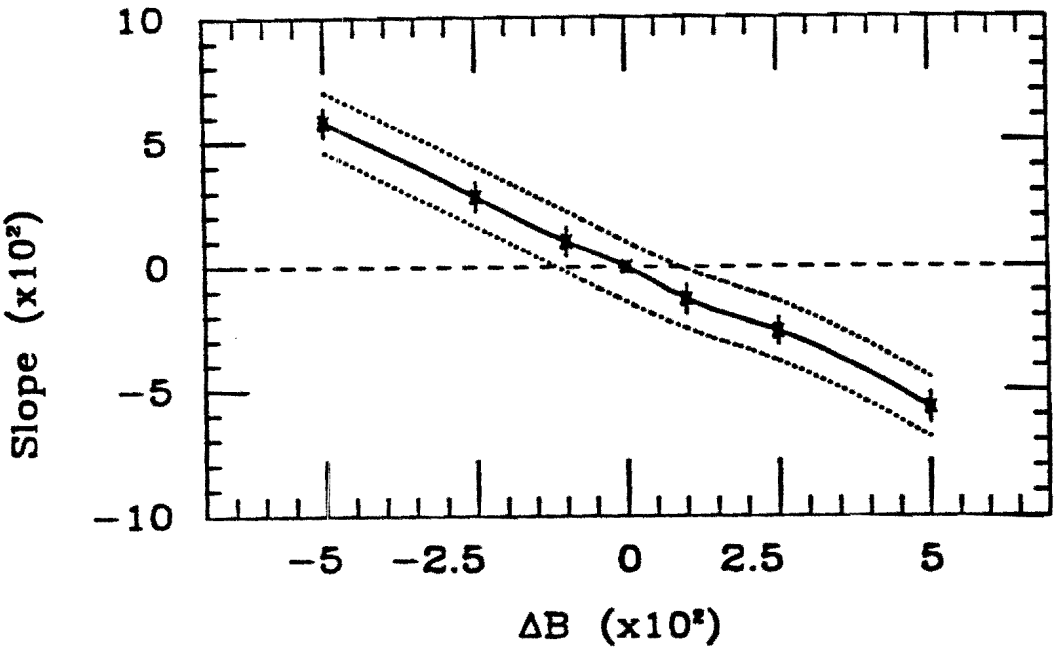

Figure 4.14: The slope variation of a fit to the conversion sample (Figure 4.4) as a function of the change of the linear coefficient of the clustered energy correction (Eq. 4.4.)

The uncertainty was measured as an uncertainty in the linear coefficient of the quadratic equation. The quadratic coefficient is small and the variation from this term is insignificant compared to the uncertainty of the linear coefficient. Figure 4.4 shows the $\not\!\!E_T$ parallel to the conversion electron direction. A fit of the corrected values to a straight line gives an offset of 1.01 GeV and a slope of $(0.6 \pm 2.2) \times 10^{-2}$. If the slope is constrained to 0.0, the offset fits to 1.2 ± 0.2 GeV. To determine the systematic uncertainty, the linear term in the cluster energy scale was varied and the corrected conversion spectrum was fit to a line with a constrained offset of 1.2 GeV. The slopes from the fits are shown in Figure 4.14 with dotted lines drawn for a 2σ shift. From Figure 4.14 the linear systematic uncertainty is taken as $\pm 0.015 * E_T$ for the lower E_T region of the clustered energy correction function. The limited statistics made a prediction for the high E_T region difficult. However, the sources of the systematic uncertainty are not expected behave differently than in the low E_T region. Therefore, a value $\pm 0.020 * E_T$ will be used.

A systematic offset of the clustered energy correction (an uncertainty in the constant

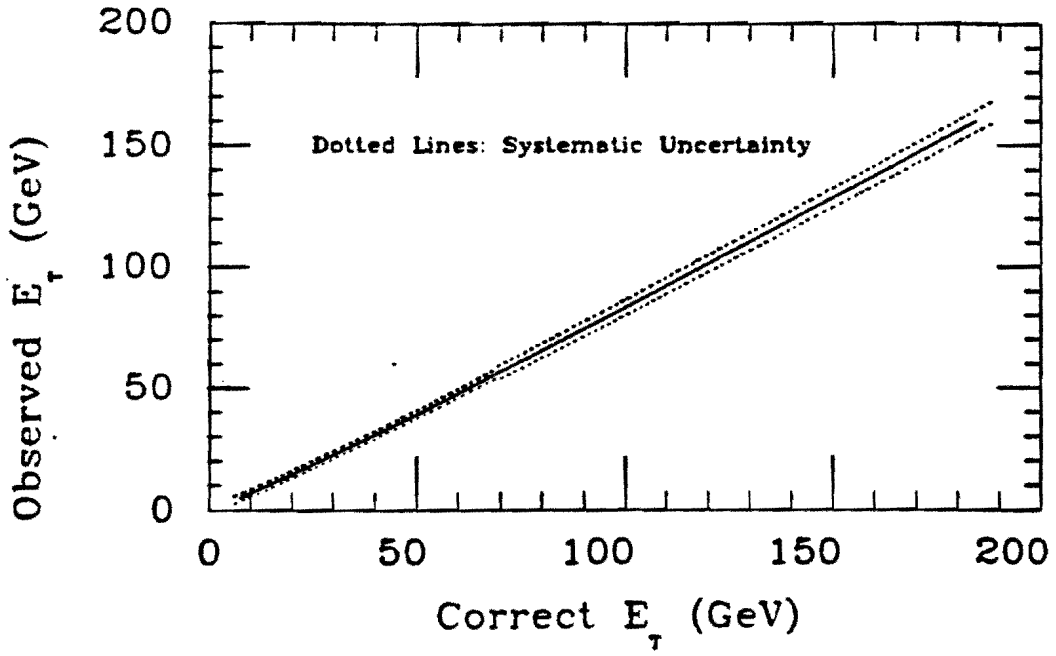

Figure 4.15: Observed Cluster E_T versus Correct E_T with systematic error bands.

term C, Eq 4.4) is more difficult to estimate. Figure 4.11 shows the $P_\eta^{ee} - P_\eta^{rec}$ for Z events with jets. The distribution's mean is -0.45 ± 0.97 GeV/c. Since clusters exist in the events, this quantity depends mostly on the clustered energy correction. The mean $\not\!\!E_T$ parallel to the conversion electrons is shifted high by approximately 1 GeV. Whether this shift is due to a real offset in the clustered energy scale or due to a subtlety in correcting the conversion events is not known. The systematic uncertainty on the clustered energy scale is taken to bracket the possible variations in the conversion and Z samples. The systematic uncertainty is ± 1.5 GeV in the low E_T ($< 57.$ GeV Obs.). For large E_T ($> 57.$ GeV Obs.), a value of ± 2.5 GeV is used. Figure 4.15 shows the clustered energy relation with the bands indicating the systematic uncertainty. The two uncertainties are added in quadrature. A cluster with an observed $E_T = 20$ GeV corrects to a 26.9 GeV cluster with a systematic uncertainty of ± 1.6 GeV. Similarly, a 50 GeV cluster corrects to 62.3 ± 1.8 GeV and 100 GeV corrects to 118.5 ± 3.6 GeV.

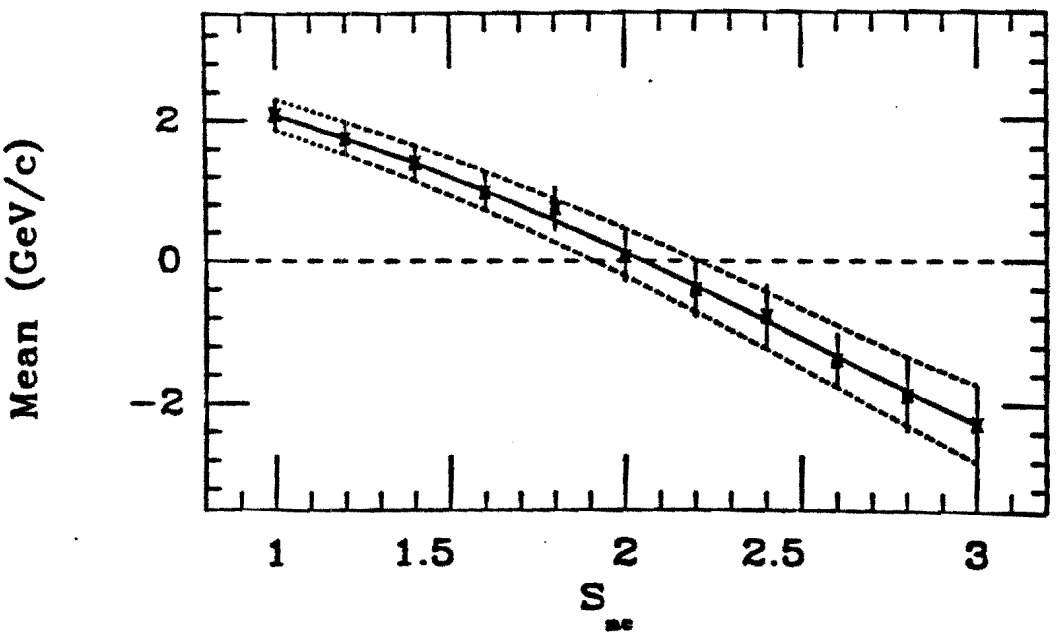

Figure 4.16: The mean $P_\eta^{ee} - P_\eta^{rec}$ for different values of S_{nc}. The sample of Z events used does not contain any clusters with $E_T > 10$ GeV so the entire $\not\!\!E_T$ correction comes from the S_{nc} scale factor. The dotted lines are the 1σ limits.

4.3.2 Non-clustered Energy Correction Factor, S_{nc}

To estimate the systematic uncertainty on the non-clustered energy correction factor, S_{nc}, the Z sample was used. Z events were selected from the sample by requiring no cluster with $E_T > 10$ GeV other than the electrons. The entire $\not\!\!E_T$ correction for these events comes from the non-clustered energy correction factor. For these events, the quantity $P_\eta^{ee} - P_\eta^{rec}$ was fit to a Gaussian distribution. Figure 4.16 shows the fitted mean plotted as a function of the scale factor, S_{nc}. The dotted lines are the 1σ limits for the errors on the mean. The 1σ limit on the high side gives an upper systematic limit of 2.2 for the scale factor. The lower systematic limit is taken as 1.8. This low limit is slightly larger than the 1σ limit. However, it maintains a symmetric uncertainty and allows for the variation seen in the Monte Carlo values in Table 4.2.

4.4 Resolution Smearing Correction

Since the P_T^W spectrum is a falling spectrum, resolution smearing generates a net movement of events to larger P_T^W and changes the spectrum shape. The resolution of P_T^W is dependent on the resolution for measuring the recoil energy. This depends on the energy corrections, especially S_{nc} which effectively changes the energy scale for low energy deposits. The smearing effects are corrected by a P_T^W dependent scale factor which reshapes the spectrum.

4.4.1 Method

The procedure used a parameterization to represent the P_T^W spectrum and a resolution function to describe the detector resolution. The parameterized spectrum was smeared using the resolution function. Each component of the P_T^W was smeared separately and the final smeared P_T^W was reconstructed from the components. This procedure gave a smeared P_T^W spectrum which was compared with the data and a χ^2 determined. The spectrum parameters were varied to find the parameters giving the minimum χ^2. Finally, using the optimum parameters, the ratio of the spectrum before smearing and the spectrum after smearing gives the resolution correction function,

$$R_{smear}(P_T) = \frac{(dN/dP_T)}{(dN/dP_T)_{smeared}} \tag{4.6}$$

The correction $R_{smear}(P_T)$ was applied to the observed spectrum to correct for resolution smearing effects.

4.4.2 Parameterization

Since theory does not provide a convenient function, a purely empirical parameterization was used. It does model the basic characteristics possessed by the P_T^W spectrum including the phase space roll-over at low P_T^W and the long tail (see Figure 1.4). The parameterization, with 5 free parameters, has the ability to fit a theoretical prediction well over the full P_T^W range. The parameterization used was

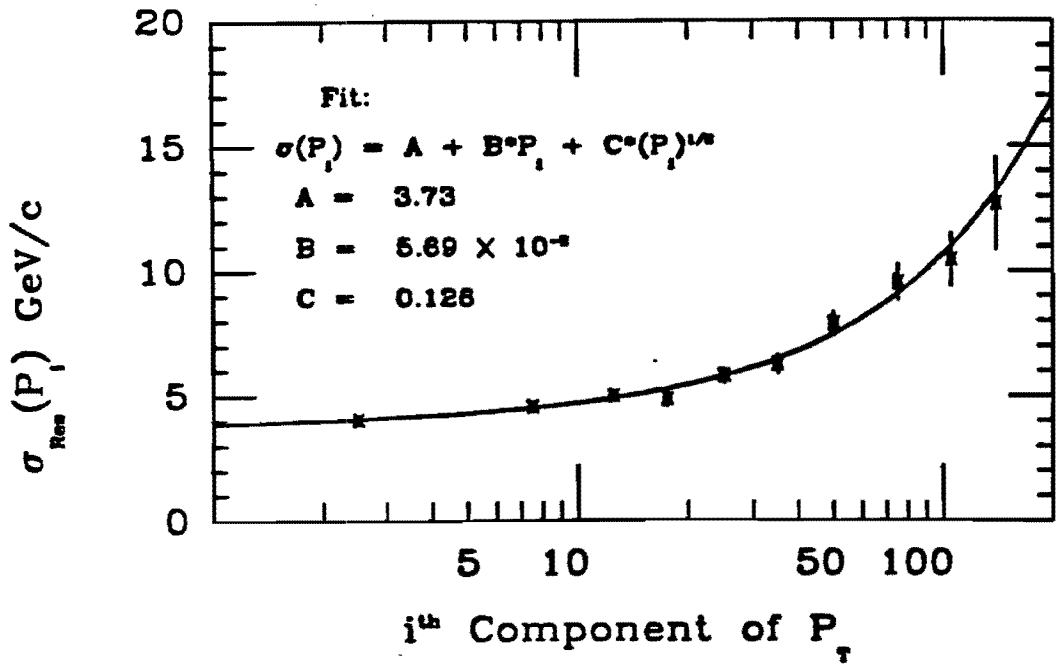

Figure 4.17: The resolution for a component, P_i, of the P_T^W versus the component magnitude. The resolution function is a fit to the points from the detector simulation.

$$\frac{dN}{dP_T} = \frac{2 * P_T * (P_T^2 - D)^{(C-1)}}{B * ((E * P_T)^F + 1)}. \tag{4.7}$$

4.4.3 Resolution Function

The resolution function is perhaps the most important piece of the smearing correction since it represents the resolution for which the spectrum is being corrected. The resolution was determined from a Monte Carlo program (PAPAGENO) with detector simulation. The simulated P_T^W was determined after all energy corrections were applied. The simulated P_T^W and the generated P_T^W were broken into detector components (x, y). For different ranges of P_i^{gen}, the difference, $P_i^{gen} - P_i^{sim}$, was fit to a Gaussian distribution. The width (σ) of each Gaussian distribution represents the resolution for the component P_i^{gen}. Figure 4.17 shows the resolution versus P_i^{gen}. The resolution was parameterized by fitting the values to a function. The function and the fit parameters are given in Figure 4.17.

Events generated with a given P_T^W contribute to all P_i less than the P_T^W. It is possible

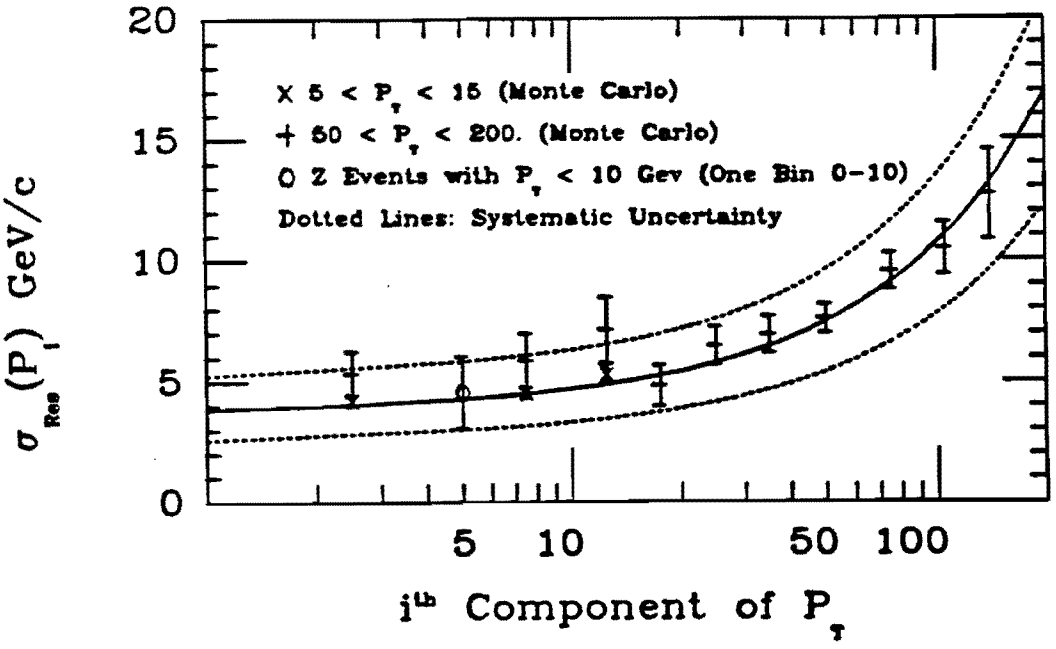

Figure 4.18: The resolution on the component for events in different P_T^W ranges. The resolution on small P_i components for high P_T^W events is slightly worse than low P_T^W events. Also shown is the resolution measured from Z events. It is in good agreement with the simulation.

that a small P_i component of high P_T^W events has poorer resolution than a P_i component of low P_T^W events. This was examined by determining the resolution for high and low P_T^W separately. Shown in Figure 4.18 are the parameterized fit and the values for events with P_T^W greater than 50 GeV/c. For the high P_T^W events, the resolution at small P_i is slightly worse than the resolution function fit. However, the difference is not large and attempting to use a more complex parameterization of the resolution would not necessarily enhance the result. Also shown in Figure 4.18 are the values for events with P_T^W generated between 5 and 15 GeV/c. Since the low P_T^W events form the bulk of the sharply falling spectrum, and therefore experience the largest effects from resolution smearing, it is most important to model the resolution of these events accurately.

Finally, Figure 4.18 has one point from Z events in the data. This point was determined with events having no jets with $E_T > 10$ GeV. The resolution was measured using P_η as measured by the electrons and the recoil energy (see Section 4.2.2 and Figure 4.10). The

Parameter	Value
B	6.02×10^{-4}
C	-0.200
D	-20.8
E	3.19×10^{-2}
F	2.89

Table 4.3: The fit parameters for the smeared spectrum.

Z events are summarized in a single bin extending from 0 to 10 GeV/c. The resolution from Z events agrees well with the resolution measured from the Monte Carlo. The systematic uncertainty for the resolution function is taken as the the dashed lines in Figure 4.18. The uncertainty is set such that it brackets the points from high P_T W's and the Z data.

4.4.4 Results of Fit

The parameters giving the best χ^2 ($\chi^2/n_f = 1.2$) is given in Table 4.3. Using the fit results, a smearing correction function was determined with Equation 4.6. The correction function is shown in Figure 4.19. Most of the smearing occurs at low P_T^W where the spectrum is falling fastest. In the large P_T^W region, the effect becomes less important. To determine the correction function's systematic uncertainty, the resolution function was varied to its upper and lower limits. For each case, the χ^2 minimization was repeated to determine another function R_{smear}^{sys}. The two dotted curves in Figure 4.19 are the two correction functions determined. The dotted curve which starts at ~ 1.3 represents the correction if the resolution was better. The other dotted curve represents the correction if the resolution was worse. The next chapter describes how the systematic uncertainties propagate into the measurement of $d\sigma/dP_T$.

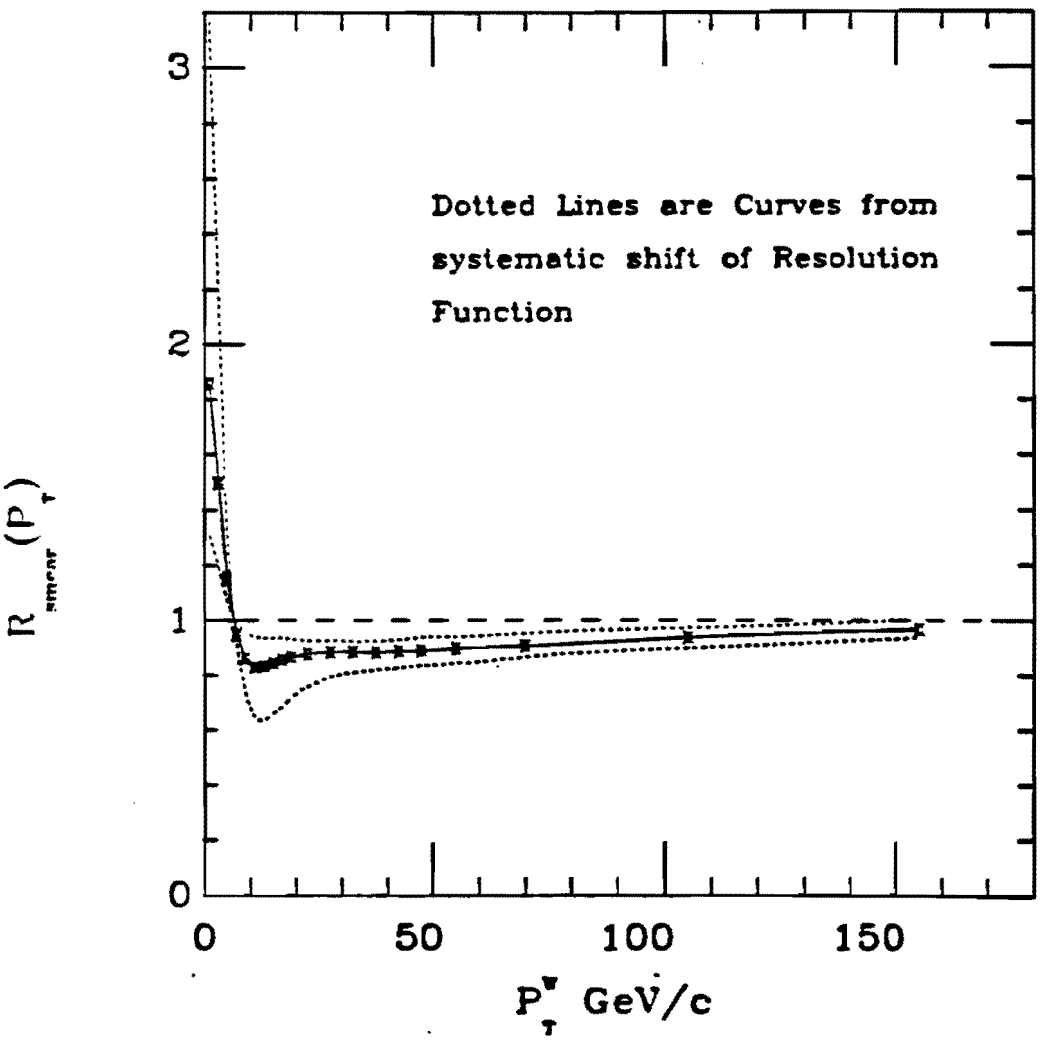

Figure 4.19: The multiplicative correction function for resolution smearing. The points with the solid curve represent the correction for each P_T^W. The dashed lines are the corrections derived when the resolution function is varied by its systematic uncertainty. The correction is largest at low P_T^W where the distortion of the spectrum is greatest. At large P_T^W, resolution effects are less important because the spectrum is not falling as rapidly.

Chapter 5

Systematic Uncertainty

The determination of the differential cross section requires several corrections. The correction factors for one P_T^W are not independent of the correction factors for another P_T^W. Therefore, the different cross section measurements are also *not* independent of one another. Because of the bin-to-bin correlations, the propagation of the systematic uncertainties for the P_T^W spectrum must be handled with care. In order to determine the correlations, a covariance matrix was found using the method described below. An element of the covariance matrix is defined by,

$$C_{ij} = \frac{1}{M}\sum_{n=1}^{M}(Y_i^n - \bar{Y}_i) * (Y_j^n - \bar{Y}_j) \tag{5.1}$$

where,

- M is the total number of simulated samples generated (M = 10^6).
- $\bar{Y}_i$ is the average value for the i^{th} bin. It is taken as the nominal fully corrected cross section for the i^{th} bin.
- Y_i^n is the value for the i^{th} bin for the n^{th} sample. It is taken as the cross section with some statistical or systematic fluctuation.

The cross section measured in the i^{th} bin is determined with the following relation,

$$Y_i = S * \frac{R_i}{A_i} * (X_i - N_i^{QCD} - N_i^Z - N_i^{top}) \tag{5.2}$$

where,

- Y_i is the fully corrected cross section, $d\sigma/dP_T$, for the i^{th} bin.
- S is a normalization factor independent of bin number.
- R_i is the smearing correction factor for the i^{th} bin.
- A_i is the acceptance in the i^{th} bin.
- X_i is the number of events per GeV/c in the i^{th} bin (after $\not\!\!E_T$ correction).
- N_i^{QCD} is the number of events per GeV/c of QCD background events in the i^{th} bin. Where,

$$N_i^{QCD} = N_{tot}^{QCD} * (1/N\ dN/dP_T)_i^{QCD} \tag{5.3}$$

- N_i^Z is the number of events per GeV/c of Z background events in the i^{th} bin.
- N_i^{top} is the number of events GeV/c of top background events in the i^{th} bin.

The value of the normalization factor, S, is determined with the following relation:

$$S = \frac{(1 - \tau_{bg})}{\mathcal{L} * \epsilon_{ele} * (1 - C) * (1 - Z) * V * B} \tag{5.4}$$

where

- $\mathcal{L}$ is the integrated luminosity.
- τ_{bg} is the percentage of events from the background $W \rightarrow \tau\nu$.

$$\tau_{bg} = \tau_{bg}^{Norm} * \mathcal{L}/N_{tot} \tag{5.5}$$

  Where τ_{bg}^{Norm} is the cross section for $W \rightarrow \tau\nu$ events *in the* $W \rightarrow e\nu$ sample. N_{tot} is the total number of events in the sample after the other backgrounds are subtracted.

- ϵ_{ele} is the efficiency of the electron identification cuts.
- C is the fraction of *real* W events lost by the cuts used to eliminate conversion events.

Factor		Value
Electron Identification Cut Efficiency	ϵ	0.84 ± 0.03
Background: $W \rightarrow \tau\nu$	τ_{bg}	0.034 ± 0.004
Over efficiency of Conversion Identification	C	0.035 ± 0.015
Over efficiency of Z Veto	Z	0.001 ± 0.01
Vertex Cut at 2σ	V	0.954 ± 0.005
Integrated Luminosity	$\mathcal{L}$	$4.05 \pm 0.28\ pb^{-1}$
Assumed Branching Ratio	B	1/9

Table 5.1: Summary of the normalization factors.

- Z is the fraction of *real* W events lost by the cuts used to eliminate Z events.
- V is the efficiency for the Z vertex cut.
- B is the branching ratio of $W \rightarrow e\nu$.

In the Equation 5.2, the X_i's represent the number of events divided by the bin width for the i^{th} bin. Since the $\not\!\!E_T$ correction is an event-by-event correction, the X_i's represent the number *after* the $\not\!\!E_T$ correction is applied. The quantities which enter the scale factor, S, are summarized in Table 5.1. The backgrounds are summarized in Table 3.1 and Table 5.2. Finally, the acceptance and resolution smearing correction factors are also summarized in Table 5.2.

5.1 Method

5.2 Statistical Uncertainty Only

The general procedure is most clearly understood by examining the simple case of the statistical uncertainty. First, $\bar{Y}_i$ was determined using the observed X_i and the nominal correction factors. For the n^{th} simulated sample, X_i was determined from a Poisson distribution with a characteristic parameter equal to the observed number of events in the bin. For bins with more than 30 events, a Gaussian distribution was used as an approximation

Bin Range (GeV/c)	Background (Events/GeV/c)	Resolution Correction	Acceptance
0 - 2	1.2 ± 0.91	$1.86 \pm^{1.31}_{0.54}$	0.33 ± 0.02
2 - 4	2.5 ± 1.5	$1.50 \pm^{0.66}_{0.30}$	0.33 ± 0.02
4 - 6	3.4 ± 1.9	$1.15 \pm^{0.26}_{0.15}$	0.32 ± 0.02
6 - 8	3.5 ± 2.0	$0.95 \mp^{0.20}_{0.05}$	0.32 ± 0.02
8 - 10	3.5 ± 1.9	$0.86 \mp^{0.16}_{0.12}$	0.32 ± 0.02
10 - 12	3.5 ± 1.8	$0.83 \mp^{0.18}_{0.11}$	0.32 ± 0.02
12 - 14	3.6 ± 1.8	$0.83 \mp^{0.20}_{0.11}$	0.315 ± 0.02
14 - 16	3.5 ± 1.8	$0.84 \mp^{0.18}_{0.09}$	0.315 ± 0.02
16 - 18	3.0 ± 1.7	$0.86 \mp^{0.17}_{0.08}$	0.31 ± 0.02
18 - 20	2.7 ± 1.6	$0.87 \mp^{0.15}_{0.07}$	0.31 ± 0.02
20 - 25	1.7 ± 1.0	$0.88 \mp^{0.12}_{0.05}$	0.31 ± 0.02
25 - 30	1.2 ± 0.84	$0.89 \mp^{0.09}_{0.04}$	0.31 ± 0.02
30 - 35	0.71 ± 0.68	$0.89 \mp^{0.08}_{0.04}$	0.31 ± 0.02
35 - 40	$0.43 \pm^{0.58}_{0.43}$	$0.88 \mp^{0.07}_{0.04}$	0.31 ± 0.02
40 - 45	$0.23 \pm^{0.53}_{0.23}$	$0.89 \mp^{0.06}_{0.04}$	0.315 ± 0.02
45 - 50	$0.20 \pm^{0.50}_{0.20}$	$0.89 \mp^{0.06}_{0.04}$	0.32 ± 0.02
50 - 60	$0.14 \pm^{0.38}_{0.14}$	$0.90 \mp^{0.06}_{0.04}$	0.325 ± 0.02
60 - 80	$0.062 \pm^{0.23}_{0.062}$	$0.91 \mp^{0.04}_{0.04}$	0.34 ± 0.02
80 - 130	$0.019 \pm^{0.079}_{0.019}$	$0.94 \mp^{0.04}_{0.03}$	0.40 ± 0.03
130 - 180	$0.0031 \pm^{0.022}_{0.0031}$	$0.97 \mp^{0.03}_{0.03}$	0.465 ± 0.05

Table 5.2: Summary the correction factors for each bin. The background numbers are the sum of all the backgrounds (see Chapter 3).

to the Poisson distribution. The Y_i^n was determined using the random X_i and the nominal correction values in Equation 5.2. A large number of samples were generated each with a set of Y_i^n. The covariance matrix was determined with Equation 5.1. Finally, the statistical uncertainty was taken as the square root of the diagonal element of the covariance matrix,

$$\delta Y_i^{Stat} = \sqrt{C_{ii}}. \tag{5.6}$$

As expected, this gives $\sqrt{N}$ uncertainties for bins containing a large number of events. The statistical uncertainty of the integrated spectrum is also $\sqrt{N_{tot}}$. Table 6.1 gives the cross section value for each bin, $\bar{Y}_i$, and the statistical uncertainty.

5.3 Statistical and Systematic Uncertainty

The covariance matrix for the combined statistical and systematic uncertainties was calculated in a similar manner. However, instead of using the nominal correction factors (ϵ, $\mathcal{L}$, τ_{bg}, R_i, etc.), these factors were allowed to vary. The systematic uncertainty for each piece can be found in Chapters 3 and 4. For the factors which contribute only to the scale factor S (Eq. 5.4), a random value was generated using a Gaussian distribution with a mean equal to the nominal value and a width equal to the systematic uncertainty of the correction. Varying the correction factors which have a bin dependence (A_i, R_i, and N_i) is more complicated. It is important to vary these factors such that the bin-to-bin correlations are maintained.

5.3.1 Backgrounds

The backgrounds were allowed to vary in two parts. First, the total number of background events was varied according to a Gaussian distribution. This represents the *systematic* variation of the total number of background events. The background shape, $(1/N\ dN/dP_T)$, was scaled by the total number of events to find the number in each bin. Second, the number of events in each bin is varied with a Poisson distribution (Gaussian for $n > 30$). This allows bins with a fraction of an event to fluctuate up to 1 or more events. This represents

a *statistical* fluctuation of the number of events in a given bin. The resulting number of background events in each bin (N_i^{Bg}) was then used for the background subtraction. This procedure was performed separately for each type of background.

5.3.2 Acceptance

The fluctuated acceptance was determined by changing the value in each bin by the same sigma. The fractional sigma, Δ, was determined from a Gaussian with a mean of zero and width of 1. The acceptance with a systematic fluctuation in the i^{th} bin is,

$$A_i^{sys} = A_i^{nom} + \Delta * \delta A_i \tag{5.7}$$

Note, the Δ was the same for all bins, but δA_i may be different for each bin (see Table 5.2). This method assumes 100% correlation between the bins.

5.3.3 Resolution Smearing Correction

The systematic variation of the resolution smearing correction is caused by the resolution function uncertainty. Making the resolution one sigma worse gives a smearing correction for low resolution, $R_i^{sys,\,L}$ (see Section 4.4.3 and Figure 4.19). Conversely, making the resolution one sigma better gives a smearing correction for higher resolution, $R_i^{sys,\,H}$. The resolution fluctuation was determined in the same manner as the acceptance. A random Gaussian distributed Δ was generated as the fractional fluctuation. If Δ was positive, the $R_i^{sys,\,L}$ was used and conversely for a negative Δ, the $R_i^{sys,\,H}$ was used. The smearing correction, with a systematic fluctuation due to the resolution function, is

$$R_i^{sys} = R_i^{nom} + |\Delta| * (R_i^{sys,\,H\ or\ L} - R_i^{nom}) \tag{5.8}$$

Each Δ generates a different curve for the resolution smearing correction. Figure 5.1 shows a set of curves for different positive Δ. Notice for some P_T^W's the R_i^{sys} is greater than R_i^{nom} but for other P_T^W's it is less. This maintains the correlations between bins and approximately preserves the property that the smearing correction changes only the shape and not the area of the distribution. However, this method has the disadvantage of giving

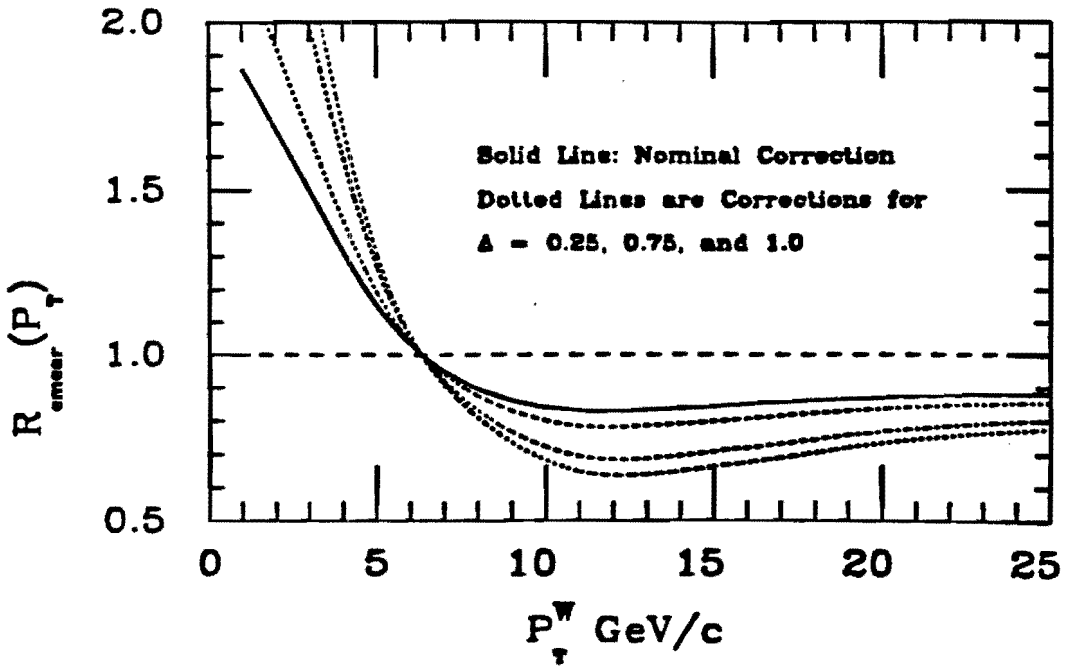

Figure 5.1: Different smearing corrections for different systematic fluctuations of the resolution function.

the corrections near the cross point a nonphysically small systematic variation (see Figure 5.2). The problem is corrected by inflating the systematic uncertainty of the corrections near the cross point to be similar in magnitude to the adjacent points. Figure 5.2 shows the inflated systematics as +'s.

After the nominal resolution smearing correction was applied, the spectrum area changed by approximately 0.6%. When systematic fluctuations were made, the area changed on average by 1.2%. Naively, renormalizing the spectrum seems appropriate. However, in the case of the systematically fluctuated spectrum, this has the undesirable effect of moving the systematic uncertainty from one bin to another. Therefore, the spectrum was not renormalized after smearing corrections. The disadvantage of not renormalizing is the small variations of the total number of events cause the errors to be slightly larger than if the correction factors perfectly conserved area.

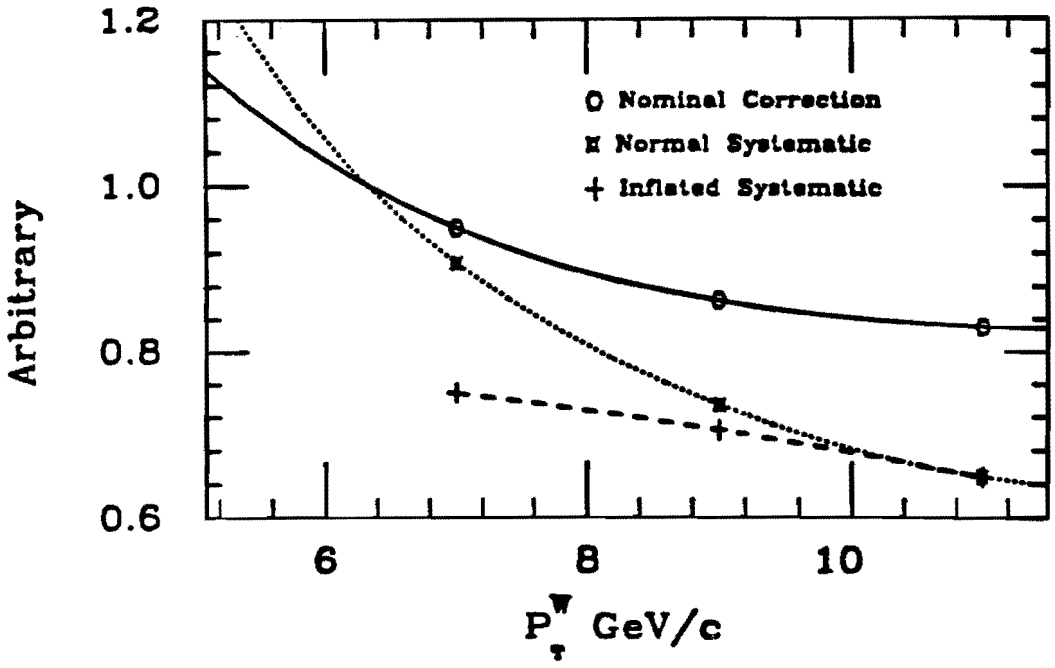

Figure 5.2: The systematic uncertainty near a cross point. The well defined cross point is nonphysical. The systematic uncertainty near the cross point must be smeared. Therefore, the systematic uncertainty near a cross point is inflated to be similar to the systematic uncertainty for points further from the cross point.

5.3.4 $\not\!\!E_T$ Corrections

The final systematic variation involves the $\not\!\!E_T$ correction. Since the correction was performed on an event-by-event basis, it was already included in the generated X_i's. Variations in the $\not\!\!E_T$ correction cause the spectrum to change shape but the total number of events does not change. The systematic variation was incorporated by changing the spectrum shape before any of the remaining corrections were applied. The change was performed by a scale factor similar to the resolution smearing correction. However, in this case a scale factor of 1.0 is the nominal correction (*i.e.* no shape change).

A scale factor for the i^{th} bin, M_i^{sys}, was determined from three pieces, M_i^{nc}, $M_i^{Clus,\,1}$, and $M_i^{Clus,\,2}$. The M_i^{nc} is the change due to the uncertainty of the non-clustered energy correction factor (see Section 4.1.4). The factors $M_i^{Clus,\,1}$ and $M_i^{Clus,\,2}$ are the changes due to the uncertainty of the clustered energy corrections, the offset term and the linear term respectively (see Section 4.1.3). The M_i's were determined from a Monte Carlo program by taking the ratio of two P_T^W spectrums (Eq. 5.9). One spectrum was determined using the nominal correction and the second spectrum used a $\not\!\!E_T$ correction with the corresponding factor varied to one systematic sigma. A high fluctuation of the non-clustered energy correction factor (S_{nc}) produced a different spectrum change than a low fluctuation. So, a separate M_i was determined for for high and low fluctuations. Therefore,

$$M_i^{nc,\,H} = \frac{(dN/dP_T)_i^{S_{nc}=2.2}}{(dN/dP_T)_i^{S_{nc}=2.0}} \tag{5.9}$$

The values of $M_i^{nc,\,H}$ and $M_i^{nc,\,L}$ are shown in Figure 5.3. The values of $M_i^{Clus,\,1}$ and $M_i^{Clus,\,2}$ were determined in the same manner. For the cluster M_i's, the high and low fluctuation of the $\not\!\!E_T$ correction parameter produce a symmetric change in the shape. Figures 5.4 and 5.5 show $M_i^{Clus,\,1}$ and $M_i^{Clus,\,2}$, respectively. In these figures, only one limit of the systematic variation is shown. The opposite limit of the systematic variation is simply a mirror reflection about 1.0. Each of the M_i's is plagued by the same problem as the smearing correction variation. The systematic uncertainty near a cross point is nonphysically small. Again, the problem is solved by inflating the systematics near the

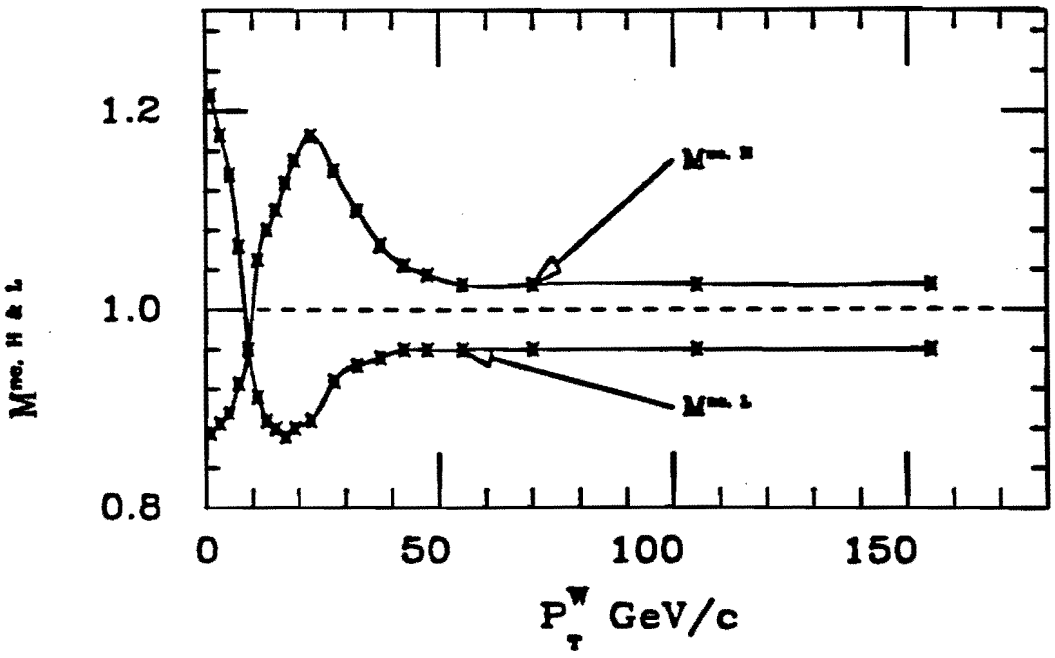

Figure 5.3: Scale factor from systematic uncertainty of non-clustered correction factor

cross point to be similar in magnitude to the adjacent points (see Figure 5.2).

The three M_i's must be combined into a total M_i^{sys}. The following relation was used to find M_i^{sys}.

$$M_i^{sys} = \prod_j (|\Delta_j| * (M_i^{j,\ H\ or\ L} - 1.0) + 1.0) \qquad j = 1,2,3 \tag{5.10}$$

where,

- j represents one of the three systematic uncertainties: the non-clustered energy scale factor, the offset for the clustered energy correction, or the linear factor of the clustered energy correction.
- Δ_j is the fractional sigma shift for the j^{th} correction. It is determined from a Gaussian centered on 0 and unit width.
- $M_i^{j,\ H\ or\ L}$ is the j^{th} M_i, the high or low fluctuation is taken depending on the sign of Δ_j as in the case of the smearing correction variation.

This method of combining the M_i's has the effect of adding the contributions in quadrature.

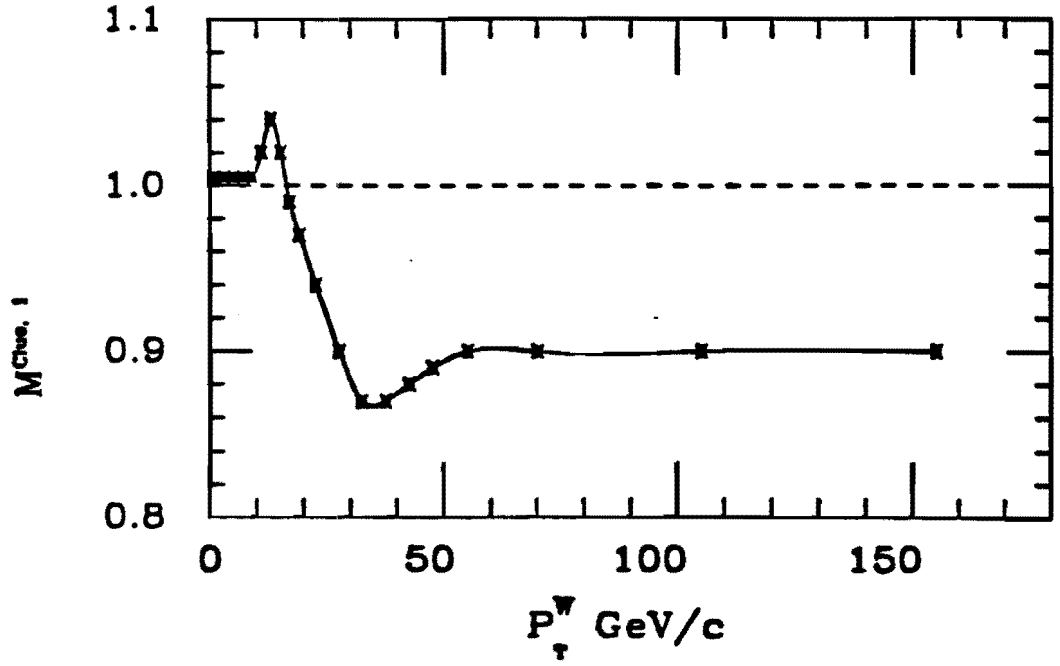

Figure 5.4: Scale factor from the systematic uncertainty of the clustered energy correction offset parameter (C) (see Eq. 4.4).

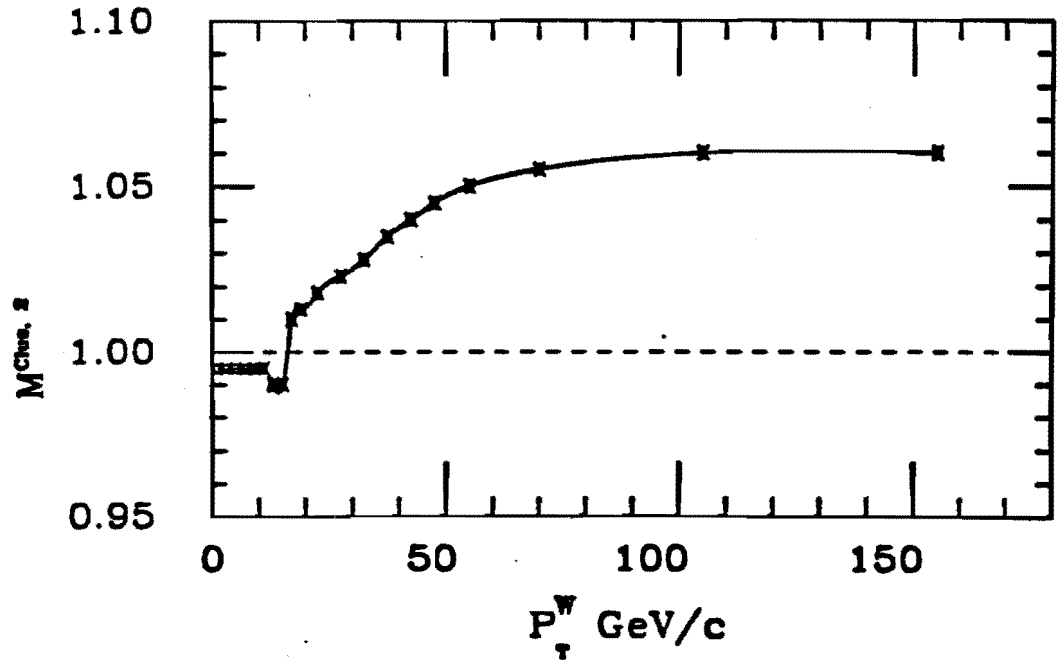

Figure 5.5: Scale factor from the systematic uncertainty of the clustered energy correction linear parameter (B) (see Eq. 4.4).

Finally, the M_i^{sys} was applied to the spectrum to change its shape.

$$X_i' = M_i^{sys} * X_i \tag{5.11}$$

The X_i''s represent a spectrum with a systematic fluctuation of the energy corrections. Like the smearing correction, the M_i's preserve the number of events only approximately. In this case, the change was usually less than 1%. The X_i''s were used to determine the Y_i's using the relation at the begin of this chapter.

5.4 Results

As with the statistical uncertainty, the covariance matrix elements, C_{ij}, were determined and the uncertainty for the i^{th} bin was taken as $\sqrt{C_{ii}}$. The cross section results are summarized in Chapter 6 (Table 6.1). The total systematic uncertainty on the cross section from the normalization factor, S, is $\sim$ 9%. The magnitudes of the other systematic uncertainties vary with P_T^W. The contribution from the acceptance is roughly constant at 6% except in the last two bins where it grows to $\sim$ 10%. The systematic uncertainties from the backgrounds range from 2% at small P_T^W to $\sim$ 25% at large P_T^W. The systematic uncertainty from the resolution smearing correction is very large for the first bin ($\sim$ 50%) but drops rapidly to between 10% and 20% for $5.0 < P_T^W < 25$ GeV/c and is less than 6% for $P_T^W > 40$ GeV/c. The systematic uncertainty from the energy corrections is between 15% and 30% for $P_T^W < 40$ GeV/c and $\sim$ 13% for $P_T^W > 40$ GeV/c. The complete covariance matrix and the correlation coefficients are given in Appendix D. At small P_T^W, the bins are highly correlated with the adjacent bins, $\rho_{i,i+1} \sim 0.9$. In the large P_T^W range the bins are less correlated. The covariance matrix is used to determine the uncertainty on the integrated cross section above a given P_T^{min} and the χ^2 comparisons given in the next chapter.

Chapter 6

Summary of the Results

Chapter 3 described the efficiencies, acceptance, and backgrounds for the collected sample of W bosons. The corrections which were applied to each event ($\not\!\!E_T$ correction) and to the spectrum as a whole (resolution smearing correction) were described in Chapter 4. These two chapters give the necessary information for determining the differential cross section, $d\sigma/dP_T$. Chapter 5 gives the relation used to calculate the differential cross section values. Chapter 5 also explains how the systematic uncertainties were propagated into the measurement of the P_T spectrum. This chapter summarizes the results found from the application of the corrections to the raw spectrum and the propagation of the systematic uncertainties.

6.1 The Differential Cross Section, $d\sigma/dP_T$

The differential cross section was determined using Equation 5.2. and the values for each bin are summarized in Table 6.1. The raw value is the (number of events)/GeV/c before any corrections. The energy corrected value is the (number of events)/GeV/c after the $\not\!\!E_T$ correction was applied to each event. Finally, the fully corrected cross section (pb/GeV/c) is given for each bin. The full P_T spectrum[1] is shown complete with systematic error bars in Figure 6.1. The outside error bar represents the combined systematic and statistical

[1] Appendix C describes how the positions for the highest P_T bins are determined.

uncertainty while the inside error bar is only the statistical uncertainty. The solid lines are a next-to-leading order QCD calculation [19, 20]. The lines represent the theoretical limits on the calculation. The calculation used HMRS B structure functions [21] and $\Lambda_{QCD} = 190$ MeV. There is good agreement between the theoretical prediction and the measured cross section. The agreement in the large P_T^W region is especially good. In this region, the experimental and theoretical systematic uncertainties are the smallest. The low end of the spectrum is shown in Figure 6.2 with the same theoretical prediction. At the low end, some deviation is seen in the range 10 to 25 GeV/c. However, these bins are highly correlated (see Appendix D) and the bins would tend to fluctuate up together. When a χ^2 comparison with the full covariance matrix was performed in the region 5 to 30 GeV/c, the χ^2/n_f was found to be 0.7. Treating the errors as independent (using only the diagonal elements of the covariance matrix) gave $\chi^2/n_f = 9.5$. A χ^2 comparison with the covariance matrix over the full P_T^W range gave a $\chi^2/n_f = 2.4$. Most of the discrepancy comes from the first bin where both the theoretical and experimental uncertainties are largest. When the first bin was not included in the χ^2 comparison, the χ^2/n_f is 0.75.

6.2 Integrated Cross Section

Once the differential cross section was determined, it was straight forward to integrate the distribution either over the full P_T^W range, to give the total cross section, or over a limited range, to give the cross section above a P_T^W cutoff. The integration used the covariance matrix to propagate the uncertainties. The total measured cross section for W boson production is:

$$\sigma_W = 21.0 \pm 0.5\ (stat) \pm 2.6\ (sys)\ \text{nb}$$

where the assumed branching fraction for $W \rightarrow e\nu$ is 1/9. The theoretical prediction for this value is 18.6 $\pm$ 2.8 nb. Including, the branching ratio for W $\rightarrow$ $e\nu$ gives $\sigma \cdot B = 2.33 \pm 0.05\ (stat) \pm 0.29\ (sys)$ nb. This is in good agreement with another analysis of the CDF production data which measured the total cross section as $\sigma \cdot B = 2.19 \pm 0.04\ (stat) \pm 0.21\ (sys)$ nb [57]. The systematic uncertainty from the integrated differential cross section

P_T Range (GeV/c)	P_T (GeV/c)	Raw (events/GeV/c)	Energy Corrected (events/GeV/c)	$d\sigma/dP_T$ (pb/GeV/c) (±stat±sys & stat)
0 - 2	1.0	171.5 ± 9.3	45.5 ± 4.7	694 ± 75 ± 460
2 - 4	3.0	273.5 ± 11.7	125.0 ± 7.9	1562 ± 102 ± 680
4 - 6	5.0	248.5 ± 11.1	147.0 ± 8.6	1419 ± 84 ± 390
6 - 8	7.0	145.0 ± 8.5	135.5 ± 8.2	1084 ± 68 ± 230
8 - 10	9.0	99.0 ± 7.0	132.0 ± 8.1	963 ± 61 ± 205
0 - 12	11.0	73.5 ± 6.1	108.5 ± 7.4	762 ± 54 ± 180
12 - 14	13.0	44.0 ± 4.7	97.0 ± 6.9	684 ± 51 ± 175
14 - 16	15.0	39.0 ± 4.4	73.5 ± 6.1	521 ± 45 ± 130
16 - 18	17.0	19.5 ± 3.1	62.5 ± 5.6	451 ± 43 ± 115
18 - 20	19.0	21.5 ± 3.3	53.0 ± 5.1	388 ± 40 ± 97
20 - 25	22.5	17.2 ± 1.9	38.8 ± 2.8	291 ± 22 ± 69
25 - 30	27.5	7.6 ± 1.3	20.6 ± 2.0	154 ± 16 ± 37
30 - 35	32.5	4.8 ± 1.0	15.2 ± 1.7	115 ± 14 ± 28
35 - 40	37.5	4.8 ± 1.0	8.20 ± 1.3	61.1 ± 9.9 ± 16.5
40 - 45	42.5	3.4 ± 0.8	6.80 ± 1.2	51.5 ± 9.2 ± 14
45 - 50	47.5	2.4 ± 0.7	5.40 ± 1.0	40.5 ± 8.1 ± 12
50 - 60	54.7	0.9 ± 0.3	2.7 ± 0.5	19.6 ± 4.0 ± 5.9
60 - 80	68.9	0.45 ± 0.15	1.05 ± 0.23	7.3 ± 1.7 ± 2.7
80 - 130	99.6	0.12 ± 0.05	0.200 ± 0.06	1.18 ± 0.41 ± 0.69
130- 180	151.2	0.02 ± 0.02	0.080 ± 0.04	0.44 ± 0.24 ± 0.28

Table 6.1: Cross section values for each P_T^W.

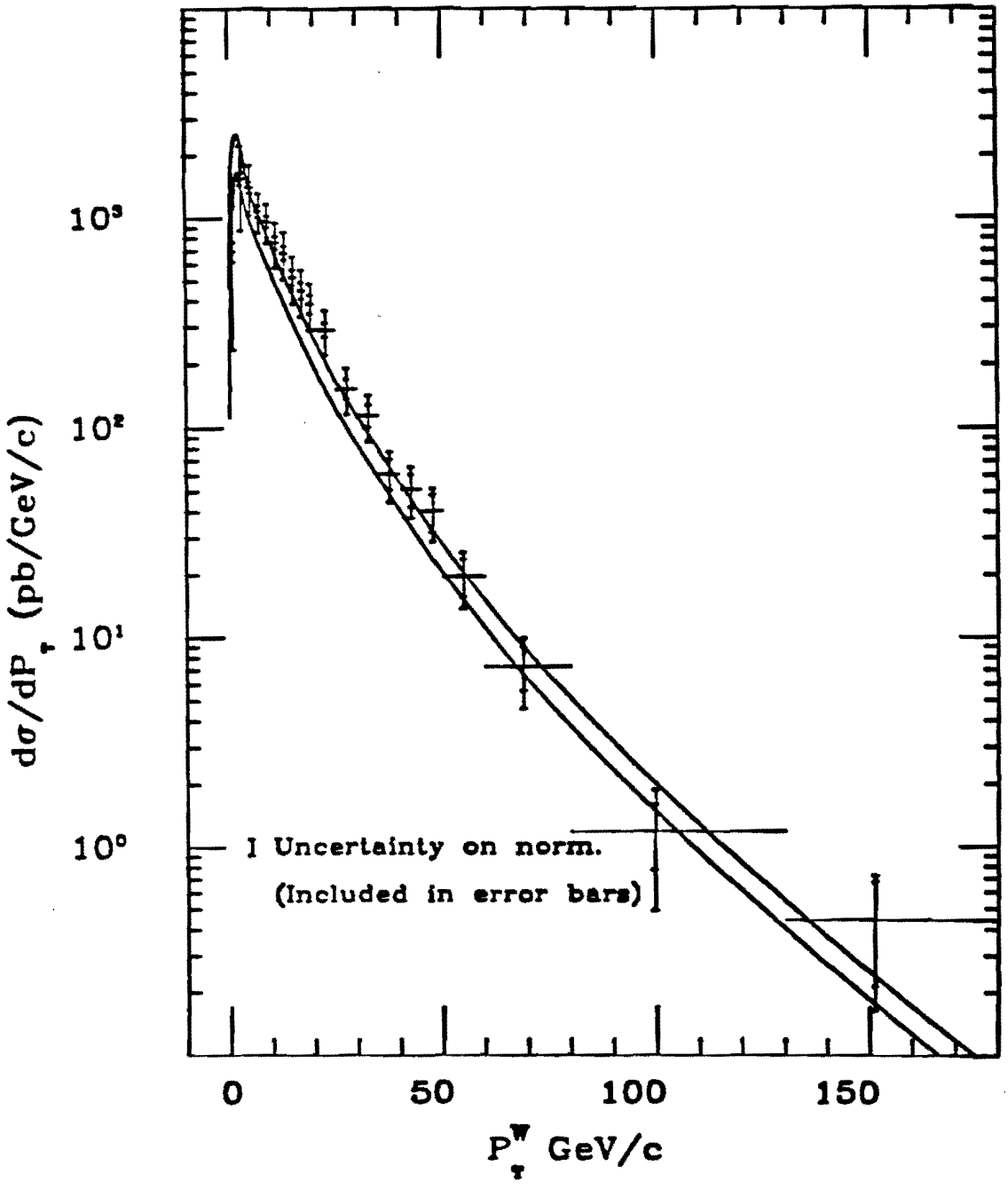

Figure 6.1: The differential cross section, $d\sigma/dP_T$. The data points are fully corrected. The solid band is a next-to-leading order prediction [20] with HMRS(B) structure functions and $\Lambda_{QCD} = 190$ MeV. The width of the band represents the theoretical uncertainty of the prediction.

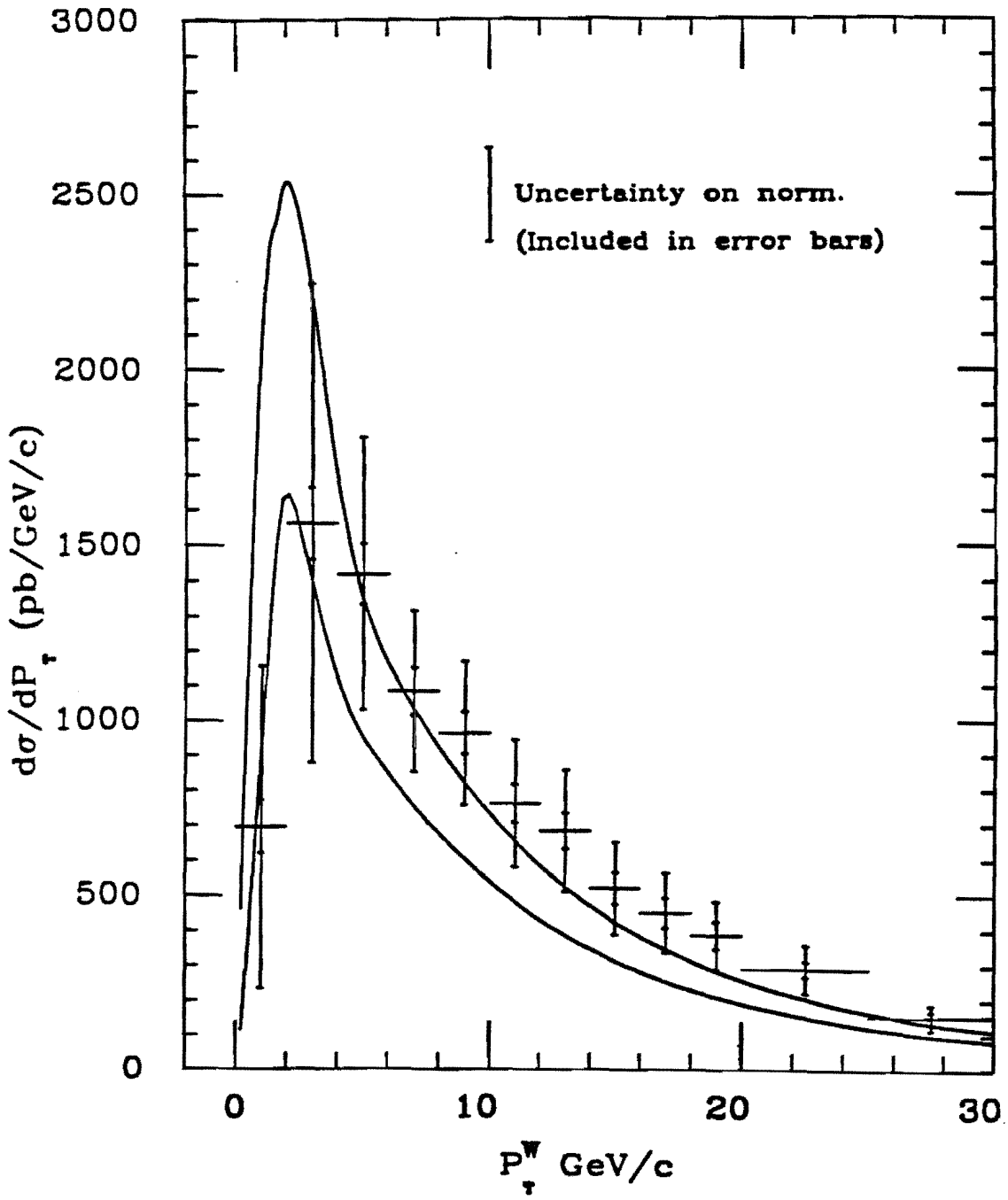

Figure 6.2: Same as Figure 6.1 except for the low P_T range. The low P_T bins are highly correlated and therefore should fluctuate as a unit (see text for more).

is slightly larger than the systematic uncertainty from the total cross section measurement. Part of the difference is caused by not renormalizing the spectrum after the smearing and $\not\!\!E_T$ systematic variations (see Chapter 5). Ideally, the systematic uncertainty of the $\not\!\!E_T$ and smearing corrections should not affect the systematic uncertainty of the integrated spectrum; but it is impossible to determine systematic variations which perfectly maintain the number of events. However, the process for determining the covariance matrix was repeated *without* allowing the smearing and $\not\!\!E_T$ corrections to vary; this eliminates their contribution. The systematic uncertainty on the integrated cross section ($\sigma \cdot B$) becomes ± 0.26 nb.

It also possible to examine the cross section above a minimum P_T^W. The spectrum was integrated above P_T^{Min} and the covariance matrix was used to propagate the uncertainty. Figure 6.3 shows the integrated spectrum above P_T^{Min} as a function of P_T^{Min}. The cross section for W boson production with $P_T > 50$ GeV/c is $423 \pm 58 \pm 108$ pb. This is in excellent agreement with the theoretical prediction of 428 ± 64 pb.

6.3 Heavy Particles Decaying into W's

A heavy particle which decays into a W boson could give an enhancement to the P_T^W spectrum at large P_T^W. However, the sensitivity of the inclusive spectrum to the effect of a heavy particle is not large. Figure 6.3 shows the expected signal from the decay of a heavy top quark ($m_{top} = 90$ GeV/c^2). The signal is approximately a factor of three lower than the standard W production based on QCD processes. The same curve is shown for a top quark with a mass of 150 GeV/c^2. To improve the signal to background ratio, further requirements, such as demand two or more high P_T jets, would have to be made on the event topology. Therefore, any significant deviation in the large P_T^W region of the inclusive distribution would indicate either the production of a heavy particle with a very large cross section or the failure of QCD to properly predict the production cross section. Figure 6.1 and 6.3 show that QCD gives an excellent prediction of the production of W bosons with large transverse momentum.

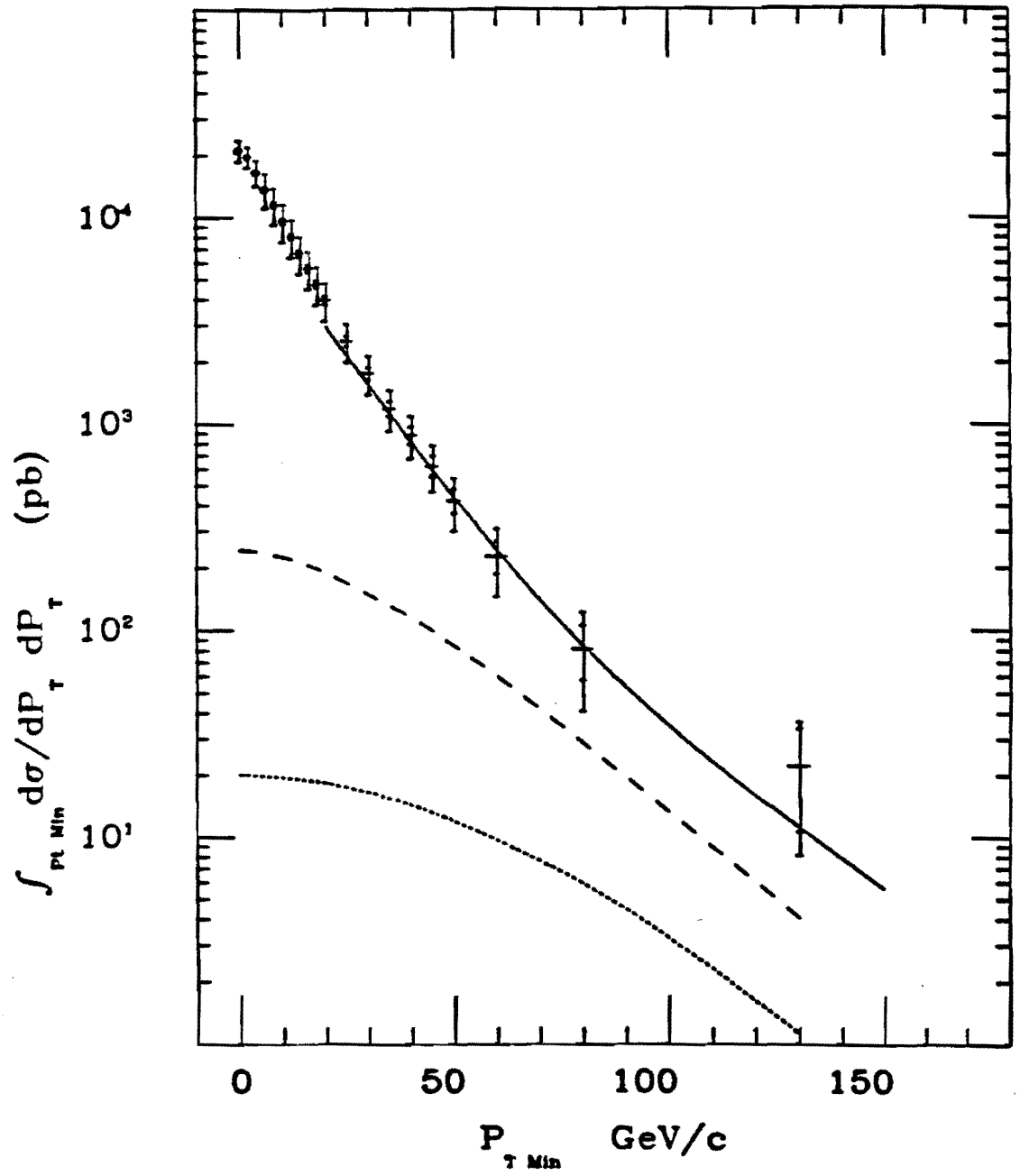

Figure 6.3: The integrated cross section above a P_T^{Min} as a function of P_T^{Min}. The value at $P_T^{Min} = 0.0$ GeV/c represent the total cross section for W boson production. The dashed (dotted) line represent the prediction from the decay of a top quark with $m_{top} = 90$ (150) GeV/c^2. The solid line is the theoretical prediction with HMRS(B) structure functions and $\Lambda_{QCD} = 190$ MeV.

Chapter 7

Conclusions

The differential cross section for W boson production provides several important tests of our understanding of the *Standard Model.* First, the agreement between the measured total cross section and the theoretical prediction provides evidence that the couplings of the W boson to quarks is properly predicted by the *Standard Model.* Second, the differential cross section, $d\sigma/dP_T$, depends both on the coupling of the W to quarks and the coupling of quarks to gluons (see Figure 1.3). The excellent agreement between experiment and theory in the region with $P_T^W > 50$ GeV/c indicates our theoretical models of the production of intermediate vector bosons with large transverse momentum are remarkable good.

Understanding W production also has several important contributions to other analyses. First, understanding W production will assist searches for the top quark. Since the top quark is heavier than the W boson, the top quark decays into a real W boson. Attempting to separate the signal of a top quark from standard W production requires knowledge of the production mechanisms. Second, the large P_T region of the W distribution can be scaled to the Z boson cross section to predict how the number of large P_T $Z \rightarrow \nu\nu$ events. This is important for monojet and supersymmetry studies.

In the future, larger data samples will allow two improvements to the measurement of the inclusive transverse momentum spectrum. First, larger P_T's can be reached with more integrated luminosity. Second, the energy corrections can be determined more precisely

with a larger sample of Z bosons. With a very large sample of Z bosons, the Z's alone will allow a precise measurement of intermediate vector boson production at low P_T. However, because of the larger cross section, the W boson will always have the advantage of reaching to larger P_T's.

In conclusion, the differential cross section for W boson production was measured in proton-antiproton collisions at a center of mass energy of 1.8 TeV. The spectrum was measured in the range $0 < P_T^W < 180$ GeV/c and fully corrected for all know experimental effects. A next-to-leading order QCD calculation agrees with the corrected distribution especially in the large P_T^W region where both the experimental and theoretical systematic uncertainties are smallest. The total cross section is $21.0 \pm 0.5\ (stat) \pm 2.6\ (sys)$ nb compared with a theoretical prediction of 18.6 ± 2.8 nb. The cross section for W production with $P_T > 50$ GeV/c is $423 \pm 58 \pm 108$ pb in excellent agreement with the theoretical prediction of 428 ± 64 pb.

Appendix A

Electron Identification Efficiency versus W Transverse Momentum

The electron identification efficiency was taken as a constant for all P_T^W. The validity of this assumption was investigated for several electron cuts. First, the requirement

$$\text{Had/EM} < 0.055 + 0.045 * \frac{E}{100.} \tag{A.1}$$

was derived with electrons from a test beam. This form attempts to maintain a constant efficiency over a large energy range. However, the sliding cut hits a hard cutoff at 0.125 due to a trigger cut and an offline electron cut. The hard cutoff occurs for electrons with E > 145 GeV. An analysis [58] of test beam electrons parameterized the efficiency of the Had/EM cut as a function of the cut value (X) and the electron energy (E). The form of the parameterization is,

$$\epsilon(X, E) = 1 - b\exp(-aX/E) \tag{A.2}$$

with $a = 5556$ and $b = 1.22$. This parameterization would predict an efficiency of 98.6% for a cut of 0.125 and an electron energy of 150 GeV. Increasing the electron energy to 200 GeV decreases the efficiency to 96%. The highest bin for the P_T^W spectrum ranges from 130 GeV/c to 180 GeV/c (see Chapter 6). For this range of P_T^W, a Monte Carlo program

predicted the average electron energy is approximately 100 GeV. Although the tail of the electron energy spectrum does extend to near 200 GeV, convoluting the spectrum with the efficiency parameterization (Eq. A.2) gave an efficiency of 98.6 %, not significantly below the 99% used.

It is also possible that a bias was caused by the trigger. If the EM energy measured by the trigger saturates, the Had/EM measured at the trigger level would be artificially high. This possibility was examined by selecting events which passed all the offline cuts but failed the online electron trigger requirement [1]. Only one event with a P_T^W above 80 GeV/c was found. This is consistent with the number expected from the measured 97% trigger efficiency.

Because of the jet activity, the isolation cut ($I < 0.1$) also could have an efficiency which changes as a function of P_T^W. A Monte Carlo program was used to study the electron isolation for different ranges of P_T^W. Table A.1 shows the results of the Monte Carlo study. The simple study shows no apparent degradation of the efficiency for P_T^W's to 200 GeV/c. For large P_T^W the electron is boosted in the W direction. Considering the naive case with a single jet recoiling against a W, the electron will tend be thrown away from the jet. Obviously, the situation is more complicated when more than one jet exists in the event.

W P_T Range (GeV/c)	1 Jet MC	2 Jet MC
$0-50$	96%	95%
$50-100$	95.5%	95%
$100-200$	96.5%	97%

Table A.1: The isolation cut efficiency for different ranges of P_T^W and different jet multiplicities. The efficiency is not a strong function of P_T^W or multiplicity.

The efficiency of the strip χ_s^2 and LSHR cuts were examined using the data. These cuts are most likely to be a function of the E_T and therefore indirectly a function of P_T^W. A sample was selected by requiring all the electron identification cuts except the LSHR and strip χ_s^2 requirements. The electron E_T was required to be greater than 25 GeV. The

[1] These events will satisfy the $\not\!\!E_T$ trigger

efficiency for the LSHR and χ^2_s cuts were examined for different ranges of electron E_T. The results are summarized in Table A.2. The uncertainties in Table A.2 are statistical. These efficiencies are not the independent efficiency for these cuts since correlations exist with other electron identification cuts. However, it is important that the values are approximately the same for the two ranges of electron E_T. These efficiencies also may be affected by jet activity. However, given the weak dependence of the electron isolation, the efficiencies for the χ^2_s and LSHR are probably not strong functions of P_T^W (total E_T).

Electron E_T Range (GeV)	LSHR ϵ	χ^2_s ϵ
$25-45$	$97\pm0.3\%$	$97\pm0.3\%$
$55-150$	$96\pm2.0\%$	$96\pm2.0\%$

Table A.2: The strip χ^2_s and LSHR efficiency for two ranges of electron E_T.

The electron identification cuts involving the CTC track are probably not sensitive to the P_T^W or at least less sensitive than the cuts examined above. Therefore, taking the electron identification cut efficiency as a constant, for the range of P_T^W's considered, was a reasonable approximation. However, for P_T^W's much larger than 200 GeV/c the efficiency for some cuts may be expected to fall.

Appendix B

Fragmentation Tuning

Simulating the observed cluster (jet) energy required convoluting the particles in the jet with the low energy response of the calorimeter. In order to properly simulate the data, the fragmentation properties of the Monte Carlo must correctly reproduce the fragmentation properties observed in the data. The fragmentation model is based on the ISAJET Monte Carlo fragmentation (Feynman-Field) [38]. The parameters of the model were adjusted to a data sample of two jet events which was not limited by statistics [54]. The jets used to tune the fragmentation are restricted to the central calorimeter where tuning quantities were defined with tracking information (see Section B.3). Since the tracking information was used, the tracking finding efficiency for the particles in jets must be understood and incorporated into the Monte Carlo simulation. After the Monte Carlo program was tuned to the two jet events, the simulated fragmentation was compared with the fragmentation observed in W events. This appendix discusses the measurement of the tracking efficiency in jets and the comparison of the tuned fragmentation with W events from data.

B.1 Tracking Efficiency

The observed fragmentation in the data not only depends on the physical fragmentation, it also depends on the efficiency for finding tracks in jets. Therefore, the track finding efficiency must be included in any fragmentation simulation tuned to the data. To measure

the track finding efficiency, first a data sample was selected. The events were chosen using the following criteria:

1. At least one jet in the central detector ($|\eta| < 0.7$).
2. A second jet back to back in ϕ, within 30°.
3. The average jet energy, $(E_T^1 + E_T^2)/2$, greater than 15 GeV.
4. No third jet with $E_T > 15$ or $E_T > 0.25 * (E_T^1 + E_T^2)$ GeV.
5. $\eta_{boost} = (\eta_1 + \eta_2)/2 < 1.0$ and $\eta^* = (\eta_1 - \eta_2)/2 < 1.0$.
6. A Z-vertex within 50.0 *cm* of the nominal interaction point.

Next, a Monte Carlo track was embedded into the central jet in these events. The raw hits of the Monte Carlo track were merged with the raw hits from the data. A different Monte Carlo track was embedded into the same real jet 30 different times[1]. The Monte Carlo tracks had the following characteristics:

1. The longitudinal momentum (relative to the jet axis) divided by the E_T of the cluster was generated flat between 0.0 and 0.4.
2. The transverse momentum (relative to the jet axis) spectrum was an exponential with an average P_T of 0.7 GeV/c.
3. The track was within a cone with $R = 0.8$ centered on the jet axis.
4. The azimuthal angle in the jet was randomized between 0 and 360 degrees.
5. The Monte Carlo track exited the CTC at the full radius.
6. The charge of the track was randomized with equal contributions of $\pm$ charges.

The efficiency was studied by retracking the events and determining how often the embedded track was found. Only tracks with full 3-dimensional reconstruction and with $P_T > 500$ MeV/c were considered. The Monte Carlo track was considered found if more than 25% of the hits from a good track matched the hits of the Monte Carlo track (generator

[1]This saves some CPU time and keeps the data set to a manageable size.

Track Efficiency in jets with $< E_T >= 80$ GeV ΔXY (3 cm steps) vs ΔZ (5 cm steps)											
	0-3	3-6	6-9	9-12	12-15	15-18	18-21	21-24	24-27	27-30	>30
0-5	0.62	0.75	0.78	0.80	0.84	0.85	0.88	0.90	0.91	0.91	0.91
5-10	0.65	0.77	0.79	0.82	0.85	0.87	0.89	0.90	0.91	0.91	0.92
10-15	0.67	0.78	0.81	0.84	0.87	0.90	0.90	0.91	0.91	0.92	0.92
15-20	0.69	0.79	0.83	0.85	0.88	0.90	0.90	0.91	0.91	0.92	0.92
20-25	0.71	0.80	0.84	0.86	0.89	0.89	0.91	0.91	0.91	0.92	0.93
25-30	0.73	0.82	0.85	0.89	0.90	0.91	0.91	0.92	0.92	0.93	0.93
>30	0.76	0.85	0.87	0.90	0.91	0.91	0.92	0.92	0.93	0.93	0.93

Table B.1:

level). If more than one track in the event satisfied this requirement, the track with the largest fraction of hits matching the Monte Carlo track was taken as the embedded Monte Carlo track.

The tracking efficiency is parameterized as a function of inter-track distance and jet E_T. The inter-track distance was broken down into XY ($R * \phi$) and Z components. Table B.1 shows the efficiency as a function of inter-track distance for jets with an average E_T of 80 GeV. The table is broken into 11 bins in the XY direction ($0-3$ cm, $3-6$ cm, $6-9$ cm, ..., $27-30$ cm, > 30 cm) and 7 bins in the Z direction ($0-5$ cm, $5-10$ cm, ..., $25-30$ cm, > 30 cm). These distances are the *sum* of the inter-track distances at three different wire radii (wires 0, 36, 83). The values in the table were smoothed to give a monotonically increasing efficiency with XY and Z distances. The uncertainty on each component is on the order of $5-10\%$.

To determine the dependence on jet E_T, the measurement was repeated using a sample of jets with $E_T > 150$ GeV. The results are shown in Table B.2. Finally, the E_T dependent tracking efficiency in jets is parameterized as follows:

For $E_T^{jet} < 80$ GeV:

$$1 - \mathrm{Eff(I,J)} = 1 - \mathrm{Eff(I,J)[80]} - 0.001 \times (80 - E_T^{jet}) \qquad \text{(B.1)}$$

For $E_T^{jet} > 80$ GeV:

$$1 - \mathrm{Eff(I,J)} = 1 - \mathrm{Eff(I,J)[80]} - \mathrm{S(I,J)} \times (80 - E_T^{jet}) \qquad \text{(B.2)}$$

Track Efficiency in jets with E_T > 150 GeV (< E_T >= 170 GeV) ΔXY (3 *cm* steps) vs ΔZ (5 *cm* steps)											
	0-3	3-6	6-9	9-12	12-15	15-18	18-21	21-24	24-27	27-30	>30
0-5	0.50	0.62	0.68	0.70	0.72	0.75	0.78	0.79	0.81	0.82	0.84
5-10	0.58	0.64	0.68	0.71	0.74	0.76	0.79	0.81	0.83	0.84	0.86
10-15	0.62	0.66	0.69	0.73	0.76	0.79	0.82	0.84	0.86	0.87	0.89
15-20	0.64	0.68	0.71	0.74	0.78	0.81	0.84	0.87	0.89	0.90	0.90
20-25	0.68	0.72	0.76	0.80	0.82	0.84	0.87	0.88	0.90	0.91	0.91
25-30	0.74	0.78	0.80	0.82	0.84	0.86	0.88	0.89	0.90	0.91	0.92
>30	0.78	0.80	0.81	0.82	0.85	0.87	0.88	0.90	0.91	0.92	0.93

Table B.2:

$S(I,J) = \Delta Eff(I,J)/\Delta E_T$ Values Multiplied by 100 ΔXY (3 *cm* steps) vs ΔZ (5 *cm* steps)											
	0-3	3-6	6-9	9-12	12-15	15-18	18-21	21-24	24-27	27-30	>30
0-5	0.14	0.14	0.11	0.11	0.12	0.11	0.11	0.11	0.11	0.10	0.08
5-10	0.10	0.13	0.12	0.12	0.12	0.12	0.11	0.10	0.09	0.08	0.07
10-15	0.06	0.13	0.13	0.12	0.12	0.12	0.09	0.08	0.06	0.06	0.03
15-20	0.06	0.12	0.13	0.12	0.11	0.10	0.07	0.04	0.02	0.02	0.02
20-25	0.03	0.09	0.09	0.07	0.08	0.06	0.04	0.03	0.02	0.02	0.02
25-30	0.02	0.04	0.07	0.07	0.07	0.06	0.03	0.03	0.02	0.02	0.01
>30	0.02	0.06	0.07	0.07	0.07	0.04	0.04	0.02	0.02	0.01	0.00

Table B.3: Slope values for the E_T dependence of the tracking efficiency

Where Eff(I, J)[80] is an element in Table B.1. The slopes, S(I, J), are linear extrapolations between the values in Table B.1 and the values in Table B.2,

$$S(I,J) = (Eff(I,J)[80] - Eff(I,J)[170])/90. \quad \text{(B.3)}$$

The S(I, J) * 100 are given in Table B.3.

Tables B.1 and B.2 roughly agree at the lower right (large inter-track distance) and disagree at small inter-track distances. The upper left element (smallest inter-track distance) is changing the fastest (see Table B.3). At a jet E_T of roughly 525 GeV, the parameterization predicts 0 efficiency. The efficiency should flatten out at some lower E_T. A jet E_T of 400 GeV was arbitrarily taken as the energy above which the efficiency does not change. This limit is well above any jet observed in the current sample of W events and has

no effect on this analysis. The measured tracking efficiency was incorporated in the Monte Carlo simulation of tracks.

B.2 Data and Simulation Samples

To test the fragmentation tuning for jets in W events, events from the data and Monte Carlo simulation were selected for comparison. The data sample was chosen from the standard W sample with the additional requirement of jet activity. The following two requirements were made:

1. One and only one jet with $E_T > 10.0$ GeV (Obs.).
2. $0.1 < |\eta_{jet}| < 0.7$

This leaves a sample with 138 events.

For the Monte Carlo sample, the PAPAGENO Monte Carlo was used as the event generator. At the generator level the following requirements are made:

1. P_T of the jet parton > 4.0 GeV/c.
2. $|\eta_{jet}| < 3.5$

The Monte Carlo events were put through a detector simulation which incorporated the tracking efficiency in jets. All the standard selection requirements were made on the electron and the $\not\!\!E_T$. Finally, the same jet requirements were made on the Monte Carlo events as were made on the data.

B.3 Fragmentation Quantities

In order to compare the fragmentation of the Monte Carlo to the data, a set of track quantities was selected for comparison. The following quantities were examined:

1. Track P_T (relative tc the beam).
2. Track Multiplicity inside the clustering cone.

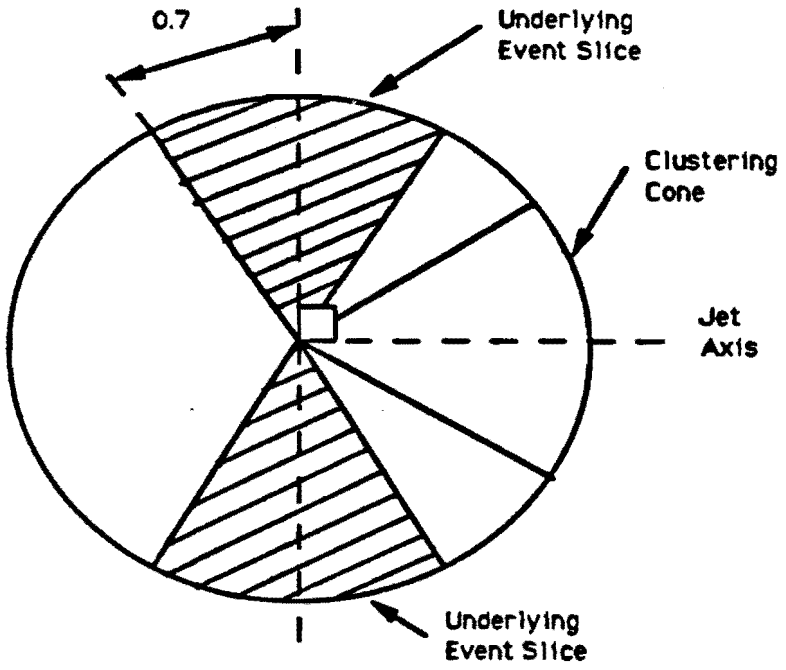

Figure B.1: The definition of the underlying event slice. The slices are located 90° away from the jet axis direction and have a half width of 0.7 radians.

3. Track $\Delta\phi$. This is the difference between the jet axis ϕ (detector coordinates) and the track ϕ (detector coordinates).
4. Track $Z_T = P_{||}^{Trk}/E_T^{Clus}$.
5. Track $Z'_T = P_{||}^{Trk}/\sum P_T^{Trks}$.

The tracks used for the comparison were required to be good 3-dimensional tracks with $P_T > 500$ MeV and the track must fall inside the clustering cone ($R = \sqrt{\Delta\eta^2 + \Delta\phi^2} = 0.7$).

Besides jet fragmentation, the energy flow of the underlying event from the spectator partons must also be tuned. The underlying event distributes energy everywhere in the detector including in the clusters. The underlying event was studied by examining tracks in slices ($\Delta\phi = 2 * 0.7$) 90 degrees away from the jet ϕ direction (see Figure B.1). If the electron was located inside an underlying event slice, that slice was ignored. The underlying event was examined using the following quantities:

1. Track P_T Spectrum.

2. Track Multiplicity.

3. Sum of the Track P_T.

B.4 Comparisons

The fragmentation tune determined with the two jet sample was used as a starting point. Figures B.2 to B.4 show a comparison of the jet fragmentation quantities in data and Monte Carlo for W events. The data is shown as points with statistical error bars and the Monte Carlo prediction is the histogram. For each quantity the ratio of the data value divided by the Monte Carlo value was examined to expose any systematic effects. The agreement between the data and Monte Carlo is reasonably good but not perfect. However, additional adjustment of the available parameters is unlikely to provide better agreement. Deviations in the fragmentation tend to be second order effects for the clustered energy correction since the low energy response does not change rapidly with particle momentum [49, 50]. The fragmentation tuned to the two jet sample adequately predicts the fragmentation observed in the W events from the data.

The energy flow from the underlying event was also examined. In this case, the Monte Carlo program tuned to the two jet events does not agree with the observed data. This was expected since it is known that two jet events have a more active underlying event than W events. The underlying event was tuned by a single parameter, X_{ue}, which loosely represents a scale factor for the mean P_T of the underlying event tracks. This parameter was tuned using the sum P_T for all the tracks in the underlying event slice. In the data sample, the average track P_T sum was found to be 1.94 GeV/c. With the two jet tune value ($X_{ue} = 0.370$), the Monte Carlo value of the average track P_T sum is 2.4 GeV/c. Adjusting X_{ue} to 0.248, the Monte Carlo value becomes 1.92 GeV/c. This value of X_{ue} was used for the simulation of the underlying event. Figure B.4 and B.5 show the underlying event quantities for the data and Monte Carlo with $X_{ue} = 0.248$. Like the jet fragmentation quantities, the agreement is not perfect but adequate.

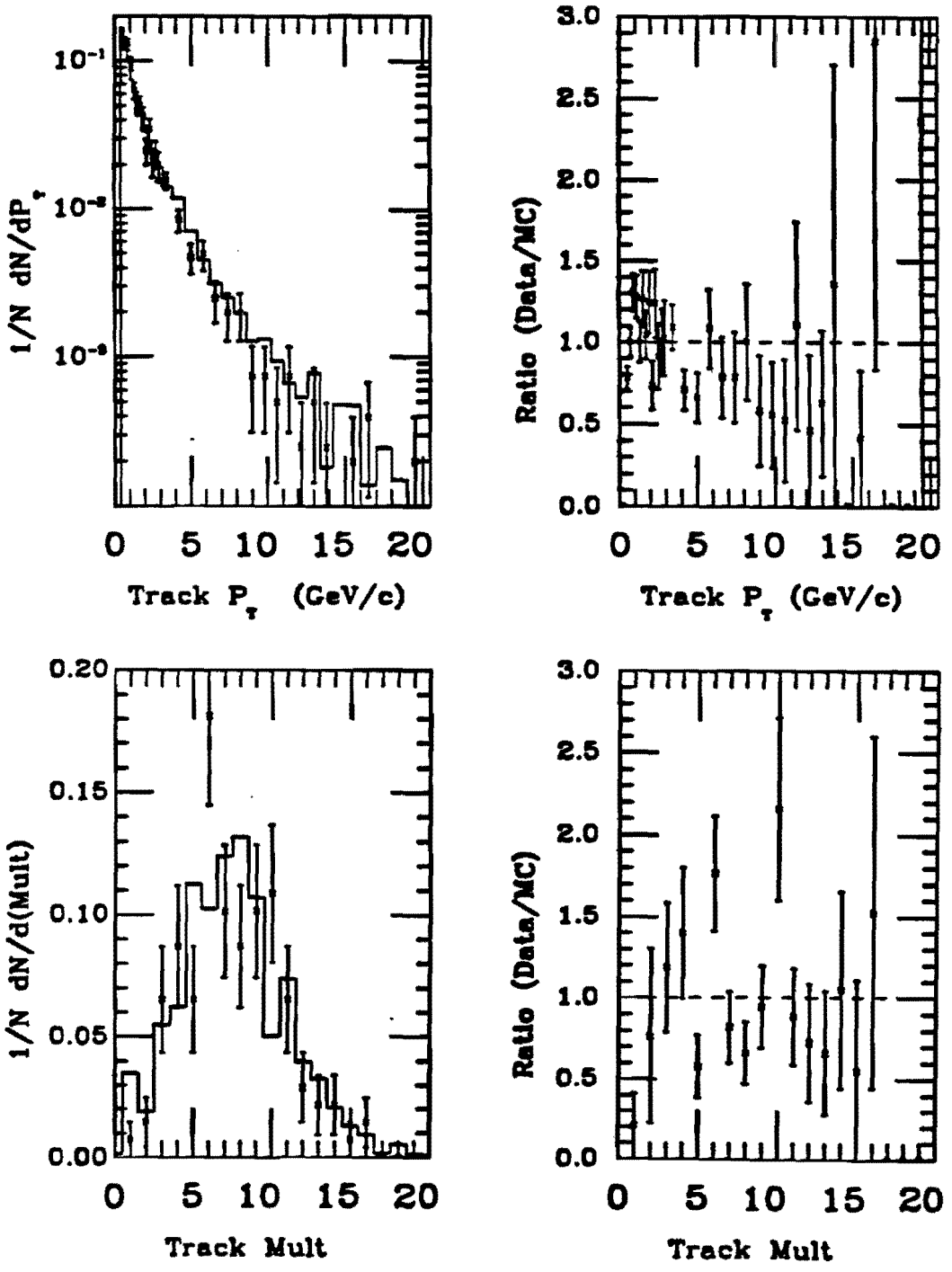

Figure B.2: A comparison between the data and the Monte Carlo fragmentation quantities for Track P_T and Track Multiplicity. The points are the data and the histogram is the prediction from the Monte Carlo program.

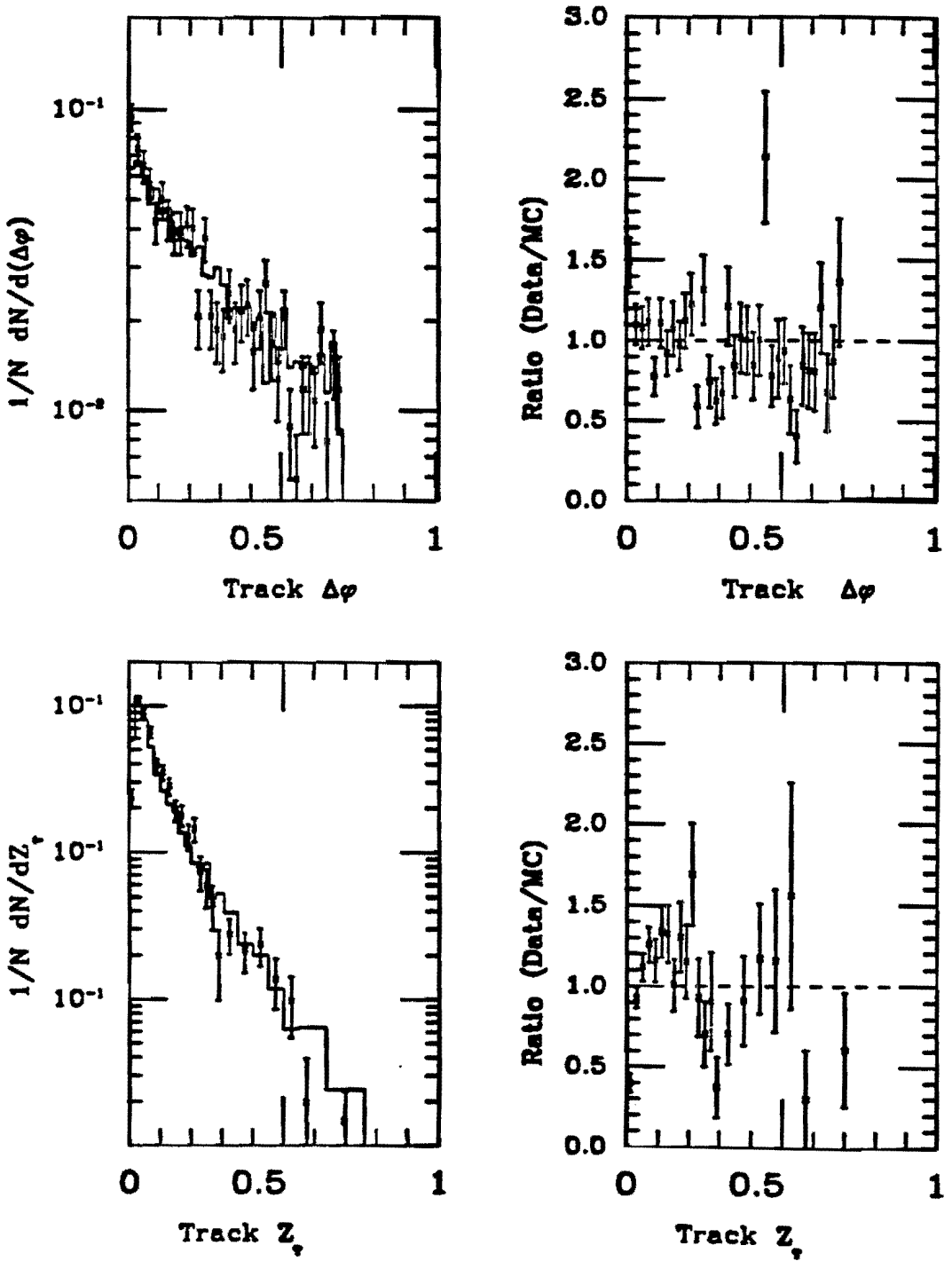

Figure B.3: A comparison between the data and the Monte Carlo fragmentation quantities for the Track $\Delta\phi$ and the Z_T. The points are the data and the histogram is the prediction from the Monte Carlo program.

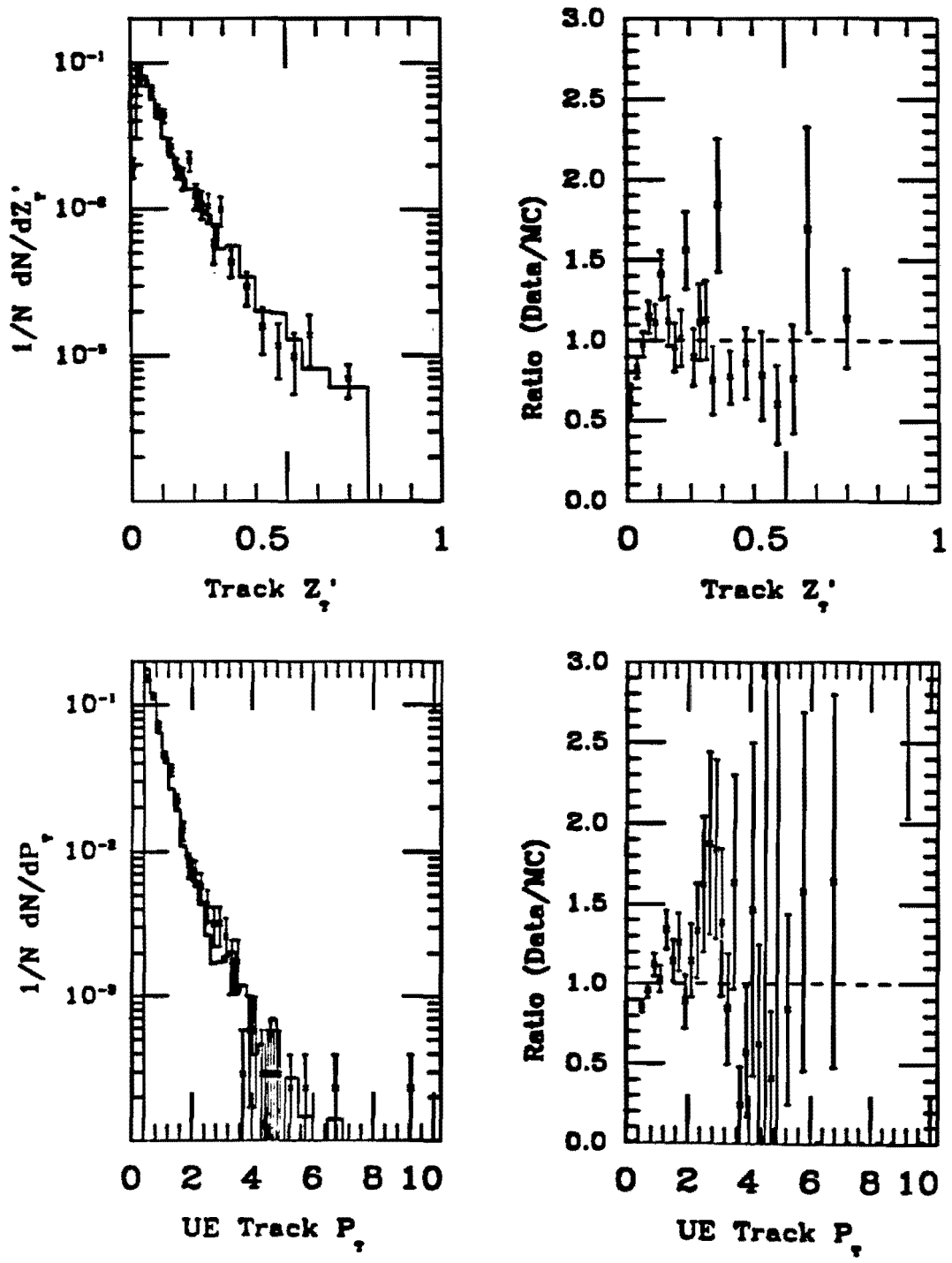

Figure B.4: A comparison between the data and the Monte Carlo fragmentation quantities for the Z_T' and the underlying event Track P_T. The points are the data and the histogram is the prediction from the Monte Carlo program.

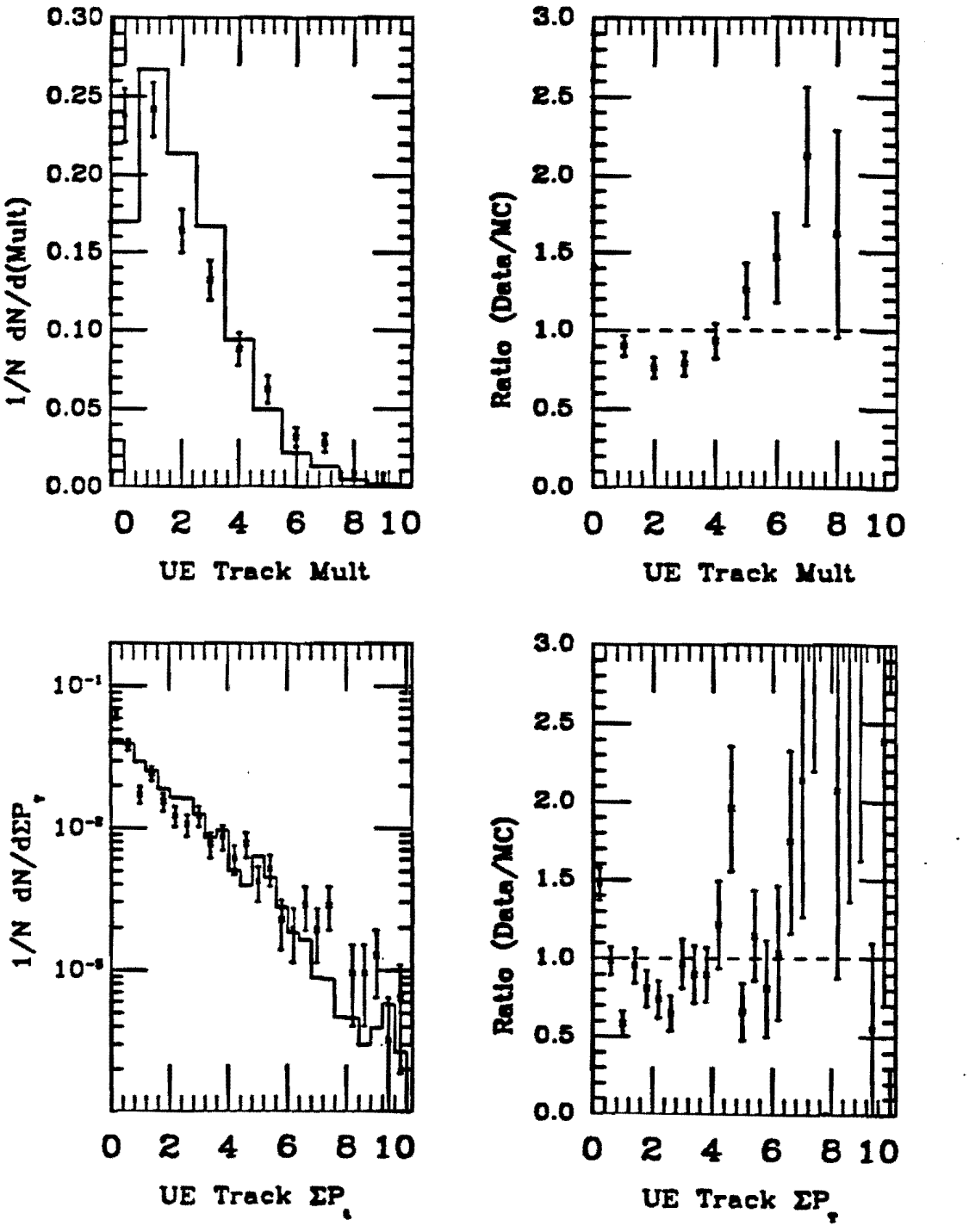

Figure B.5: A comparison between the data and the Monte Carlo fragmentation quantities for the underlying event Multiplicity and the sum of the track P_T's. The points are the data and the histogram is the prediction from the Monte Carlo program.

Appendix C

Bin Position for High P_T^W Bins

For the high P_T^W bins (P_T^W > 50 GeV/c), the P_T^W spectrum falls substantially from the lower edge of the bin to the higher edge of the bin. Given the spectrum shape, plotting the result at the bin center is not appropriate. The measured value for each bin represents the integrated cross section in the bin divided by the bin width. The proper position, P_T^{Plot}, to display the measured value is given by,

$$\frac{d\sigma}{dP_T}(P_T^{Plot}) = \frac{\int_{\Delta X} d\sigma/dP_T \; dP_T}{\Delta X} \tag{C.1}$$

(see Figure C.1). Since $d\sigma/dP_T$ is the quantity being measured, this expression can not be used as it stands. However, by fitting the results to a function, the function can be used to approximate how the spectrum falls from one side of the bin to the other. Given a function for $d\sigma/dP_T$, the expression above can be solved numerically to determine P_T^{Plot} for each bin. Using the function given in Section 6.2.2, the procedure predicts the P_T^{Plot} position for the highest four bins. The P_T^{Plot}'s (bin center) are 54.7 (55), 68.9 (70), 99.6 (105), and 151.2 (155). The variation from the bin center for the lower P_T bins is small and no changed was made. If instead of using a fit to the results, a fit to the theory is used, the P_T^{Plot}'s found are very similar to those given above.

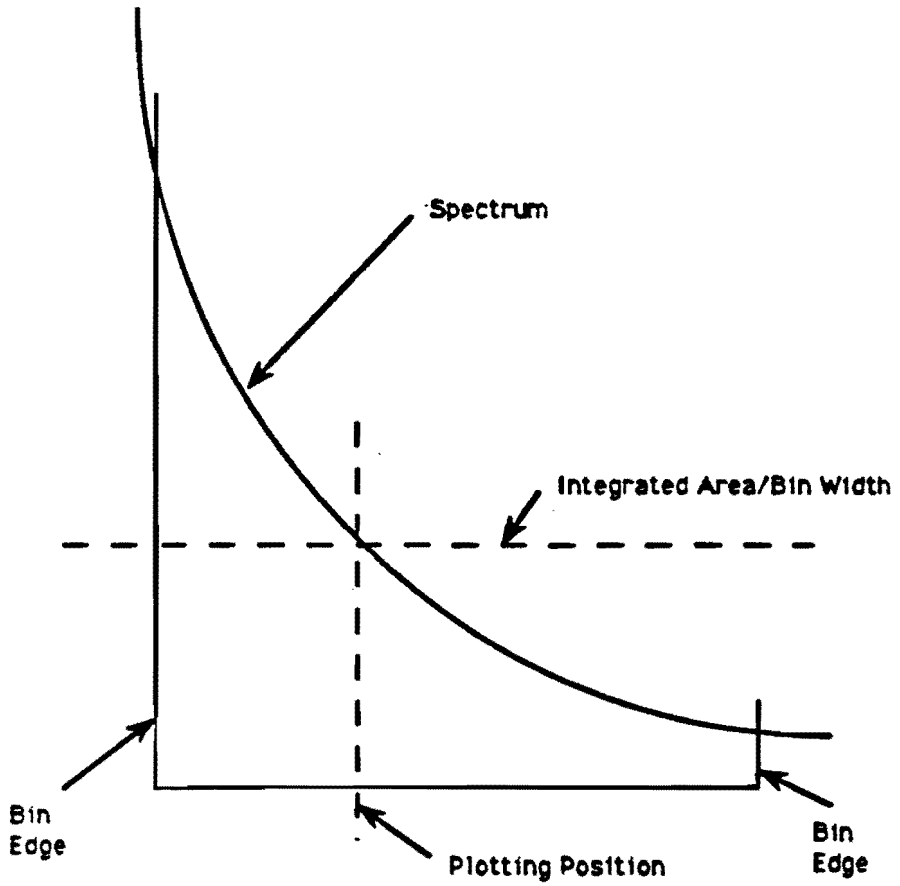

Figure C.1: The determination of the plotting position for the high P_T spectrum bins. The bin center is not the proper position to plot the measured value for the high P_T bins. Instead, the position, P_T^{Plot} is the correct position.

Appendix D

Covariance Matrix

In Chapter 5, a covariance matrix was derived to describe the correlations between bins of the transverse momentum spectrum. The covariance matrix is define by the relation,

$$C_{ij} = \frac{1}{M}\sum_{n=1}^{M}(Y_i^n - \bar{Y}_i) * (Y_j^n - \bar{Y}_j) \tag{D.1}$$

where,

- M, the total number of simulated samples generated. (M = 10^6)
- $\bar{Y}_i$, the average value for the i^{th} bin. Taken as the fully corrected cross section for the i^{th} bin.
- Y_i^n is the value for the i^{th} bin for the n^{th} sample.

The covariance matrix given in Table D.1 contains both the systematic and statistical uncertainty. The matrix is symmetric and only the upper half of the matrix is shown.

The covariance matrix can be used to determine the correlation coefficients. The coefficients described the magnitude of the correlation between different bins and are defined as,

$$\rho_{ij} = \frac{C_{ij}}{\sqrt{C_{ii} * C_{jj}}} \tag{D.2}$$

The correlation coefficients are given in Table D.2.

Table D.1: The covariance matrix for the combine systematic and statistical uncertainty for the $d\sigma/dP_T$ measurement is shown. The matrix is symmetric and only half of the elements are shown. The row and column numbers are given along the borders of the matrix. The matrix is shown in two pieces to conserve space.

	1	2	3	4	5	6	7	8	9	10
1	0.212E6	0.300E6	0.159E6	-0.423E5	-0.600E5	-0.564E5	-0.546E5	-0.390E5	-0.319E5	-0.236E5
2		0.468E6	0.247E6	-0.481E5	-0.809E5	-0.794E5	-0.775E5	-0.557E5	-0.460E5	-0.343E5
3			0.150E6	-0.884E4	-0.330E5	-0.366E5	-0.364E5	-0.265E5	-0.225E5	-0.170E5
4				0.531E5	0.348E5	0.250E5	0.224E5	0.149E5	0.107E5	0.740E4
5					0.424E5	0.315E5	0.293E5	0.210E5	0.167E5	0.126E5
6						0.334E5	0.288E5	0.212E5	0.173E5	0.138E5
7							0.302E5	0.204E5	0.163E5	0.130E5
8								0.174E5	0.123E5	0.991E4
9									0.131E5	0.916E4
10										0.935E4

	11	12	13	14	15	16	17	18	19	20
1	-0.144E5	-0.546E4	-0.322E4	-0.159E4	-0.128E4	-0.101E4	-0.583E3	-0.265E3	-0.651E2	-0.108E2
2	-0.211E5	-0.779E4	-0.440E4	-0.211E4	-0.163E4	-0.129E4	-0.753E3	-0.350E3	-0.880E2	-0.129E2
3	-0.107E5	-0.369E4	-0.187E4	-0.802E3	-0.556E3	-0.429E3	-0.259E3	-0.130E3	-0.348E2	-0.305E1
4	0.394E4	0.203E4	0.162E4	0.963E3	0.885E3	0.711E3	0.371E3	0.140E3	0.274E2	0.842E1
5	0.791E4	0.351E4	0.241E4	0.130E4	0.110E4	0.878E3	0.459E3	0.183E3	0.376E2	0.106E2
6	0.915E4	0.389E4	0.243E4	0.117E4	0.934E3	0.722E3	0.347E3	0.125E3	0.219E2	0.742E1
7	0.848E4	0.346E4	0.206E4	0.982E3	0.785E3	0.613E3	0.301E3	0.111E3	0.207E2	0.649E1
8	0.659E4	0.269E4	0.159E4	0.746E3	0.590E3	0.457E3	0.224E3	0.825E2	0.153E2	0.492E1
9	0.657E4	0.300E4	0.197E4	0.955E3	0.742E3	0.563E3	0.267E3	0.982E2	0.175E2	0.600E1
10	0.558E4	0.257E4	0.168E4	0.803E3	0.617E3	0.466E3	0.216E3	0.777E2	0.132E2	0.485E1
11	0.481E4	0.206E4	0.139E4	0.666E3	0.507E3	0.378E3	0.171E3	0.608E2	0.987E1	0.390E1
12		0.138E4	0.777E3	0.383E3	0.294E3	0.219E3	0.996E2	0.360E2	0.593E1	0.231E1
13			0.809E3	0.299E3	0.233E3	0.174E3	0.805E2	0.299E2	0.517E1	0.190E1
14				0.274E3	0.124E3	0.939E2	0.453E2	0.178E2	0.341E1	0.111E1
15					0.195E3	0.760E2	0.376E2	0.151E2	0.302E1	0.937E0
16						0.134E3	0.297E2	0.123E2	0.253E1	0.746E0
17							0.350E2	0.720E1	0.164E1	0.425E0
18								0.710E1	0.870E0	0.198E0
19									0.480E0	0.048E0
20										0.078E0

	1	2	3	4	5	6	7	8	9	10
1	1.000	0.952	0.889	-0.398	-0.633	-0.670	-0.682	-0.641	-0.605	-0.530
2		1.000	0.929	-0.305	-0.574	-0.635	-0.652	-0.617	-0.588	-0.518
3			1.000	-0.099	-0.413	-0.517	-0.539	-0.518	-0.507	-0.453
4				1.000	0.734	0.593	0.558	0.489	0.406	0.332
5					1.000	0.837	0.820	0.773	0.711	0.635
6						1.000	0.906	0.881	0.829	0.780
7							1.000	0.891	0.820	0.771
8								1.000	0.815	0.776
9									1.000	0.828
10										1.000

	11	12	13	14	15	16	17	18	19	20
1	-0.451	-0.319	-0.246	-0.209	-0.198	-0.190	-0.214	-0.216	-0.204	-0.084
2	-0.445	-0.306	-0.226	-0.186	-0.171	-0.163	-0.186	-0.192	-0.186	-0.067
3	-0.397	-0.256	-0.170	-0.125	-0.103	-0.096	-0.113	-0.126	-0.130	-0.028
4	0.246	0.238	0.248	0.252	0.275	0.267	0.272	0.228	0.172	0.130
5	0.554	0.459	0.411	0.380	0.383	0.369	0.377	0.333	0.264	0.183
6	0.722	0.574	0.467	0.387	0.367	0.342	0.321	0.257	0.173	0.145
7	0.703	0.535	0.418	0.341	0.324	0.305	0.293	0.240	0.172	0.133
8	0.720	0.548	0.423	0.341	0.320	0.299	0.286	0.234	0.168	0.133
9	0.828	0.707	0.607	0.504	0.465	0.425	0.394	0.322	0.221	0.187
10	0.832	0.715	0.611	0.502	0.458	0.417	0.377	0.302	0.197	0.179
11	1.000	0.799	0.705	0.579	0.524	0.471	0.418	0.329	0.205	0.201
12		1.000	0.736	0.623	0.569	0.511	0.454	0.364	0.231	0.222
13			1.000	0.635	0.586	0.529	0.479	0.395	0.263	0.239
14				1.000	0.537	0.490	0.463	0.404	0.297	0.238
15					1.000	0.471	0.456	0.408	0.312	0.240
16						1.000	0.434	0.398	0.315	0.230
17							1.000	0.457	0.401	0.257
18								1.000	0.472	0.265
19									1.000	0.246
20										1.000

Table D.2: The correlation coefficients for the combine systematic and statistical uncertainty for the $d\sigma/dP_T$ measurement are shown in matrix form. The matrix is symmetric and only half of the elements are shown. The row and column numbers are given along the borders of the matrix. The matrix is shown in two pieces to conserve space.

Bibliography

[1] E. Rutherford, Phil. Mag. **21**, 669 (1911).

[2] *Report of the General Meeting on LEP, Villars-sur-Ollon, Switzerland*, edited by M. Bourguin, (1981).

[3] *SLC Design Handbook, Stanford Linear Accelerator Center*, edited by R. Erickson, (1984).

[4] Glashow, S. L., Nucl. Phys. **22**, 579 (1961).

[5] Weinberg, S., Phys. Rev. Lett. **19**, 1264 (1967).

[6] Salam, A., Nobel Symposium # 8, edited by W. Svartholm (1968).

[7] UA1 Collaboration, Phys. Lett., **122B**, 103 (1983).

[8] UA2 Collaboration, Phys. Lett. **122B**, 476 (1983).

[9] UA1 Collaboration, Phys. Lett. **126B**, 398 (1983).

[10] UA2 Collaboration, Phys. Lett. **129B**, 130 (1983).

[11] Bardeen, W. A., Fritzsch, H., and Gell-Mann, M., in *Scale and Conformal Symmetry in Hadron Physics*, edited by R. Gatto, Wiley, New York (1973).

[12] Gros, D. J. and Wilczek F., Phys. Rev. **D8**,3633 (1973).

[13] Weinberg, S., Phys. Rev. Lett. **31**, 494 (1973).

[14] M. Aguilar-Benitez *et al.*, Phys. Lett. **239B**, 1 (1990).

[15] McAllister, R. W. and Hofstadter, R., Phys. Rev. **102**, 851 (1956).

[16] Fisk, H. E. and Sculli, F., Ann. Rev. Nucl. Part. Sci. **32**,499 (1982).

[17] G. Altarelli and G. Parisi, Nucl. Phys. **B127**, 298 (1977).

[18] J. Collins, D. Soper and G. Sterman, Nucl. Phys. **B250**, 199 (1985).

[19] P. Arnold and M. H. Reno, Nucl. Phys. **B319**, 37 (1989); erratum: Nucl. Phys. **B330**, 284 (1990).

[20] P.B. Arnold and R.P. Kauffman, ANL-HEP-PR-90-70 (to be published).

[21] P.N. Harriman, A.D. Martin, W.J. Stirling, and R.G. Roberts, Phys. Rev. **D42**, 798 (1990).

[22] UA2 Collaboration: J. Alitti *et al.*, Z. Phys. **C47**, 523 (1990).

[23] UA1 Collaboration: C. Albajar *et al.*, Z. Phys. **C44**, 15 (1989).

[24] H. Edwards, Proceedings of the XIII International Conference on High Energy Accelarators, Vol. 1 Page 20, (1990).

[25] F. Abe *et al.*, Nucl. Instr. Methods Phys. Res., **A271**, 387 (1988).

[26] G. W. Foster *et al.*, Nucl. Instr. Methods Phys. Res., **A269**, 93 (1988).

[27] D. Amidei *et al.*, Nucl. Instr. Methods Phys. Res., **A269**, 51 (1988).

[28] D. Brown and M. E. B. Franklin, CDF Note# 605 (1988).

[29] G. Redlinger and Y. D. Tsay, CDF Note# 521 (1987).

[30] F. Abe *et al.*, Phys. Rev. Lett. **62**,613 (1989).

[31] D. Brown *et al.*, CDF Note# 605 (1988).

[32] R. Harris, CDF Note# 1329 (1990).

[33] B. Adeva *et al.*, Phys. Lett. **B231**, 509 (1989).

[34] D. Decamp *et al.*, Phys. Lett. **B231**, 519 (1989).

[35] M. Akrawy *et al.*, Phys. Lett. **B231**, 530 (1989).

[36] P. Aarnio *et al.*, Phys. Lett. **B231**, 539 (1989).

[37] M. Gold, CDF Note# 912 (1989).

[38] F. Paige and S. D. Protopopescu, BNL Report No. 38034, (1986). ISAJET Version 6.25 was used.

[39] M. Shapiro, D. Brown, and Sheila Kannappan, CDF Note# 753 (1988).

[40] C. Campagnari, P. Derwent, and M. Miller, CDF Note# 1245 (1990).

[41] K. Sliwa, in *Proceedings of XXVth Rencontres de Moriond, Les Arcs, Savoie, France (1990)*, Edition Frontieres, **M65**, 456 (1990).

[42] C. Bowers, C Campagnari, P. Derwent, H. Frisch, S. Kopp, M. Miller, CDF Note# 1026 (1989).

[43] I. Hinchliffe, private communication. Version 3.12 of PAPAGENO was used.

[44] D. Brown, CDF Note# 873 (1989).

[45] B. Winer, P. Tipton, CDF Note# 920 (1990).

[46] A. D. Martin, R. G. Roberts, and W. J. Stirling, Phys. Rev. **D37**, 1161 (1988).

[47] E. Eichten, I. Hinchliffe, K. Lane, and C. Quigg, Rev. Mod. Phys. **56**, 579 (1984).

[48] G. Martinelli, Nucl. Phy. **B316**, 355 (1989).

[49] S. Behrends, S. Kuhlmann, D Amidei, and F. Rimondi, CDF Note# 583 (1987).

[50] S. Behrends, M. Shapiro, E. Pare, CDF Note# 1066 (1989).

[51] F. Abe *et al.*, FERMILAB-PUB-90/162-E (1990). (Submitted to Phys. Rev. D, Aug 1990).

[52] W. Trischuck, Ph.D. Thesis, Havard University (1990).

[53] D. Brown, CDF Note# 835 (1988). The analysis was updated for the 1988-89 run.

[54] T. Hessing, S. Behrends, P. Tipton, and B. Winer, CDF Note# 1131 (1990).

[55] B. Winer, CDF Note# 1239 (1990).

[56] M. Binkley, CDF Note# 1096 (1990).

[57] F. Abe *et al.*, FERMILAB-PUB-90/229-E (1990).

[58] M. Gold, CDF Note# 1161 (1990).